2016-04-01

Droplet Impingement on Superhydrophobic Surfaces

Cristian Esteban Clavijo Angeles
Brigham Young University

BYU ScholarsArchive Citation

Clavijo Angeles, Cristian Esteban, "Droplet Impingement on Superhydrophobic Surfaces" (2016). *All Theses and Dissertations*. 6306.
https://scholarsarchive.byu.edu/etd/6306

Droplet Impingement on Superhydrophobic Surfaces

Cristian Esteban Clavijo Angeles

A dissertation submitted to the faculty of
Brigham Young University
in partial fulfillment of the requirements for the degree of

Doctor of Philosophy

Julie Crockett, Chair
R. Daniel Maynes
Brian D. Iverson
Matthew R. Jones
S. Andrew Ning

Department of Mechanical Engineering

Brigham Young University

April 2016

ABSTRACT

Droplet Impingement on Superhydrophobic Surfaces

Cristian Esteban Clavijo Angeles
Department of Mechanical Engineering, BYU
Doctor of Philosophy

This dissertation explores the physics of droplet impingement on superhydrophobic surfaces. The research is divided in three categories. First, the effect of a slip boundary condition on droplet spreading/retracting is considered. A model is developed based on energy conservation to evaluate spreading rates on surfaces exhibiting isotropic and anisotropic slip. The results show that larger slip causes the droplet to spread out farther owing to reduced friction at the interface for both slip scenarios. Furthermore, effects of slip become magnified for large Weber numbers due to the larger solid-liquid contact area during the process. On surfaces with anisotropic slip, droplets adopt an elliptical shape following the azimuthal contour of the slip on the surface.

It is common for liquid to penetrate into the cavities at the superhydrophobic interface following droplet impact. Once penetrated, the flow is said to be in the Wenzel state and many superhydrophobic advantages, such as self-cleaning and drag-reduction, become negated. Transition from the Wenzel to the Cassie state (liquid resides above the texture) is referred to as dewetting and is the focus of the second piece of this dissertation. Micro-pillar pitch, height and temperature play a role on dewetting dynamics. The results show that dewetting rates increase with increasing pillar height and increasing surface temperature. A scaling model is constructed to obtain an explanation for the experimental observations and suggests that increasing pillar height increasing the driving dewetting force, while increasing surface temperature decreases dissipation.

The last piece of work of this dissertation entails droplet impingement on superheated surfaces (100°C - 400°C). We find that the Leidenfrost point (LFP) occurs at a lower temperature on a hydrophobic surface than a hydrophilic one, where the LFP refers to the lowest temperature at which secondary atomization ceases to occur. This behavior is attributed to the manner in which vapor bubbles grow at the solid-liquid interface. Also in this work, high-speed photographs reveal that secondary atomization can be significantly suppressed on a superhydrophobic surface owing to the micro-pillar forest which allows vapor to escape hence minimizing bubble formation within the droplet. However, a more in-depth study into different superhydrophobic texture patterns later reveals that atomization intensity can significantly increase for small pitch values given the obstruction to vapor flow presented by the increased frequency of the pillars.

Keywords: superhydrophobic, droplet impingement, boiling, slip velocity, moving triple contact line

ACKNOWLEDGMENTS

I wish to express gratitude to my sweet companion, Danielle Clavijo, who was extremely supportive during my PhD. She demonstrated patience in the long hours I spent in the lab including weekends and holiday breaks. I always found motivation to keep pushing forward at work because of her positive and uplifting personality. She became the main care-taker of our son who was born in the middle of my studies, allowing me to focus on my PhD work.

I thank my father, mother and sister. Their support began long before graduate school. They were always interested in helping me succeed. During my PhD, they have been a source of recreation and motivation by making sure family activities and reunions came to pass on a regular basis regardless of how far apart we lived.

Other students in the lab became my close friends. Though many of my contributions may not carry their name, my work was very much inspired by countless conversations with them. They taught me scientific principles I did not understand, reminded me of physical laws I had forgotten and engaged in postulating hypotheses for the phenomena observed. Julie Crockett is an unbelievable mentor who allowed me to grow as a researcher and as a person. I thank her for her patience with my stubborn personality and with the myriad of questions I asked her on a weekly basis about what is the purpose of science, academia and life in general (sometimes I would ask about research). In combination with Dan Maynes, they permitted me the freedom to suggest my own direction throughout my PhD. Their expertise in the thermal fluids arena proved invaluable.

I am grateful for The Church of Jesus Christ of Latter-day Saints, Brigham Young University and all the people behind these two magnificent institutions. The mix between scholarship and faith truly makes BYU a unique institution and one that provides an education far superior to that which would be achieved by secular means alone.

Finally, I express gratitude to the National Science Foundation (Grant No. CBET 1235881 and Grant No. 1066356) for having funded this work.

TABLE OF CONTENTS

LIST OF TABLES

LIST OF FIGURES

CHAPTER 1. INTRODUCTION

Research is driven by different purposes. One school of thought is solely based on curiosity where the researcher measures his/her success by increased understanding of the world around them. On the other hand is the driving force of innovation seeking to engineer new solutions to existing applications. While curiosity may be a part of such endeavor, emphasis is placed on how the results might benefit others. While an entire spectrum exists between the two foregoing mentalities (for instance, Technology Readiness Level), the present work lends itself towards the former. Thus, the body of this dissertation does not hint at the optimization of any existing technology or soon-to-be technology, nor does its intent intimately pursue what thermal engineers nominally seek after such as improving heat transfer rates. Rather, the author provides theoretical and experimental evidence to explain unexplored physicochemical phenomena, the corresponding projects which resulted from curiosity.

This work entails temporally and spatially transient behavior of surface tension dominated flows, extreme water-repellency effects, interactions at solid-liquid-gas boundaries and phase change, all in terms of a single millimetric droplet impinging on a solid surface. In Sec. 1.1, background information is given regarding droplet impingement, superhydrophobic surfaces and boiling. Common examples that people run into on a daily basis will be highlighted for each of these cases, as well as current and potential applications. Sec. 1.2 will discuss the current state-of-the-art research for the topics covered in each of the subsequent chapters in this dissertation (Chapters 2, 3, 4 and 5). Unexplored corners of the field that motivated our studies shall be made manifest, as well as the specific contributions of the author. Finally, the outline of the remainder of the dissertation will be provided in Sec. 1.3.

1.1 Background

1.1.1 Droplet Impingement

Droplet impingement on solid surfaces is a ubiquitous occurrence in everyday life. A few examples include rain impacting house rooftops, crime-scene blood stains by which detectives deduce how assassinations occurred, and even how some artists transfer ink onto their canvases during gestural abstraction. There are also many applications that depend on our understanding of this rather complex interaction. The resolution and accuracy of spray coatings, ink jet printers and 3D printers, to name a few, all depend on the spacing, frequency and deformation of impinging droplets, and these technologies can only improve by understanding the fundamental physicochemical behavior. While most droplet impingement scenarios in real life generally occur in a group of droplets impacting a surface rather than a single one, academia often places emphasis on the latter. This simplifies an otherwise extremely complex scenario and makes it possible to analyze fundamental dynamics while still providing useful insight into real-life scenarios. The work here is no exception and only considers single droplet impingement.

Cohesion of liquids results from intermolecular forces attracting liquid molecules to each other. These interactions allow momentum to be transferred through a liquid and the magnitude of its resistance is known as viscosity. Cohesion causes molecules at immiscible liquid-gas or liquid-liquid interfaces to experience an inward pull (normal to interfacial curvature) due to the uneven distribution of intermolecular forces. Surface tension is a result of this inward pull and is commonly expressed as σ with units of force per unit length. Surface tension is thus a force that acts tangentially to the surface of the liquid and seeks to minimize its interfacial area, thus giving droplets their spherical shape. Although effects of surface tension can be neglected in most fluid mechanic problems, flows that occur at the millimetric scale or less and contain liquid-gas interfaces are typically dominated by surface tension, as is the case with droplet impingement.

The intricate physics of droplet impingement are due to the temporal and spatial nature of the event. Furthermore, behavior varies widely depending on the wettability of the surface the droplet comes in contact with. While other parameters vary the outcome of the event, such as the composition of the liquid and the inclination of the surface relative to the impingement path, we limit our discussion to a water droplet impinging normal to a stationary horizontal solid surface.

When the surface is hydrophilic or "water-attracting" (e.g. glass), the droplet spreads out and remains in a flat position. On the other hand, a droplet impinging on a hydrophobic or "water-repelling" (e.g. Teflon coated cooking pans) surface spreads out at first but then recoils due to a surface tension pull and rebounds. Both of these events are are shown in Fig. 1.1 for two different impact speeds (0.3 m/s and 7.0 m/s). The images also show that for long times after impact, the droplet assumes its equilibrium shape with the surface, which is independent of impact speed. The difference in impingement behavior on hydrophilic and hydrophobic surfaces arise from the type of van der Waal forces formed at the solid-liquid interface; hydrogen bonds prevail in the former while dispersion forces in the latter.

Another important parameter in determining the outcome of the impingement event is the momentum with which the droplet impacts the surface (also shown in Fig. 1.1). The Weber number, $We = \rho V^2 D/\sigma$, where ρ, V and D are the density of the liquid, and velocity and diameter at impact, is the most commonly used non-dimensional number to quantify impingement. It provides direct comparison between inertial and surface tension forces at impact (consequently it is often referred to as the impact Weber number). For large Weber numbers, little droplets fly off from the periphery of the droplet and the droplet is said to *splash*. On the other hand, when inertia is small relative to surface tension, dynamics are governed by surface tension and minimal deformation takes place.

1.1.2 Superhydrophobic Surfaces

A trip to the world-renown Denver Botanic Gardens will lavish the visitor with over 9,517 species of plants [12]. Towards the back of the exhibit, a peculiar group of circular plant leaves (see Fig. 1.2), roughly a foot in diameter, sit next to a large pond. The name on the identifier tag quickly reveals this family's name: The Lotus Plant. Just a few feet away, a couple of water-striders can usually be spotted on scene walking on water. What do these two have in common? Superhydrophobic "skin", which in both cases allows these plants and insects to thrive in their environment.

Superhydrophobicity means extreme water repellency. In the case of superhydrophobic plants such as the Lotus, when rain falls, water is unable to stick to the surface. Instead, the droplets bounce or roll off the leaves, directing the water to the soil. Superhydrophobic surfaces exhibit

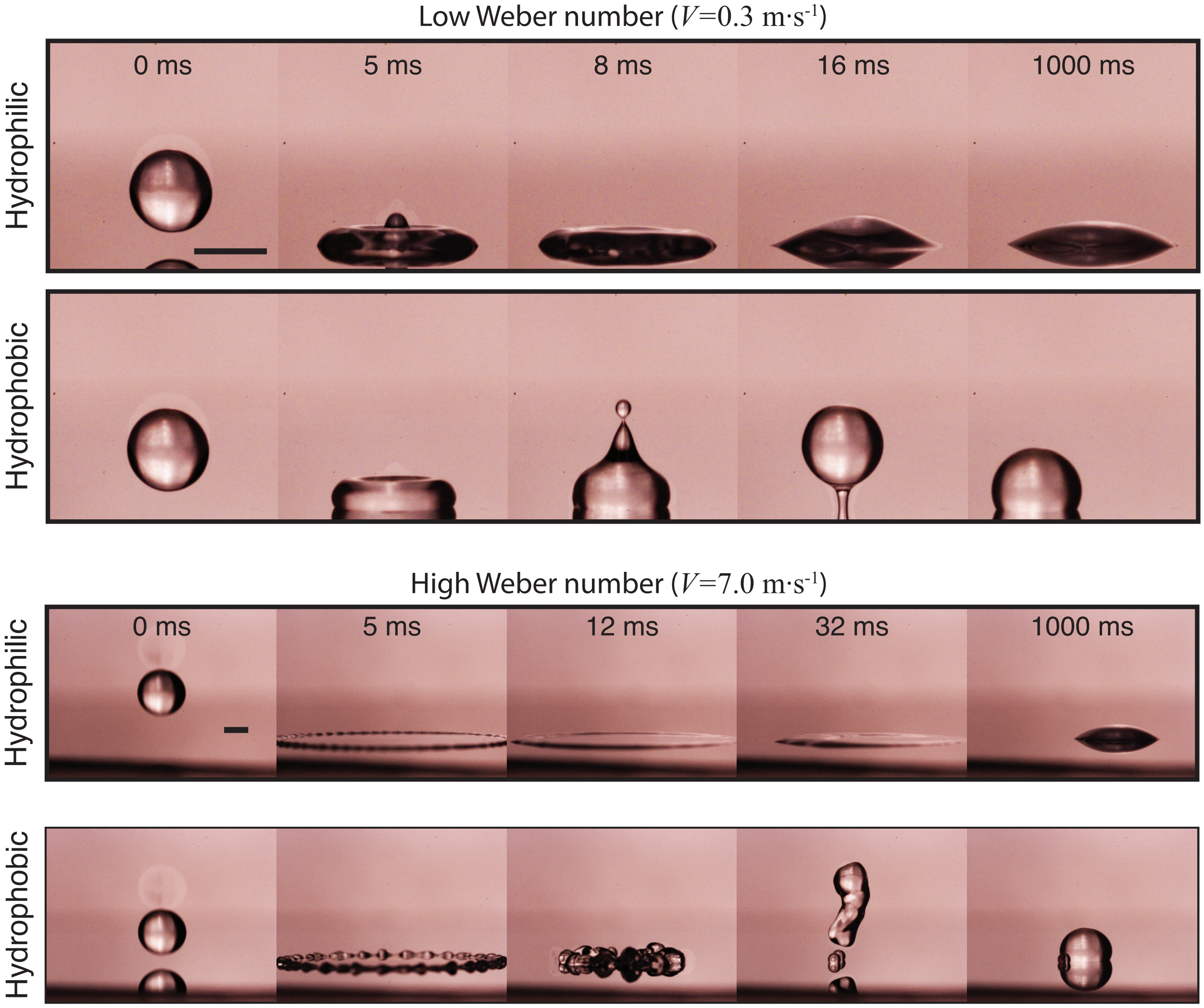

Figure 1.1: Droplet impingement on a hydrophilic and hydrophobic surface at room temperature at high Weber number, 350, (top two sequences) and low Weber number, 10, (bottom two sequence). Scale size, 2mm.

much stronger repellency than hydrophobic ones (discussed in the last section) and "the Lotus effect" has been coined to represent superhydrophobic interactions. In the case of the water-strider, their superhydrophobic legs allow them to roam freely across the pond even though their body density is larger than that of water. On the other side of the spectrum of wettability, extreme water-loving surfaces also exist and are named superhydrophilic. One example of superhydrophilicity found in nature is plant capillaries which distribute water against gravity throughout the plant [13]. While most of this dissertation is concerned with superhydrophobic interactions, experiments were also conducted on surfaces over the entire wettability spectrum.

Figure 1.2: Photograph of the Lotus leaf with a water droplet on it prior to roll off [1].

What causes a surface to be superhydrophobic or superhydrophilic? In either case, the solid surface must exhibit micro or nano texturing in addition to a hydrophobic or hydrophilic coating. When water comes in contact with the surface, the increase in solid-liquid contact area effectively increases water repellency or water attraction macroscopically. Unique to a superhydrophobic surface, two equilibrium states exist. Water can completely wet the textured interface, as is the case on a superhydrophilic surface, or it can remain suspended above the texture due to surface tension. The former state is called the Cassie state and the latter the Wenzel state; schematic drawings of both of these are shown in Fig. 1.3a. The state of residence depends on many factors such as how water nucleated at the interface (in the case of condensation) or the pressure of the water flow relative to that in the gas at the interface.

With the advent of micro-fabrication techniques, nature is no longer the sole owner to superhydrophobic technology. Figure 1.3 shows a Scanning Electron Microscope (SEM) photograph of one of the superhydrophobic surfaces fabricated by the author, made up of pillars about 10 μm in height. In fact, superhydrophobic sprays are now commonly sold in hardware stores for under $20 and claim to keep your clothes and shoes dry in case of bad weather. Remarkably, there is an increasing need for superhydrophobic surfaces at a grander commercial scale due to their many hydrodynamic advantages. For example, superhydrophobic surfaces can reduce drag for internal (piping networks which require large pumping requirements) or external (a torpedo traveling in the ocean) flow scenarios. Drop-wise condensation is another attractive application of superhy-

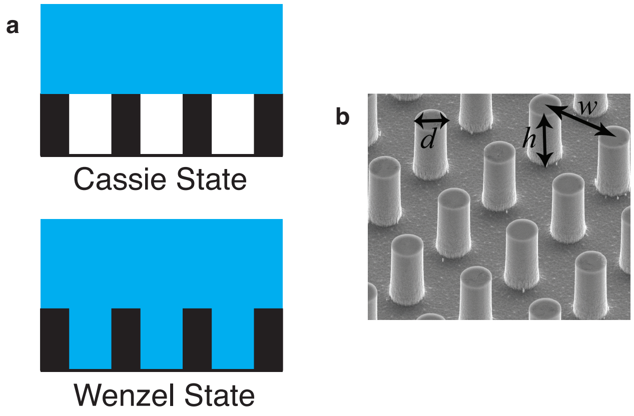

Figure 1.3: (a) Schematic drawings of liquid in the Cassie state (top) and Wenzel state (bottom). (b) SEM photograph of a superhydrophobic surface textured with pillars.

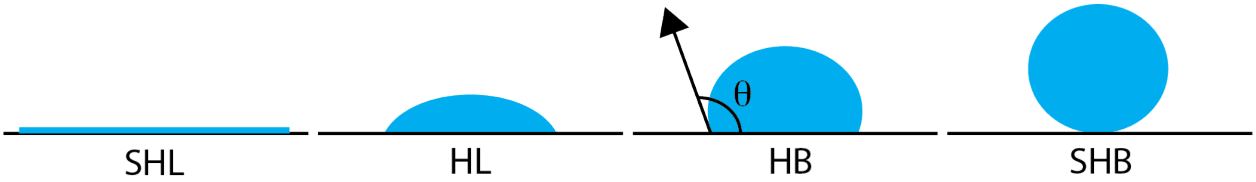

Figure 1.4: Schematic drawing of a droplet on four different types of solid surfaces varying in wettability. The definition of the static contact angle is shown on the hydrophobic surface, but the same definition applies to all surface types.

drophobicity which can significantly increase heat transfer rates in industrial condensers due to the quick removal of condensing droplets, as well as the increased surface area between vapor and solid which results from texturing.

Because of the increasing need for superhydrophobic surfaces, diverse ways now exist to quantify their effects. One of the most common is the sessile droplet contact angle test. Here, a single droplet is gently placed on the surface of interest and the resulting angle between solid and liquid, named the static contact angle, θ, is measured with a goniometer. Schematic drawings of droplets on different surfaces, as well as the orientation of θ, are shown in Fig. 1.4. Generally speaking, wettability is categorized as follows: superhydrophilic (SHL) $\theta = 0^\circ$, hydrophilic (HL) $0^\circ < \theta < 90^\circ$, hydrophobic (HB) $90^\circ < \theta < 120^\circ$ and superhydrophobic (SHB) $120^\circ < \theta < 180^\circ$.

For non-textured or smooth surfaces, the contact angle can be related to surface tensions of all three interfaces present at the boundary via Young's relation, $\sigma \cos\theta^0 = \gamma_{SG} - \gamma_{SL}$. Here, θ^0

is named the Young contact angle, γ_{SL} and γ_{SG} are the solid-liquid and solid-gas surface tension values and $\theta = \theta^0$ for smooth surfaces. On the other hand, θ on a superhydrophobic surface can be predicted as follows [14, 15],

$$\begin{gathered} \cos\theta = r\phi_s \cos\theta^0 + \phi_s - 1 \\ \cos\theta = r\cos\theta^0 \end{gathered} \tag{1.1}$$

for liquid in the Cassie and Wenzel state. The roughness factor, r, is the area of the surface divided by its normal-projected area (the second relation in Eq. (1.1) can also be applied to a SHL surface) and the solid fraction ϕ_s is the area of the top of the pillars divided by the normal-projected area of the surface. The difference between θ^0 and θ becomes clear with Eq. (1.1) in that θ, also generally referred to as the apparent contact angle, is a macroscopic characteristic of a droplet on a surface and can hence be applied to smooth or textured surfaces.

Another peculiar characteristic of SHB surfaces is that liquid flow experiences a microscopic slip velocity condition at the plane of the wall over the cavities if it remains in the Cassie state, thus reducing friction drag. Traditionally, internal or external fluid flow is said to yield the so-called “no-slip” condition at the wall when the continuum assumption is valid (technically, nanoscale slip always prevails on all surface types [16], but this magnitude of slip is negligible for the current argument). The velocity profile on a SHB wall alternates between slip and no-slip as is schematically depicted in Fig. 1.5, which results in an aggregate slip velocity at the plane of the wall. This has been confirmed experimentally and theoretically [17, 18]. The slip length, λ, is most commonly used in theoretical arguments and can be related to the slip velocity, V_s, by $\lambda = V_s/\dot{\gamma}$, where $\dot{\gamma}$ is the strain rate at the wall. Thus, λ is based on the assumption of a linear velocity profile below the wall.

Philip was the first to obtain an expression for slip length in a channel flow under laminar flow conditions with a longitudinal configuration of alternating no-slip and perfect-slip boundary conditions, as well as for a transverse configuration [18, 19],

$$\begin{gathered} \frac{\lambda_L}{w} = \frac{1}{\pi} \ln \cdot \sec((1-\phi_s)\pi/2) \\ \lambda_T = \lambda_L/2 \end{gathered} \tag{1.2}$$

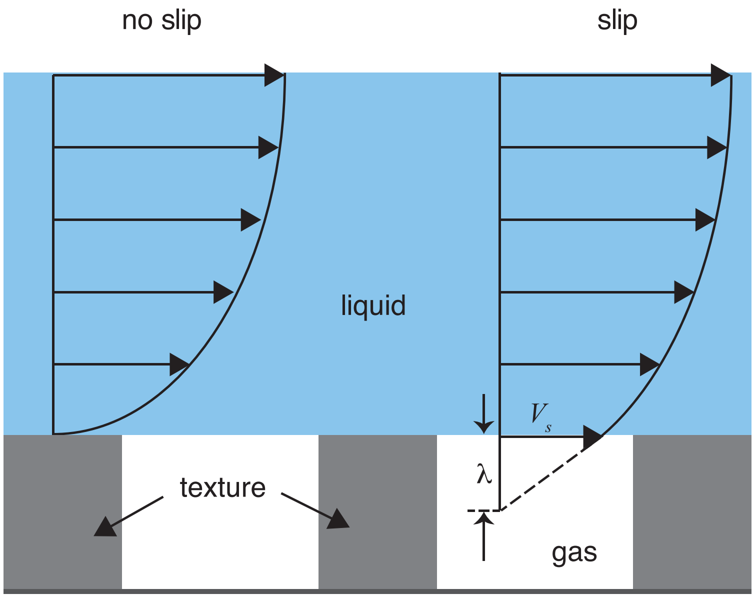

Figure 1.5: Schematic drawing of a classical no-slip velocity profile (left) and a velocity profile with slip at the wall (right).

where the subscripts L and T refer to the longitudinal and transverse direction and w is the pitch or period of the texture (Fig. 1.3). Since the work of Philip, the slip length has been determined for more complicated scenarios, including flow in a direction diagonal to the alternating wall-cavity scenario [20, 21]. A discussion on how this boundary condition was applied for droplet impingement is the essence of Chapter 2 of this dissertation.

1.1.3 Boiling

Boiling occurs when the pressure of a liquid is low enough relative to its temperature, such that liquid molecules overcome their cohesive forces and become gas. There are countless examples people run into on a regular basis, like cooking. However, boiling does not necessarily require a high temperature and hence it is actually possible to boil water at room temperature if the pressure is low enough. In this section, we focus on water boiling at ambient pressures and thus the saturation temperature of water, T_{sat}, is $\approx 100°$C. The benefits of unraveling the complex physics of boiling have extended beyond the kitchen and today affect many industrial processes including combustion, electronic and power plant cooling, material quenching, etc.

There are different types of boiling behaviors and these have been quantified into different regimes. They were first identified by Nukiyama in 1934 [22] by immersing a wire into a water bath and heating the wire electrically. He deduced the amount of thermal energy or heat flux, q'', into the water by the voltage and current supplied, and the temperature of the wire by changes to its electrical resistance [23]. He observed the following regimes with increasing excess temperature, ΔT_e (the temperature of the wire minus the saturation temperature of water): Free convection, nucleate boiling, transition boiling and film boiling. Free convection is characterized by mild boiling behavior with little or no bubbles, which largely depends on the amount of gas dissolved in the liquid and surface type. In this regime, heat flux increases linearly with excess temperature and can be described by Newton's law of cooling, $q'' = h\Delta T_e$ where h is the convection heat transfer coefficient. As temperature increases, bubbles nucleate and grow rapidly, hence the name nucleate boiling. Here, heat flux increases with much more sensitivity to excess temperature due to the latent heat released during phase change and can no longer be predicted by Newton's law of cooling. Thus, in applications where high heat fluxes are desired for extreme cooling, nucleate boiling is usually the regime of interest. As the excess temperature continues to increase, heat flux begins to decrease (transition boiling). This occurs because the rapid formation of vapor bubbles begins to insulate the liquid from the hot solid. Eventually, an entire vapor blanket forms thus reducing the heat flux to a minimum. This point is known as the Leidenfrost point, LFP, and defines the start of film boiling. If ΔT_e increases past this point, the heat flux once again begins to increase, but this time due to radiation from the hot surface.

Heat transfer for a single droplet on a heated surface is more difficult to quantify than for pool boiling due to the inability to maintain steady state. Furthermore, the lifetime of a droplet is usually on the order of tens of milliseconds [24]. Also, the temperature of the surface does not remain constant but varies widely during the lifetime of the droplet, both temporally and spatially. Surface wettability also makes a difference. Given the complexities in heat transfer, the ensued hydrodynamics have been the subject of great scrutiny, for which one of the preferred methods of analysis is high-speed photography. Fig. 1.6 shows three high-speed photographs of a water droplet boiling on an aluminum surface at 130°C. As can be seen in these images, bubbles grow due to vapor expansion and burst, which results in little droplets flying upward–a mechanism commonly referred to as secondary atomization.

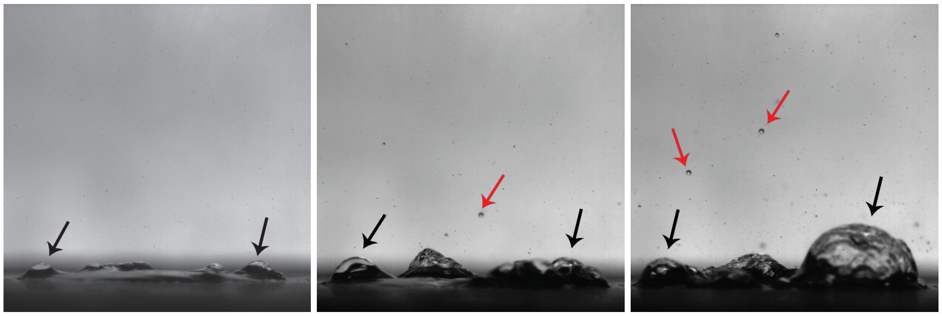

Figure 1.6: A water droplet boiling on an aluminum surface at 130°C (30 ms between images). Black and red arrows point to vapor bubbles and atomized droplets, respectively.

1.2 Current State-of-the-Art and Motivation for Current Work

In this section, a literature review is presented for the work in this dissertation, which is divided into three categories for clarity:

- Droplet impingement on a superhydrophobic surface with slip (corresponding research comprising Chapter 2).
- Wenzel to Cassie transition during droplet impingement (corresponding research comprising Chapter 3).
- Droplet impingement on superheated superhydrophobic surfaces (corresponding research comprising Chapter 4, 5).

1.2.1 Room Temperature Droplet Impingement on a Superhydrophobic Surface with Slip

A review of experimental work will be presented first, followed by analytical work. Richard and Quéré were the first to report droplet impingement dynamics on superhydrophobic surfaces with low hysteresis, $< 5^\circ$, where hysteresis is defined as the difference of contact angles at the advancing and receding front of the impinging droplet [25]. They used small droplets (~ 1 mm in diameter) which yielded high coefficients of restitution, ~ 0.9, for impingement in the low Weber number regime ($We < 7$). For larger hysteresis values, $\sim 30^\circ$, lower coefficients of restitution were obtained, ~ 0.8, and this was attributed to higher viscous dissipation. They argued coefficients of restitution close to 1 were not possible due to oscillations of the droplet following the impact, and hence a second channel for energy dissipation. Since then, studies have focused on the amount of deformation, either in terms of the height or diameter of the droplet during spreading and recoiling, as a function of impact velocity, impact diameter and Weber number [26,27]. Clanet et al. proposed that the maximum spread diameter, D_{max}, should scale as $D_0 We^{1/4}$, where D_0 denotes impact diameter, based on a balance between inertial and capillary forces [27]. He validated this scaling with experiments using water on a superhydrophobic surface and mercury on a hydrophilic surface over $10^0 < We < 10^3$.

Bouncing behavior on a superhydrophobic surface is interesting because it is tantamount to many oscillating systems in nature owing to the low friction interaction. To this end, Antonini et al. compared superhydrophobic rebound with droplets on Leidenfrost and sublimating surfaces, both of which are known to yield high coefficients of restitution [10]. A Leidenfrost rebound occurs when a droplet impinges a hot surface such that the droplet never contacts the solid but rests on its own vapor, while a sublimating rebound also sustains a vapor layer between solid and droplet but this time the vapor belongs to the solid. Their experimental data for all three surfaces collapsed onto the same curve and maximum diameter was concluded to universally scale as $D_0 We^{0.4}$ over $10^0 < We < 10^2$, which is slightly different than suggested by Clanet et al [27]. It is important to note that much of past experimental work has only focused on contact angle characteristics of a given surface, but not on specific phenotypical details such as the micro-structure arrangement. Pearson et al. were the first to investigate the effects of micro-structures for droplet impingement on anisotropic superhydrophobic surfaces made up of alternating ribs and cavities [28]. They reported that spreading and recoiling consequently occurs in an anisotropic manner, thus yielding elliptical rather than circular droplet shapes. As will be shown in Chapter 2, this motivated a predictive model developed by the current author.

Many ways exist of mathematically modeling droplet impingement on a superhydrophobic surface and one of the most common is based on a mass-spring-damper system, as shown in the schematic drawing of Fig. 1.7. Here, the kinetic energy, which the droplet carries at impact, transforms into surface potential energy as the droplet deforms. At maximum spread diameter, kinetic energy vanishes since the droplet stops before reversing directions, while potential energy reaches its maximum. During recoil, energy transfer resumes but this time from potential energy to kinetic energy. Through the entire process, velocity gradients, ∇V, cause the total energy, E_T,

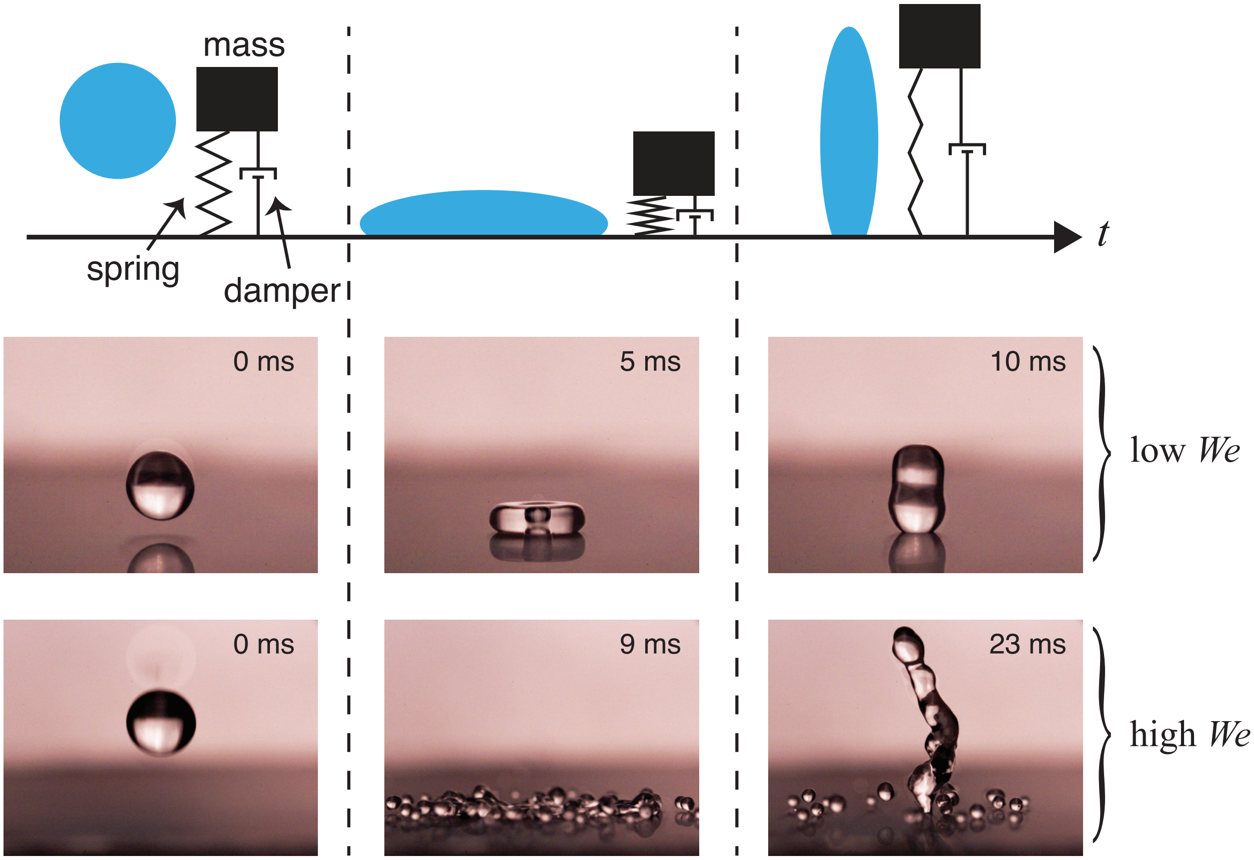

Figure 1.7: Schematic of mass-spring-damper system commonly used to model droplet impingement. High-speed photographs represent impingement on a superhydrophobic surface for $We = 10$ and 350, respectively.

(kinetic plus potential) to decrease with time due to frictional dissipation and it can be modeled as

$$\frac{d}{dt}(E_T) = -\int \mu (\nabla V)^2 d\Omega \tag{1.3}$$

where the term on the right side of the equation represents dissipation of energy with t, μ and Ω representing time, dynamic viscosity and droplet volume. The high-speed photographs in the bottom two panels of Fig. 1.7 show that the mass-spring-damper system qualitatively mimics real-life behavior relatively well for low Weber numbers. However, At high Weber numbers, the droplet splashes, a phenomenon which the model is unable to capture.

In order to solve Eq. (1.3), a representative droplet shape must first be assumed and the two most common examples include a truncated sphere or a cylinder as shown in Fig. 1.8. This

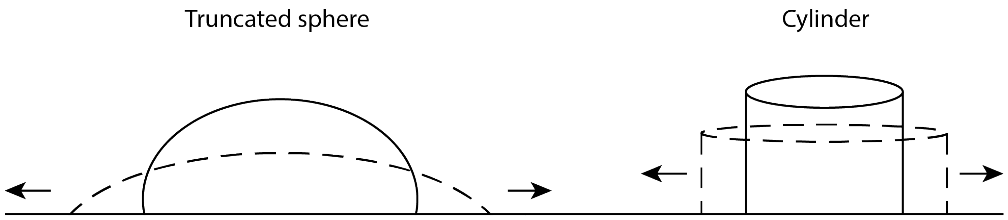

Figure 1.8: Schematic drawings of truncated sphere and cylindrical shapes used to model droplet impingement.

assumption makes it possible to define surface energy at any time. Second, a velocity field within the droplet is also assumed in order to obtain a value for kinetic energy and dissipation, where the two most common scenarios are shear-free flow and shear flow based on linear velocity gradients. Other assumptions commonly made include negligible dissipation at the triple contact line, a constant contact angle and negligible evaporation through time.

Bechtel et al. proposed a model based on the truncated sphere assumption and evaluated the temporal evolution of the height of the film for different Weber numbers, viscosities and surface tension values [29]. They compared their results with Wachters and Westerling [30] who had investigated droplet impingement on surfaces heated above the Leidenfrost point 15 years earlier. The agreement was mediocre, with the model over predicting spreading and retraction rates, as well as maximum spread diameters by 10% to 15%. Attane et al. later developed a model following the cylinder-shape approach, which predicted experimental data within a few percent [31]. They assumed a linear shear flow velocity profile which allowed them to obtain kinetic energy, E_k, and viscous dissipation, Φ, as follows

$$\begin{gathered} E_k = \frac{1}{2}\rho \int (V_r^2 + V_z^2) d\Omega \\ \Phi = 2\mu \int \left[(\frac{\partial V_r}{\partial r})^2 + (\frac{V_r}{r})^2 + (\frac{\partial V_z}{\partial z})^2 + \frac{1}{2}(\frac{\partial V_r}{\partial z} + \frac{\partial V_z}{\partial r})^2 \right] d\Omega \end{gathered} \tag{1.4}$$

where r and z represent the radial and vertical direction (in subscript form, these variables denote trajectory of variable in that direction). They also accounted for dissipation at the rim of the spreading of the droplet, which others had neglected up to this point. Their model showed good agreement with the experiments of others for $10^0 < We < 10^3$ including the foundational work by Clanet et al. presented above [27].

Though several models had been proposed to date, none had considered the effects of slip. This lack motivated the work that shall be presented in the second chapter of this dissertation. The author builds on previous models by incorporating slip as a boundary condition at the solid-liquid interface. Slip effectively reduces viscous dissipation and thus the total energy of the droplet is expected to remain higher for all time yielding larger maximum spread diameters and larger recoiling speeds. This was recently shown to be true by the author [32], both analytically and experimentally, and is the epitome of the Chapter 2. A second model is constructed by the author, also discussed in chapter 2, which is able to predict behavior on a surface with anisotropic slip. It was found that the droplet spreads in an elliptical manner in this case and these effects increase with increasing *We*. Experiments were also performed on anisotropic superhydrophobic surfaces and validated the model.

1.2.2 Wenzel to Cassie Transition During Droplet Impingement

As mentioned earlier, liquid on a superhydrophobic surface can exist in either of two states: Cassie or Wenzel, where Cassie refers to liquid sitting on the peak of the micro-texture and Wenzel to liquid wetting the grooves. Such a microscopic characteristic can exert influence that is noticed at the macroscale. For example, a droplet was shown to exhibit a much larger contact angle in the Cassie, $\theta = 170^\circ$, than when in the Wenzel state, $\theta = 130^\circ$, in the case of a flat surface decorated with microscopic spikes [33]. Both states still yield $\theta > 120^\circ$ and are thus still considered superhydrophobic interactions. Lafuma and Quéré reported that in addition to static contact angle effects, the hysteresis is another variable, which highly depend on the state of the liquid [34]. They measured a hysteresis of 5° in the Cassie state but, strikingly, 100° in the Wenzel state. Channel flow can also exhibit significant differences between these states [35]. Woolford et al. reported a reduction of 11% in the friction factor for Cassie-stable turbulent flow relative to a smooth channel, whereas no reduction was obtained for Wenzel flow [17]. Their results showed good agreement to accompanying numerical and analytical results, where drag reduction was attributed to slip at the wall.

Thus we see that many superhydrophobic advantages including droplet removal and drag reduction are only possible under Cassie state conditions. This state, however, is metastable meaning that fluctuations in the pressure of the liquid can induce it into the Wenzel state. It is therefore of practical importance to investigate parameters that govern this transition such that transition into the Wenzel state is hindered or reversal back to the Cassie state is possible. To this end, Sun et al. fabricated a superhydrophobic surface by coating a wall with aligned carbon nanotubes with temperature-responsive polymer poly(N-isopropylacrylamide) [36]. They observed that wettability, quantified via the sessile droplet contact angle test, was sensitive to small temperature variations, oscillating between 25°C and 40°C. In a different study, Krupenkin et al. investigated the Wenzel to Cassie transition of a water droplet by increasing the substrate temperature and boiling the penetrated liquid at the interface, which restored the droplet back to the Cassie state [37]. Other approaches have included electrolysis [38], magnets [39] and vibrations [40].

Analytical efforts have also been made from interfacial energy considerations. Consider a superhydrophobic surface made up of square posts as shown in Fig. 1.9. It has been shown that Cassie or Wenzel energy levels, U_C and U_W, respectively, can be defined as the surface tension at every immiscible interface multiplied by the area over which it acts [41],

$$\begin{gathered} U_C = \gamma_{SL} a^2 + \sigma(b^2 + 2ab) + \gamma_{SG}(b^2 + 2ab + 4aH) \\ U_W = \gamma_{SL}[(a+b)^2 + 4aH] \end{gathered} \tag{1.5}$$

where a, b and H represent the post length, cavity length and post height, as shown in the figure. Thus, the geometry of the superhydrophobic surface defines the energy landscape between both states, where both are local energy minima thus making an in-between state unlikely at equilibrium. Furthermore, it has been found that even when one state is energetically favorable, the liquid may dwell in the other state due to the associated energy necessary to transition from one to the other, or the so-called energy barrier [42].

Transition from the Wenzel to the Cassie state is difficult because of the mentioned energy barrier and thus has only been achieved aggressively, as stated earlier. The current author shows it is possible to passively transition from the Wenzel to the Cassie state (addressed in Chapter 4) by increasing the energy differential between the two energy states and decreasing the energy bar-

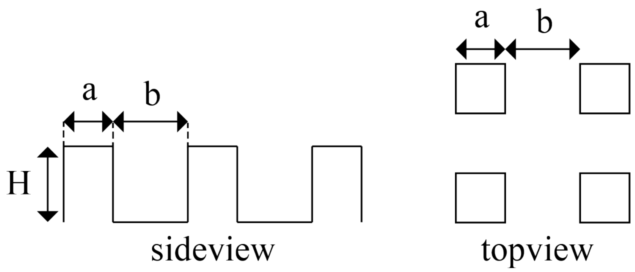

Figure 1.9: Side and top view of a square pillar array textured surface.

rier by increasing local temperature, all during a droplet impingement event. Experimental data is presented over a wide range of surfaces (varying pillar pitch and height) and temperatures. A scaling argument is constructed based on interfacial energy as the driving mechanism and dissipation caused by the moving contact line.

1.2.3 Droplet Impingement on a Superheated Superhydrophobic Surface

Extensive research has been performed for droplet impingement on hot surfaces. However, aluminum, steel and copper (hydrophilic) are normally used as test surfaces given their wide use in industry [8], and thus droplet impingement on hot superhydrophobic surfaces remains largely unexplored. A brief description is given here for impingement on hydrophilic surfaces. For surface temperatures in the range of $100°\mathrm{C} < T_s < 110°\mathrm{C}$, droplets spread and remain adhered to the surface with minimal boiling behavior. For higher surface temperatures up to $\sim 300°\mathrm{C}$, vapor bubbles form within the droplet and burst resulting in the ejection of tiny droplets, which is referred to as secondary atomization [43]. A high-speed event of secondary atomization on a textured hydrophilic surface is shown in Fig. 1.10. Heat transfer is significantly higher in this regime, which results from the induced phase change [24]. As surface temperature continues to increase, atomization slowly starts to decrease until it ceases completely. The temperature at which atomization disappears is known as the Leidenfrost point (LFP), where a vapor layer insulates the water from the heated surface [44] and occurs between 300°C and 400°C depending on the impact velocity [9, 24]. The heat transfer significantly decreases in this regime. Finally, as surface temperature continues to increase above the LFP, atomization eventually resumes once again [11]. This is due to increasing heat transfer into the liquid through thermal radiation.

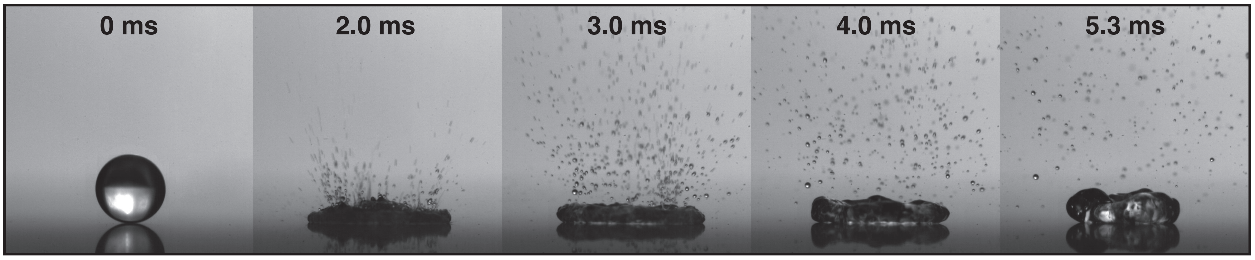

Figure 1.10: Droplet (5 μL) impinging at 0.3 m/s on a textured hydrophilic surface maintained at a temperature of 275°C.

The Weber number also plays a significant role with impingement dynamics. The LFP has been found to increase with increasing Weber number and is thus more appropriately termed the Dynamic Leidenfrost point [9, 11, 45]. This relationship has been attributed to higher vapor production being necessary to maintain a stable vapor layer between solid and liquid. Above the LFP, the Weber number exerts a similar influence to impingement on a superhydrophobic surface at room temperature. Namely, peripheral separation of droplets occurs for sufficiently high Weber numbers ($We > 100$) due to higher inertia at impact [8]. Surface roughness (superhydrophilicity) has been found to decrease the temperature at which the LFP occurs [11], although this is still a matter of debate because opposite observations have been made [46–48].

Because studies have focused on hydrophilic surfaces, information on hydrophobic or superhydrophobic surfaces is lacking. Hydrophobic and superhydrophobic surfaces are expected to yield significantly different behavior for droplet impingement on superheated surfaces because of what is known about the way vapor bubbles nucleate, grow and attach to a solid surface during pool boiling. It has been shown that during boiling, vapor bubbles spread out and adhere to hydrophobic surfaces for a longer period of time prior to rising to the liquid-air surface, which is in contrast to hydrophilic surfaces where bubbles bead up and rise more quickly [49, 50]. Because of the apparent attraction between vapor bubbles and hydrophobic surfaces, the vapor blanket at the Leidenfrost point can be formed at a lower temperature [51]. It is expected that a reduction in Leidenfrost temperature also occurs for droplet impingement on a hydrophobic surface. Furthermore, impingement dynamics on a superheated superhydrophobic surface may exhibit further differences due to the ability of water to remain above the texture.

To the author's knowledge, only three previous studies have explored droplet dynamics on heated hydrophobic or superhydrophobic surfaces. One of these studies investigated droplet impingement dynamics on textured hydrophobic surfaces, but focused on measuring heat transfer at the interface [52], leaving the ensued hydrodynamics unresolved. In a different study, Li et al. presented high-speed image analysis of droplet impingement on heated surfaces across the entire wettability spectrum but the highest surface temperature explored was 110°C [53]. The last study which pertains droplet dynamics on superheated superhydrophobic surfaces was performed by Hays et al. but he only considered the sessile droplet case ($We = 0$). They reported mitigated boiling behavior relative to a smooth surface [54]. Thus, we were motivated to pursue the investigation of droplet impingement on superheated hydrophobic and superhydrophobic surfaces, which is the subject of Chapters 4 and 5 of this dissertation. The surface temperature and Weber number ranges explored include 100°C - 415°C and 10 - 220, respectively.

1.3 Dissertation Organization

Subsequent chapters are arranged as follows. Chapters 2 through 5 contain stand-alone manuscripts that have either already been published, are under review, or will soon be submitted. As such, each chapter contains a brief introduction, methodology, results and discussion and conclusions sections. Chapter 2 demonstrates that the maximum diameter attained by a droplet impinging on a superhydrophobic surface depends on the amount of slip. This dependency is shown for both isotropic and anisotropic slip and analytically as well as experimentally. Chapter 3 deals with the thermodynamic dependence of the Cassie to Wenzel transition during droplet impingement. Once again, analytical and experimental approaches are used here. The following two chapters, 4 and 5, cover boiling hydrodynamics for a droplet impinging on superheated superhydrophobic surfaces. Chapter 4 presents a comprehensive analysis of droplet impingement on surfaces across the entire wettability spectrum: superhydrophilic, hydrophilic, hydrophobic and superhydrophobic, while Chapter 5 discusses more in-depth dynamics for atomization on different superhydrophobic surfaces with pillars of varying height and pitch. Finally, conclusions are presented in Chapter 6 to summarize all the work.

CHAPTER 2. EFFECTS OF ISOTROPIC AND ANISOTROPIC SLIP ON DROPLET IMPINGEMENT ON A SUPERHYDROPHOBIC SURFACE

This chapter is published in the journal Physics of Fluids. The formatting of this paper has been modified to meet the stylistic requirements of this dissertation.

2.1 Contributing Authors and Affiliations

Cristian E. Clavijo, Julie Crockett, Daniel Maynes Department of Mechanical Engineering, Brigham Young University, Provo, Utah 84602

2.2 Abstract

The dynamics of single droplet impingement on micro-textured superhydrophobic surfaces with isotropic and anisotropic slip are investigated. While several analytical models exist to predict droplet impact on superhydrophobic surfaces, no previous model has rigorously considered the effect of the shear-free region above the gas cavities resulting in an apparent slip that is inherent for many of these surfaces. This paper presents a model that accounts for slip during spreading and recoiling. A broad range of Weber numbers and slip length values were investigated at low Ohnesorge numbers. The results show that surface slip exerts negligible influence throughout the impingement process for low Weber numbers but can exert significant influence for high Weber numbers (on the order of 10^2). When anisotropic slip prevails, the droplet exhibits an elliptical shape at the point of maximum spread, with greater eccentricity for increasing slip and increasing Weber number. Experiments were performed on isotropic and anisotropic micro-structured superhydrophobic surfaces and the agreement between the experimental results and the model is very good.

2.3 Introduction

This paper is concerned with the dynamics of a droplet impinging on a superhydrophobic surface with slip. Since the early work of Herminghaus on the effective surface energy between a non-wetting liquid and a rough surface [55], the interaction between droplets and superhydrophobic (SH) surfaces has been rigorously explored due to its many industrial applications including self-cleaning technology [56] and drop-wise condensation [40]. Furthermore, as interest in micro- and nano-engineering grows, droplets will only receive increasing attention due to their ability to act as micro-chemical reaction chambers with a highly controlled environment, repeatability and scalability [57]. Cellular biology [58], forensic sciences [59], and lab-on-a-chip technology [60] are a few examples of fields that have already been directly impacted by improvements in droplet translation, manipulation, and transport phenomena.

When a droplet impinges on a SH surface, the droplet spreads out to some maximum diameter after which the inward pull of surface tension causes the droplet to recoil and eventually rebound. SEM images of SH surfaces used in this work are shown in Figure 2.1 (a) and (b), where the pitch, w, and the ratio of the cavity area to the total projected area as the cavity fraction, F_c, are shown. Friction resisting the flow of liquids over SH surfaces is generally reduced due to a nearly shear-free condition at the liquid-air interface above the cavities (given a low viscosity fluid in the cavities [61]), though exceptions to this trend have been observed for protruding menisci [62]. A common simplification for the alternating slip and no-slip behavior that prevails above the cavities and solid features, respectively, is to consider a spatially-uniform aggregate slip. The aggregate non-zero velocity at the wall is referred to as the slip velocity, V_s, and the wall-normal distance into the wall where the extrapolated velocity profile would reach zero, assuming a constant strain rate, $\dot{\gamma}$, is commonly termed the effective slip length, $\lambda = V_s/\dot{\gamma}$ [63], which increases as cavity fraction and/or pitch increases. λ values been solved for Stokes flow on pillars [64] and ribs [65–69]. Because slip directly impacts dissipation of energy at the wall, it is logical to conclude that droplets would spread farther during impingement (depicted in Figure 2.1 (c)), as has been observed for jet impingement scenarios [70,71]. Effective slip length values as high as 60 μm on SH surfaces have been previously reported for Cassie stable flows [72–74]. It is worth emphasizing that despite all SH surfaces generally exhibiting high contact angles, not all inherently yield significant slip since the latter is increasingly more sensitive to large cavity fraction and large pitch values.

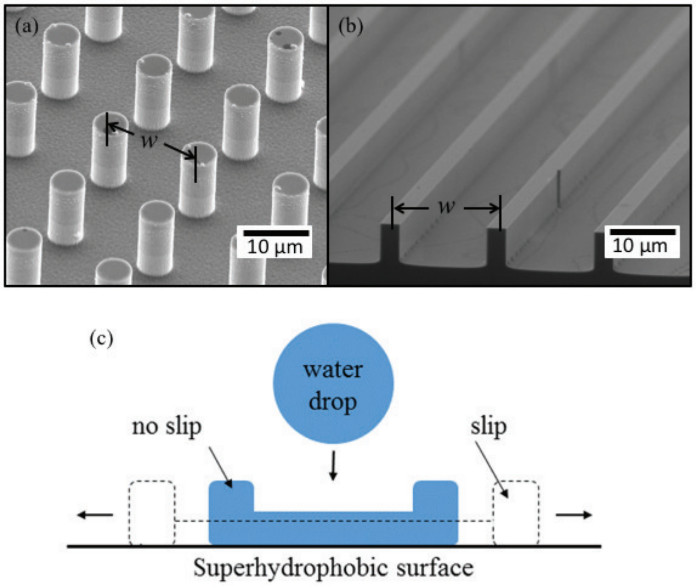

Figure 2.1: (a) and (b) SEM images of the two types of superhydrophobic surfaces used in this work. (c) Schematic of a water drop impinging on a superhydrophobic surface where slip promotes larger spreading diameters.

Some of the earliest experimental work addressing droplet impingement on SH surfaces found the contact time of an impinging droplet (the total time a droplet spends in contact with the solid surface) , was shown to be independent of impact velocity over the Weber number range $0.3 < We < 37$, where $We = \rho V_o^2 D_o / \sigma$. Here, ρ is density, V_o and D_o are velocity and diameter at impact, and σ is liquid-air surface tension [75]. Antonini et al. [2] conducted water droplet impingement experiments over a broad range of surface types from very hydrophilic to superhydrophobic. Their data revealed that the maximum spread diameter decreases for surfaces with increasing contact angles, θ, over the range $48^\circ < \theta < 166^\circ$, due to the increased attraction between water and hydrophilic surfaces. A later study by this same group on droplet rebound revealed that the maximum spread diameter was slightly larger for droplets that made no contact with the surface during impingement (due to sublimating and Leidenfrost effects) indicating that the shear stress at the wall may play a significant role during spreading [76].

Droplet impingement on azimuthally-varying wall shear stress surfaces was first explored by Pearson et al. by using anisotropic SH surfaces with alternating ribs exhibiting high cavity fractions (80% to 93%) and relatively large pitch (40 μm) [77]. They observed that a droplet spreads farther and faster in the direction along the ribs than in the transverse direction providing further evidence that the shear stress at the wall can play a significant role even for a single impingement event. This is in agreement with the work of Crowdy who mathematically showed that the effective slip length along the direction of the ribs is twice that for the transverse direction [66]. However, no analytical model was employed by Pearson et al. to explore the underlying mechanism causing their observations.

Theoretical aspects of droplet impact began with Madejski who proposed a differential energy balance model which accounted for surface energy and kinetic energy based on a two-dimensional axisymmetric cylindrical flow field [78]. A truncated sphere model has since also been developed [79]. More recently, Attane et al. improved on the cylinder model by accounting for dissipation caused by the lamellar rim, resulting inbetter correlation to empirical data than other models previously reported over a broad range of contact angles, Weber numbers and Ohnesorge numbers, where $Oh = \mu/\sqrt{\rho \sigma D_o}$ (μ is the dynamic viscosity of the liquid). While these models allow for contact angles commonly observed on SH surfaces, none considerthe effect of slip, which is surprising since slip has been shown to alter flow dynamics for many other scenarios including jet impingement [70, 71, 80–82] and channel flow [69, 83, 84].

In this work, we present an analytical model capable of predicting droplet spreading dynamics on SH surfaces with non-negligible slip. It is based on an energy conservation approach taking into consideration surface energy, kinetic energy, and dissipation. Results show that slip can cause effects which existing models are unable to predict. Furthermore, a two dimensional model able to handle anisotropic slip behavior for the case of droplet impingement is presented for the first time. Experiments were also performed on isotropic and anisotropic SH surfaces to validate the models and very good agreement was found.

Section 2 of this paper presents the analytical model derivation, followed by surface fabrication and experimental methodology. Results of both the model and experiments are presented and discussed in Section 3 for the isotropic and anisotropic cases over a broad range of governing parameters. Finally, Section 4 will present the conclusions of this work.

2.4 Methodology

2.4.1 Theory

Isotropic Model

A differential model for post-impact droplet spreading and recoiling is now developed based on conservation of energy. The liquid droplet is assumed to maintain the shape of a cylinder while in contact with the surface where a shear flow velocity field exists. Similar approaches have been widely employed in the past [3, 78, 85] and thus will only be briefly described.

A temporal conservation of energy model based on the exchange between surface energy, E_σ, and kinetic energy, E_k, including viscous dissipation, Φ, is as follows

$$\frac{d}{dt}\left(E_\sigma + E_k\right) + \Phi = 0, \tag{2.1}$$

where t is time and gravitational effects are negligible. Individual terms are defined as

$$E_\sigma = \sigma\left(\pi R^2 + 2\pi RH - \pi R^2 cos\theta\right), \tag{2.2}$$

$$E_k = \frac{1}{2}\rho\int_\Omega \left(V_r^2 + V_z^2\right) d\Omega, \tag{2.3}$$

and

$$\Phi = 2\mu\int_\Omega \left[\left(\frac{\partial V_r}{\partial r}\right)^2 + \left(\frac{V_r}{r}\right)^2 + \left(\frac{\partial V_z}{\partial z}\right)^2 + \frac{1}{2}\left(\frac{\partial V_r}{\partial r} + \frac{\partial V_z}{\partial z}\right)^2\right] d\Omega \tag{2.4}$$

In the above equations, σ, ρ, and μ are the liquid surface tension, density, and dynamic viscosity, respectively. R, H, and Ω are the radius, height, and volume of the droplet, respectively, and θ is the apparent static contact angle. r and z are the radial and axial coordinates, and V_r and V_z are the radial and axial velocity components, respectively. The model does not account for hysteresis and thus θ remains constant throughout the event. However, it will be shown in Section 2.1.3 that the model can predict dynamics on a SH surface with hysteresis as high as 20° with good accuracy.

The terms on the right side of (2.2) represent the surface energy along the top, side, and bottom area of the cylindrical droplet. The velocity field, $\vec{V}$, necessary for (2.3) and (2.4) is defined as

$$\vec{V} = \begin{bmatrix} V_r \\ V_z \end{bmatrix} = \begin{bmatrix} Crz \\ -Cz^2 \end{bmatrix} \tag{2.5}$$

where C is a constant that can be obtained by setting the time rate of change of the periphery of the droplet, dR/dt, equal to the average radial velocity at the periphery as follows

$$\frac{dR}{dt} = \frac{1}{H}\int_0^H V_r(r = R)dz \tag{2.6}$$

Both the surface and kinetic energy terms were normalized by their corresponding values for a spherical droplet immediately before impact, defined as

$$E_{\sigma,o} = \sigma \pi D_o^2 \tag{2.7}$$

$$E_{k,o} = \frac{1}{2}\rho \Omega V_o^2 \tag{2.8}$$

where D_o and V_o are the droplet diameter and velocity at impact. The viscous dissipation term was normalized by

$$\Phi_o = \mu \left(\frac{V_o}{D_o}\right)^2 \frac{\pi D_o^3}{6} \tag{2.9}$$

After normalizing and substituting the velocity field (2.5) into (2.1), the final form of the energy balance yields a non-linear ordinary differential equation,

$$\frac{d}{d\hat{t}}\left[\hat{R}^2(1 - cos\theta) + \frac{1}{3\hat{R}}\right] + \frac{1}{12}\frac{d}{d\hat{t}}\left[\left(\frac{2}{3} + \frac{1}{45\hat{R}^6}\right)\left(\frac{d\hat{R}}{d\hat{t}}\right)^2\right] + 4Oh\left(3\hat{R}^4 + \frac{2}{3\hat{R}^2} + s\hat{R}\right)\left(\frac{d\hat{R}}{d\hat{t}}\right)^2 = 0 \tag{2.10}$$

where the variables denoted with a hat represent normalized quantities. The normalized droplet radius and time are defined as $\hat{R} = R/D_o$ and $\hat{t} = tV_o/(D_o We)$, where $We = \rho V_o^2 D_o/\sigma$ is the Weber number at impact. Frictional loss due to the lamellar rim is accounted for in the viscous dissipation term in (2.10) through the term proposed by Attane et al. [3], $s\hat{R}$, where $s = 1.41 Oh^{-2/3}$. This definition of s has shown good agreement with experimental data over the broad range of $1 <$

$We < 2 \times 10^3$, $0.0022 < Oh < 0.585$, and for θ as high as 170° [3]. The ranges used in this work are well within these bounds.

Having introduced the energy balance previously employed by other researchers, in which the no-slip condition prevails at the wall, we now build upon it by incorporating slip. We employ Navier's slip hypothesis [63] thus altering the boundary condition such that an apparent slip exists at $z = 0$ and fluid velocity vanishes at $z = -\lambda$. The velocity field is now expressed as

$$\vec{V} = \begin{bmatrix} Cr(z+\lambda) \\ -C(z^2+2\lambda z) \end{bmatrix} \tag{2.11}$$

where V_z was obtained by satisfying $\nabla \cdot \vec{V} = 0$. Finally, substituting the slip-altered velocity field (2.11) into (2.1) yields

$$\begin{aligned} &\frac{d}{d\hat{t}}\left[\hat{R}^2(1-cos\theta)+\frac{1}{3\hat{R}}\right]+ \\ &\qquad \frac{1}{3888}\frac{d}{d\hat{t}}\left[\frac{1}{\hat{R}^{10}}\left(2\hat{\lambda}+\frac{1}{6\hat{R}^2}\right)^{-2}\left(\frac{d\hat{R}}{d\hat{t}}\right)^2\left(6\hat{R}^6+\right.\right. \\ &\qquad \left.\left.108\hat{\lambda}\hat{R}^8+648\hat{\lambda}^2\hat{R}^{10}+\frac{1}{5}+6\hat{\lambda}\hat{R}^2+48\hat{\lambda}^2\hat{R}^7\right)\right]+ \\ &\qquad \frac{Oh}{3}\left(\hat{\lambda}+\frac{1}{12\hat{R}^2}\right)^{-2}\left(\frac{1}{18\hat{R}^6}+\frac{\hat{\lambda}}{\hat{R}^4}+\frac{6\hat{\lambda}^2}{\hat{R}^2}+\frac{1}{4}+\frac{s}{12\hat{R}^3}\right)\left(\frac{d\hat{R}}{d\hat{t}}\right)^2=0 \end{aligned} \tag{2.12}$$

The normalized effective slip length is defined as $\hat{\lambda} = \lambda/D_o$. Equation 2.12 serves as the basis for the model of droplet impingement on a surface exhibiting isotropic slip.

Two initial conditions are necessary to solve (2.12). For the first, the initial surface energy of the cylindrical droplet is set equal to the surface energy of its physical counterpart before impact (Equation 2.7) such that $\hat{R}_o = \hat{R}(\hat{t} = 0)$. While there is no real solution for $\theta > 109.4°$, Attane et al. showed that $\hat{R}_o$ obtained at this upper θ limit ($\hat{R}_o = 0.39$) is a good representation for higher θ values up to 170° [3]. For the second initial condition, the kinetic energy of the model at $t = 0$ is set equal to that of a droplet immediately before impact (Equation 2.8), which results in

$$\frac{d\hat{R}_o}{d\hat{t}} = \frac{(2\hat{\lambda}+\hat{R}_o^2/6)\sqrt{324\hat{R}_o^{10}We}}{\sqrt{6\hat{R}_o^6+108\hat{\lambda}\hat{R}_o^8+648\hat{\lambda}^2\hat{R}_o^{10}+0.2+6\hat{\lambda}\hat{R}_o^2+48\hat{\lambda}^2\hat{R}_o^7}} \tag{2.13}$$

An adaptive step-size 4^{th} order Runge-Kutta algorithm was employed to solve (2.12) with the given initial conditions. $\hat{R}$ was calculated as a function of $\hat{t}$, where realistic values of θ, $\hat{\lambda}$, Oh, and We were chosen and specified for each simulation. The range of values explored were $145^\circ < \theta < 165^\circ$, $0 < \hat{\lambda} < \infty$ and $5 < We < 250$ for $0 < \hat{t} < 0.5$ to capture both the spreading and recoiling phase. Low Oh values were used $\sim 2 \times 10^{-3}$. The results of this analysis for surfaces with isotropic slip will be presented in Section 3.1.

Anisotropic Model

When the superhydrophobic surface of interest exhibits anisotropic texturing, such as the alternating rib and cavity pattern shown in Figure 2.1 (b), an effective slip length that varies with the azimuthal direction, α, prevails. Although the same governing equations and initial conditions developed in the isotropic derivation apply here, an azimuthally-varying slip length, $\lambda(\alpha)$, must now be accounted for. For the rib and cavity scenario, $\lambda(\alpha)$ can be expressed as [66]

$$\lambda(\alpha) = \lambda_L \sqrt{cos^2\alpha + \left(\frac{sin\alpha}{2}\right)^2} \tag{2.14}$$

In (2.14), λ_L represents the slip length along the direction of the ribs (longitudinal) where $\alpha = 0^\circ$, while λ_T denotes the slip length in the direction perpendicular to the ribs (transverse) where $\alpha = 90^\circ$. λ_L can be computed from the following relation [65, 66]

$$\lambda_L = \frac{w}{\pi} ln\left(sec\left(\pi\frac{F_c}{2}\right)\right) \tag{2.15}$$

where w and F_c maintain the same definition as in the isotropic derivation.

In order to solve (2.12) with anisotropic slip, it is necessary to discritize the domain spatially and temporally. Spatially, the model was discretized in the azimuthal direction from 0° to 90° into I number of finite control volumes with a uniform slice angle of $\Delta\alpha = 90^\circ/I$. The corresponding slip length for each control volume was determined from (2.14). As the droplet spreads, control volumes with larger slip spread farther at every time step resulting in shorter control volume heights. In order to maintain a realistic spatially-uniform height, $\bar{H}$, across the entire model through time, the sum of all control volumes was set equal to the volume of the spherical droplet before impact

$$\frac{\pi\bar{H}}{I}\sum_{i=1}^{I}R_i^2 = \frac{4\pi}{3}\left(\frac{D_o}{2}\right)^3 \tag{2.16}$$

to calculate $\bar{H}$ after each time step. A 4^{th} order Runga-Kutta scheme was employed to solve the system of equations through time. Grid independence studies were carried out to ensure convergence. The final number of control volumes used in the model for the domain $0^\circ < \alpha < 90^\circ$ was 252 and the number of time steps used over $0 < \hat{t} < 0.5$ was 3200.

Influence of Contact Angle Hysteresis

Depending on the physical and chemical architecture of a SH surface, the hysteresis can range from a few degrees to several tens of degrees. Superhydrophobic surfaces explored in this work exhibit hysteresis values of nominally 10° to 20°. However, as stated in Section 2.1.1, our model assumes a constant contact angle throughout the entire event, which we now justify.

Normalized maximum diameter as a function of contact angle over the range $40^\circ < \theta < 165^\circ$ are shown in the top panel of Figure 2.2. Solid lines correspond to the model with no slip for $Oh = 0.002$ and $We = 50$ and 150. Also shown with open markers are experimental results using the advancing contact angle from Antonini et al. [2]. In the figure, D_{max}/D_o increases with We because the initial energy of the system is greater. As θ increases, there is a decreased attraction or adhesion between water and surfaces, resulting in decreased D_{max}/D_o. Both model and experimental data show that the change in D_{max}/D_o is small within the range $145^\circ < \theta < 165^\circ$. Variation in droplet diameter as a function of time is shown in the bottom panel of Figure 2.2. Model results are shown for $\theta = 145^\circ$ and $\theta = 165^\circ$ at $We = 50$ and 150, thus depicting the difference in trajectory within our maximum hysteresis range for two arbitrary initial conditions. During the spreading phase the effect of θ on diameter is minimal, whereas discrepancy increases during the recoiling phase ($\sim 10\%$ at $\hat{t} = 0.5$ for both We). A model that accounts for a varying contact angle would expectedly yield a trajectory within these bounds.

Table 2.1 presents the maximum deviation in the maximum diameter, D_{max}/D_i, the time to maximum diameter, $\hat{t}_{D_{max}}$, and the time from impact through spreading and recoiling to when the normalized diameter returns to unity, $\hat{t}_c$, for $\theta = 145^\circ$ and 165° at $We = 150$ and $Oh = 0.002$. Deviation was calculated as the percent variation for any one of these parameters, X, between

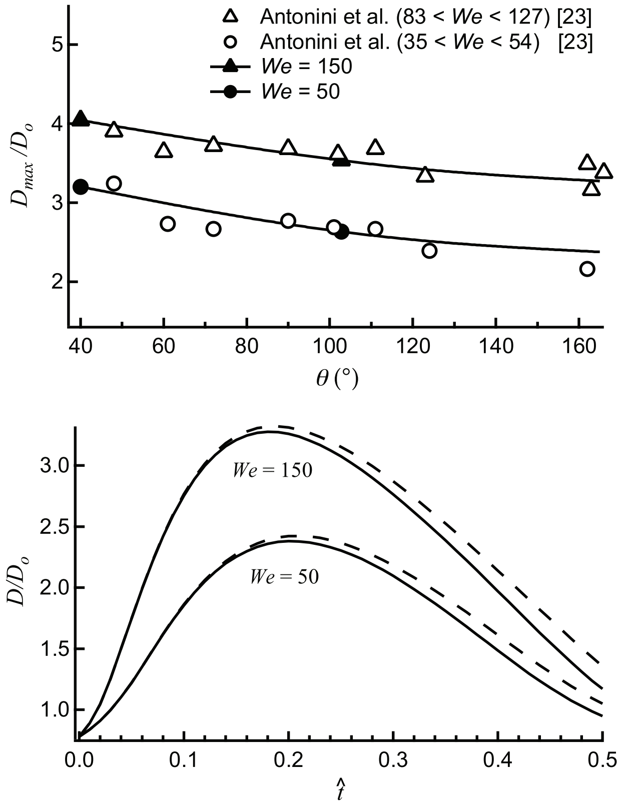

Figure 2.2: Top: Normalized maximum droplet spread diameter as a function of θ for two different values of *We*. Solid lines represent data from the theoretical model developed herein for $Oh = 0.002$ and $\hat{\lambda} = 0$, while the markers are experimental data from Antonini et al. [2] with $Oh = 0.002 \pm 0.5\%$. Bottom: Normalized diameter as a function of normalized time for $Oh = 0.002$, $\hat{\lambda} = 0$, and $We = 50$ and 150. Dashed and solid lines represent $\theta = 145°$ and 165°, respectively.

Table 2.1: Percent deviation of D_{max}/D_i, $\hat{t}_{D_{max}}$, and $\hat{t}_c$ between $\theta = 145°$ and 165° for three different slip values. Values shown are for $Oh = 0.002$ and $We = 150$.

$\hat{\lambda}$	$D_{max}/D_i(\%)$	$\hat{t}_{D_{max}}(\%)$	$\hat{t}_c(\%)$
0	1.4	2.3	1.4
0.01	1.8	2.7	4.8
0.06	3.2	3.6	4.0

$\theta = 145°$ and 165°, namely $(X_{145°} - X_{165°})/X_{145°}$. Results show that the influence of θ is small and only rises modestly with slip. We thus conclude that the use of a single contact angle in the slip model is a reasonable approximation and introduces only small error for the hysteresis values of the SH surfaces considered in this paper.

2.4.2 Surface Fabrication

Superhydrophobic surfaces were fabricated to conduct experimental validation of the model results. Two surfaces with post and rib features (Figure 2.1 (a) and (b)) were fabricated to represent isotropic and anisotropic boundary conditions, respectively. We note that while square post arrays have resulted in anisotropic behavior for thin film jet impingement dynamics in the Wenzel state [81, 82], they exhibit nearly isotropic behavior for Cassie droplet impingement flows, in spite of the localized Wenzel state at the impingement point [**?**, 86]. All surfaces were fabricated on silicon wafers using standard photolithography methods and etched using an Inductively Coupled Plasma (ICP) Reactive Ion Etcher (RIE). A 100 nm coat of chromium was thermally evaporated onto the wafers to promote adhesion for the subsequent solution of Teflon in FC-75 (0.2:100 v/v), which was spun onto the wafers and baked (330°C for 30 min) rendering them superhydrophobic. The thickness of the coat of Teflon was nominally 200 nm.

Three SH surfaces were created with approximately 20 μm tall microstructures; two with post structures and one with rib and cavity structures. Post surfaces featured pitches of 8 and 16 μm with corresponding F_c of 80% and 92%. Both exhibited an advancing contact angle of $165^\circ \pm 3^\circ$ and receding of $145^\circ \pm 3^\circ$. Effective slip lengths were estimated using the square pillar lattice correlation of Ybert et al. [64] and yielded slip lengths of 2.3 μm and 11.3 μm for the 80% and 92% F_c surfaces, respectively. The rib surface featured a 40 μm pitch and 93% cavity fraction. This surface exhibited advancing and receding contact angles of 161° and 155°, respectively, in the longitudinal direction (along the ribs), and advancing and receding contact angles of 167° and 157°, respectively, in the transverse direction. The effective slip for the rib surface was determined using (2.15) and yielded a value of 28 μm in the longitudinal direction.

2.4.3 Experimental Procedures

A syringe and needle arrangement was used to release a water droplet, driven by gravity, onto a horizontally-positioned SH surface. Droplet diameters were nominally 2.2 mm, which is below the capillary length of $a = \sqrt{\sigma/\rho g}$ and thus effects of gravity on spreading dynamics were neglected. Impact velocity was altered by adjusting the height of the needle. An APX RS Photron high-speed camera, placed parallel to the surface, captured side-view images of the impingement at 6000 frames per second. For anisotropic surface droplet impingement, images were captured in both orthogonal directions (parallel and perpendicular to the ribs). To reduce noise, the background was subtracted from all images such that only the droplet was considered at each instant in time. The impact velocity was inferred from the slope of a second-order polynomial fit to the position of the center of mass of the falling droplet.

Uncertainty in the normalized diameter was due to random error and is depicted in the subsequent figures in the following section as error bars based on a 95% confidence level, with nominally 3 - 10 samples per scenario. Calibration uncertainty did not affect the normalized diameter since the normalizing length was obtained with the same calibration. The droplet diameter and impact velocity each had an uncertainty between 0.2 and 1.1%. Fluid property uncertainty is primarily associated with temperature fluctuations of 3°C, resulting in uncertainty for density, surface tension and viscosity of 0.2%, 0.7%, and 6%, respectively. An error propagation analysis of these uncertainties yielded a total uncertainty in the Weber number of 0.9 to 3.9%.

2.5 Results and Discussion

Spreading and recoiling dynamics on surfaces with isotropic and anisotropic slip ranging the entire spectrum $0 < \hat{\lambda} < \infty$ are explored. A physically-limiting upper reference value for $\hat{\lambda}$ may be assumed to occur around 0.06, which is representative of a 1 mm diameter droplet impacting a SH surface with a 60 μm aggregate effective slip length. The infinite slip scenario represents extensional flow which would occur for a droplet spreading on a shear-free gas layer with no contact with the solid substrate. While this situation may be regarded as purely theoretical, some examples include the Leidenfrost rebound [87], sublimating solid rebound [76], and more recently, the perfect hydrophilic surface rebound [88], the former which we compare with our model for $\lambda \to \infty$ later on. In Section 3.1, we first discuss the influence of the slip length and Weber number on the spreading and recoiling dynamics for SH surfaces with isotropic slip. In Section 3.2, the influence of these parameters on SH surfaces with anisotropic slip is discussed.

2.5.1 Isotropic Slip Results

Transient Dynamics

When a droplet impinges an isotropic surface, spreading and recoiling dynamics are axisymmetric and thus results shown in this section are invariant in the azimuthal direction. Representative normalized droplet diameter as a function of normalized time are shown in the top panel of Figure 2.3. Results are shown for $We = 20$ and 150, $\hat{\lambda} = 0$, 0.02, 0.06 and ∞, where $Oh = 0.002$ and $\theta = 165^{\circ}$. For all We and $\hat{\lambda}$, the diameter increases with time (spreading phase) up to a maximum diameter, D_{max}, after which it decreases (recoiling phase) due to the inward pull of surface tension. As expected, higher We yields larger maximum diameter and higher rate of spreading due to the higher kinetic energy at impact. The no-slip model developed by Attane et al. [3] is also plotted for comparison at $We = 150$ and the results exactly coincide with our $\hat{\lambda} = 0$ results.

Introducing slip causes the droplet to spread to a larger D_{max}/D_o for either We since the flow experiences less frictional resistance. Accompanying the increase in maximum diameter is a slight increase in time to reach maximum diameter. Both of these effects occur for both We but are more noticeable at $We = 150$ because the influence of slip is proportional to the contact area covered during spreading.

Recoiling rates are expected to be lower than spreading rates since viscous dissipation during spreading leaves less energy than the initial energy of the system available for recoiling. For SH surfaces, this effect decreases until it is negligible as $\hat{\lambda} \rightarrow \infty$ since slip has a direct implication on dissipation (at $\hat{\lambda} = \infty$ no energy is dissipated). Finally, it is worth noting that D_{max} for the infinite slip case is 60% greater than the no slip case for $We = 150$. Interestingly, the influence of increasing $\hat{\lambda}$ on D_{max} asymptotes quickly with $\hat{\lambda} = 0.1$ (not shown) yielding results within 10% of the infinite slip scenario.

The bottom panel of Figure 2.3 shows model results that reveal the interplay of energy exchange between the surface and kinetic energy of the system for a typical case. Here, the energies are normalized by the total energy of the droplet just before impingement and are referred to as $\hat{E}_{\sigma}$ and $\hat{E}_k$, respectively. The data in the figure corresponds to the $We = 150$ case shown on the figure in the top panel with $\hat{\lambda} = 0$ and 0.02, and $D_o = 2$ mm. As kinetic energy is converted to surface energy during spreading, it decreases rapidly with time. This conversion process continues

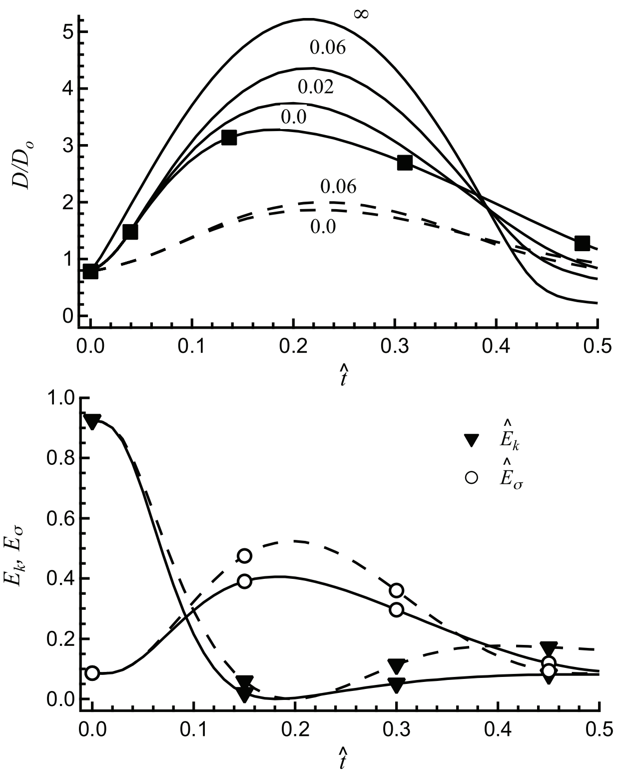

Figure 2.3: Top: Model results for normalized droplet diameter as a function of normalized time for $\theta = 165°$, $Oh = 0.002$, $We = 20$ (dashed lines) and 150 (solid lines), and $\hat{\lambda}$ values of 0, 0.02, 0.06, and ∞ as shown in the figure. Results from the model developed by Attane et al. [3] are shown as markers (■). Bottom: Model results for normalized surface and kinetic energy for $\hat{\lambda} = 0.02$ (dashed lines) and $\hat{\lambda} = 0$ (solid lines) as a function of normalized time for $\theta = 165°$, $We = 150$, $Oh = 0.002$ and $D_o = 2$ mm.

until $\hat{E}_k = 0$, which occurs at $\hat{t}_{D_{max}}$ where all energy in the system exists only in the form of surface energy and the droplet is instantaneously stationary ($d\hat{R}/d\hat{t} = 0$). Subsequently, the exchange of energy reverses, but due to viscous dissipation, the available energy at this point is significantly less than at the beginning of impingement ($\sim$40% of the initial value for the no slip case) and thus $\hat{E}_k$ does not return to its initial value. As $\hat{t} \to \infty$, $\hat{E}_k$ vanishes completely.

During the initial stages of spreading, no noticeable differences in the energy partition are observed between the $\hat{\lambda} = 0$ and $\hat{\lambda} = 0.02$ cases. Deviation becomes apparent at $\hat{t} > 0.05$ and the slip-influenced values of $\hat{E}_k$ and $\hat{E}_\sigma$ remain higher throughout the remainder of the spreading process since less dissipation occurs. Consequently, the surface energy at $\hat{t}_{D_{max}}$ is greater for the slip case, concommitant with the spread diameter being greater as shown in the top panel.

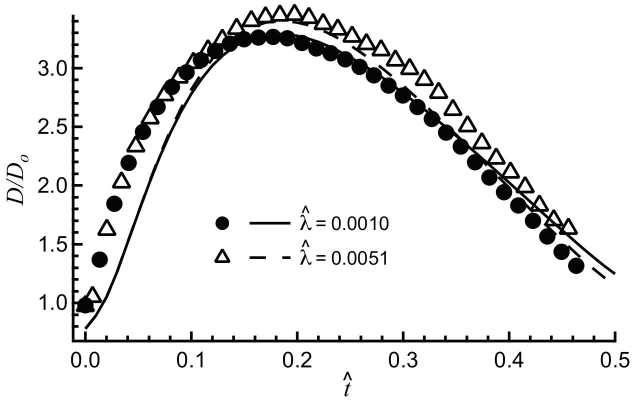

Figure 2.4: Normalized droplet diameter as a function of normalized time with $We = 155$ and $Oh = 0.0024$. Solid and dashed lines correspond to the model for $\hat{\lambda} = 0.0010$ and 0.0051, respectively. Markers (●, △) represent the experimental counterpart of the model at equivalent slip values ($F_c = 80\%$ and 92%) for a 2.2 mm initial diameter water droplet.

Next we present experimental data to compare with the model results. Figure 2.4 shows D/D_o as a function of $\hat{t}$ for $We = 155$, $Oh = 0.0024$ and for slip values of $\hat{\lambda} = 0.0010$ and 0.0051. Experiments were conducted using the $F_c = 80\%$ and 92% surfaces described previously. During the initial phase of spreading, the model underpredicts the experimental results for both scenarios. This deficiency is native to most energy balance models due to the assumed initial droplet shape and has been well documented [3]. Notwithstanding the underprediction during spreading, the model predicts the maximum diameter with good accuracy. Both the experimental and model results show that the influence of $\hat{\lambda}$ is negligible during the initial spreading phase ($\hat{t} < 0.1$), after which point deviation begins. In contrast with spreading, the model results more closely match the experimental observations during recoiling suggesting that the model is unaffected by the assumed initial droplet shape during this phase.

General Slip Effects

The left panel of Figure 2.5 shows the normalized maximum diameter as a function of We. No data is shown for $We > 200$ because peripheral splashing can occur above this point. Experimental results for both post surfaces are compared with model results at equivalent slip length values ($\hat{\lambda} = 0.0010$ and $\hat{\lambda} = 0.0051$) for $Oh = 0.0024$ and $\theta = 155°$. We make no attempt at validating the experimental results of others shown with the analytical model since slip could

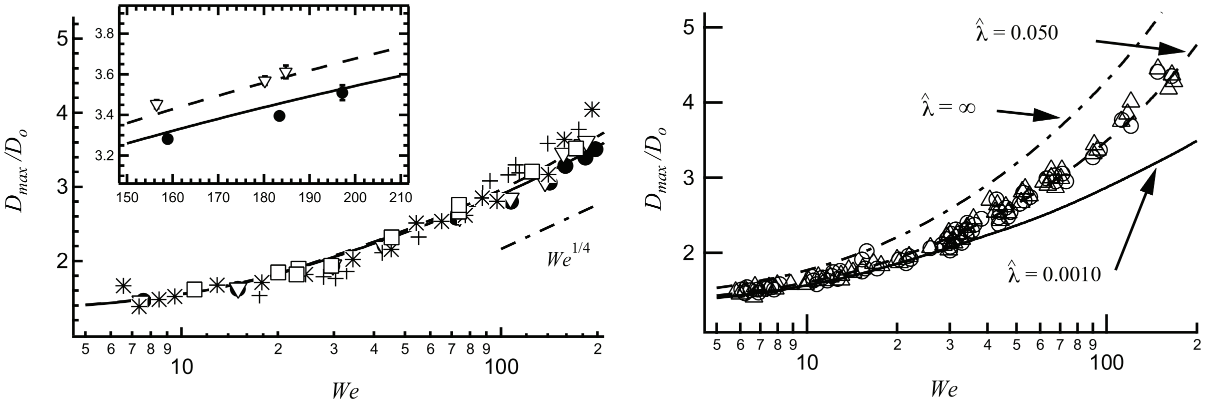

Figure 2.5: Normalized maximum diameter as a function of *We* for millimetric size water droplets on superhydrophobic surfaces (left) and hot (Leidenfrost) surfaces (right) from available literature ($Oh \sim 0.0024$). Left: (+) Antonini et al. [2], ($*$) Aria et al. [4], and (□) Clanet et al. [5]. Also shown are experimental data for the $F_c = 80\%$ (●) and $F_c = 92\%$ (▽) surfaces, as well as corresponding model results for $\hat{\lambda} = 0.0010$ (solid line) and $\hat{\lambda} = 0.0051$ (dashed line). Right: (△) and (○) are experimental results on a Leidenfrost surface from Tran et al. 2012 and 2013 [6, 7], respectively. Solid, dashed and dash-dot lines represent the model with $\hat{\lambda} = 0.0010$ ($\theta = 155°$), $\hat{\lambda} = 0.050$ ($\theta = 180°$) and $\hat{\lambda} = \infty$ ($\theta = 180°$), respectively.

not be inferred from those experiments. Clanet et al. [5] gave no detail about their SH surface characteristics except that $\theta \sim 170°$; Aria et al. [4] used a SH surface made of carbon nanotube (CNT) arrays making it impractical to obtain a representative effective slip length; and the SH surface finish of Antonini et al. [2] consisted of a random etch where only a generalized RMS could be inferred. Nonetheless, model results, as well as all experimental data, show that maximum spread diameter increases with Weber number, as expected. The dependence on $We^{1/4}$ as proposed by Clanet et al. is shown in the dash-dot line and shows good agreement with the results [5]. At low *We*, there is virtually no distinction between experiments and the analytical model, while at high *We*, there is a clearer distinction since the droplet spreads sufficiently for surface characteristics to exert influence. Generally, the analytical model serves as a good representation of the data everywhere.

A closer examination of the higher Weber number range ($150 < We < 210$) shown in the inset shows only the experiments performed in the present work, where the apparent slip can be inferred. Error bars are not shown on data points where the error was smaller than the marker size. For this *We* range, the model results show good agreement with the experimental data and

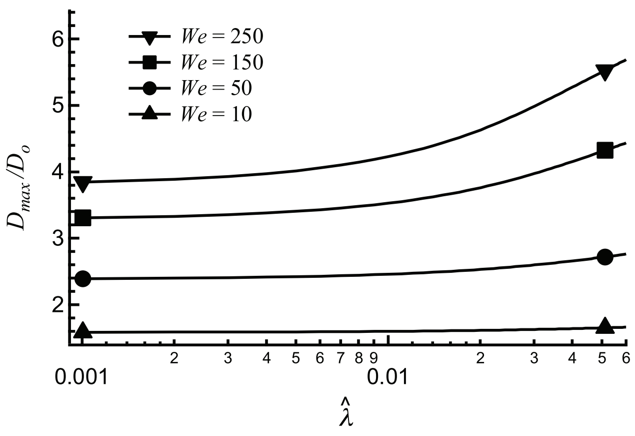

Figure 2.6: Model results for the normalized maximum diameter as a function of $\hat{\lambda}$ for $We = 10$, 50, 150, and 250. For all scenarios shown, $Oh = 0.002$ and $\theta = 165°$.

a distinctly larger maximum diameter was observed on the $F_c = 92\%$ surface due to the higher effective slip length.

The right panel of Figure 2.5 also shows the maximum spread diameter as a function of *We* but for impingement on a surface with infinite slip (dash-dot line). The solid line represents the same model results as in the left panel for $\hat{\lambda} = 0.0010$ and is plotted for comparison. Experimental data is shown from Tran et al. [6,7], who performed millimetric drop ($D_o \sim 2$ mm) experiments on surfaces above the Leidenfrost temperature, thus approximating the infinite slip scenario. The data show that the model generally over predicts the experimental results by $\sim 20\%$. This indicates that the additional friction at the wall caused by the vapor layer may not be negligible [61] and thus maximum diameter model results at infinite slip are higher for all *We*. For the sake of obtaining an approximate slip value for Leidenfrost impingement, model results for $\hat{\lambda} = 0.050$ are also shown as a representative fit to the experimental data.

The general influence of $\hat{\lambda}$ and *We* on normalized maximum droplet diameter are explored in Figure 2.6. Model results for D_{max}/D_o are plotted as a function of $\hat{\lambda}$ for *We* values of 10, 50, 150 and 250, with $Oh = 0.002$ and $\theta = 165°$ for all cases. Maximum diameter increases with increasing *We* for all $\hat{\lambda}$ as well as with increasing $\hat{\lambda}$ at constant *We*. This influence of slip is significantly more pronounced for higher *We*. For $We = 10$, there is only a slight increase in maximum diameter ($< 6\%$) over the enitre range shown whereas, for $We = 250$, the normalized maximum diameter increases 46%. At high *We*, because the thickness of the droplet gets smaller as it spreads, the influence of slip becomes more dominant. Finally, we note that because droplets that impinge

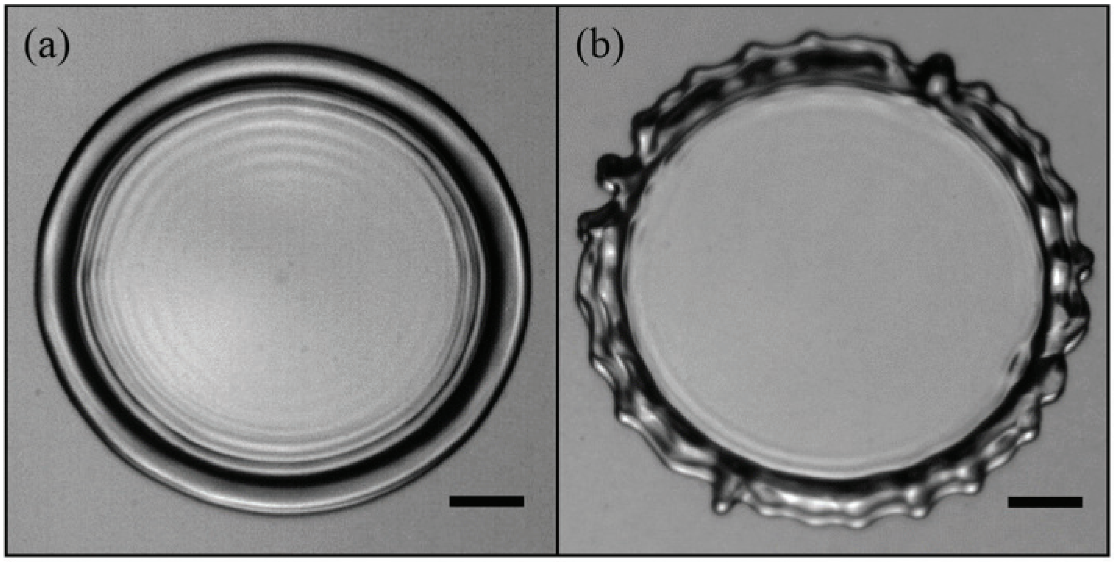

Figure 2.7: Top view images of a water droplet ($D_o = 2.2$ mm) impinging a superhydrophobic surface captured at maximum spread (~ 2.7 ms after impact) with $We = 180$ and $Oh = 0.0024$. (a) $\hat{\lambda} = 0.0010$ ($F_c = 80\%$); (b) $\hat{\lambda} = 0.0051$ ($F_c = 92\%$). The scale is 1 mm for both images.

on surfaces with higher slip may spread out significantly farther for the same initial conditions, fingering may be induced prematurely around the periphery. This phenomenon (depicted in the right panel of Figure 2.7 for $We = 180$) is characterized by a wavy lamellar rim [85,89,90].

2.5.2 Anisotropic Slip Results

An anisotropic SH surface is a surface where the slip length, λ, varies as a function of the azimuthal direction, α. Spreading and recoiling dynamics differ from the isotropic scenario in that the droplet spreads faster along the direction with less shear stress or greater slip length [77]. Figure 2.8 shows an anisotropic impingement event at $We \sim 160$. Because less resistance is associated with the longitudinal direction, the droplet spreads farther in this direction and transitions to droplet breakup earlier. The dark region in the center of the spreading droplet (left panel) represents a local transition to the Wenzel state. Given that once the liquid enters into the superhydrophobic cavities it remains stagnant, the bulk of the droplet presumably still slips above the cavities during spreading and receding. Thus, anisotropic slip behavior prevails, as will be shown in the results later in

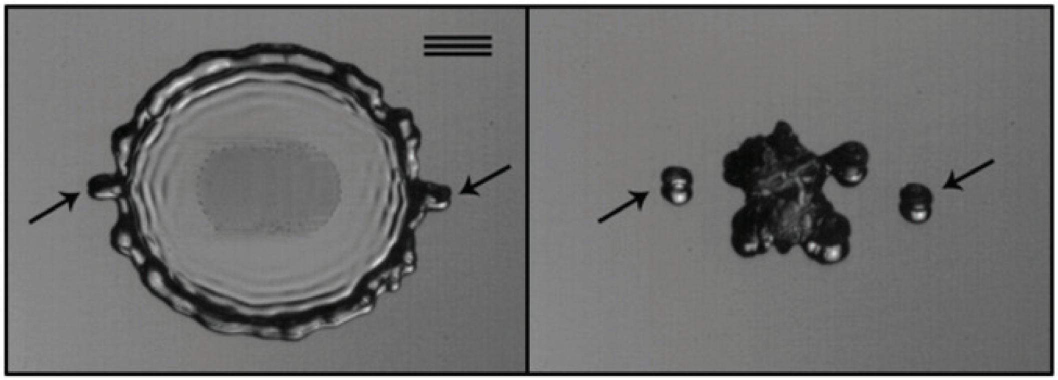

Figure 2.8: Droplet impingement on anisotropic surface at $We \sim 160$ and $t = 2.3$ ms (left) and $t = 6.3$ ms (right) after impact. Rib direction is indicated by lines in left panel. Arrows point to satellite drops that form along the direction of greatest slip, $\alpha = 0$.

this section. The influence of Weber number and slip length on the eccentricity of the spreading dynamics in the pre-splashing regime on anisotropic surfaces is the main focus of this section.

Transient Dynamics

Figure 2.9 provides D/D_o for the longitudinal and transverse diameters as a function of time for the case where $Oh = 0.0024$, $\theta = 160^\circ$, $We = 109$, and $\hat{\lambda}_L = 0.0127$ ($\hat{\lambda}_T = 0.0064$) (see (2.15)). Lines correspond to model results and markers to experiments. In the longitudinal direction, the model predicts a maximum diameter $\sim 5\%$ greater than in the transverse direction, due to larger slip length, and with a slightly later arrival time ($\sim 2\%$). Recoiling occurs faster in the longitudinal direction since the maximum diameter is greater and thus there is greater surface energy per perimeter length, in addition to greater slip. In the model, this causes the droplet diameter in the longitudinal direction to become smaller than its orthogonal counterpart at $\hat{t} \sim 0.38$, while this effect occurs experimentally outside the window of time shown.

Experimental data presented in Figure 2.9 follows the general trends predicted by the model. Longitudinal maximum diameter is predicted quite well, but the model significantly overestimates it in the transverse direction ($\sim 10\%$ overprediction). A possible explanation for this is that the azimuthal distribution of slip on a uni-directional anisotropic surface proposed by Crowdy [66]

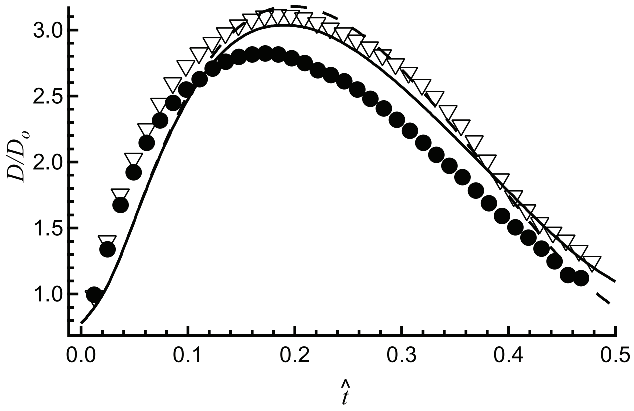

Figure 2.9: Droplet diameter in the two primary spreading directions as a function of time for impingement on an anisotropic surface. Solid line represents the transverse diameter, while the dashed line represents the longitudinal diameter. Markers (●) and (△) represent experimental data along these directions, respectively. This scenario is defined by $Oh = 0.0024$, $\theta = 160°$, $We = 109$, $D_o = 2.2$ mm, $w = 40$ μm and $F_c = 93\%$ ($\hat{\lambda}_L = 0.0127$).

(Eq. (2.14)) may overpredict the slip that exists for droplet impingement, particularly in the transverse direction. This is further evidenced by the earlier departure of the experimental data from the model predictions, which occur at $\hat{t} \sim 0.1$. A more in depth analysis of the slip profile is given in the following section.

General Slip Effects

Maximum diameters as a function of Weber number are shown in the top panel of Figure 2.10 for the same conditions as Figure 2.9. In both directions, the maximum diameter increases as Weber number increases. Additionally, the difference between the maximum diameter in both directions also increases as *We* increases, suggesting that the influence of slip for an anisotropic SH surface is magnified at higher Weber numbers. While the model predicts the longitudinal maximum spread with good accuracy, it overpredicts the transverse maximum spread by 7% to 16% in the range $110 < We < 170$, and thus underestimates the observed anisotropy.

The hydrodynamic slip length tensor provided by Crowdy [66] (Eqs (70) and (71)) is the basis for (2.14) which assumes Stokes flow and that slip prevails in both of the orthogonal directions, with $\hat{\lambda}_L = 2\hat{\lambda}_T$. Woolford et al. showed that for flow in a microchannel with SH walls exhibiting transverse ribs at non-Stokes flow Reynolds numbers, the slip length decreases with in-

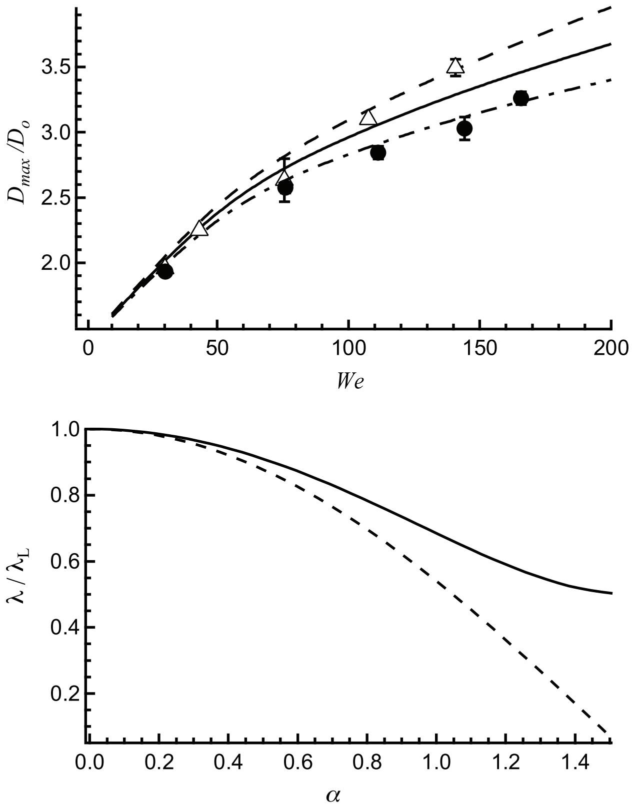

Figure 2.10: Top: Normalized maximum diameter in the longitudinal and transverse directions as a function of We. Dashed and solid lines represent the analytical model data for the longitudinal and transverse directions, respectively, employing the slip profile given by (2.14), while the markers (△ and ●) represent experimental data in these corresponding directions. Dash-dot line represents analytical model data for the transverse direction for the slip profile given by $\lambda(\alpha) = \lambda_L cos(\alpha)$. $Oh = 0.0024$, $\theta = 160^\circ$, $D_o = 2.22$ mm, $w = 40$ μm and $F_c = 93\%$ ($\hat{\lambda}_L = 0.0127$) for all cases. Bottom: Normalized effective slip length as a function of the azimuthal direction. The solid line represents Eq (2.14) and the dashed line is $\lambda(\alpha) = \lambda_L cos(\alpha)$.

creasing Reynolds number [91]. Furthermore, other work has identified a decrease in slip over an alternating solid-gas interface (as is the case in the transverse direction) for drooping mensici [62], which could likely be the case for droplet impingement given the associated high impact pressure. The implication of this is that at high Weber numbers the slip in the transverse direction is likely to be much lower than that predicted by Crowdy. While no previous researcher has presented a model to predict the slip length for droplet impingement flow over transverse ribs, we consider here the limiting case where slip in the transverse direction vanishes such that $\lambda(\alpha) = \lambda_L cos(\alpha)$. This relation, as well as (2.14), are shown in the bottom panel of Figure 2.10, and the effect on D_{max}/D_o in the transverse direction is shown in the top panel. There is very good agreement for the transverse

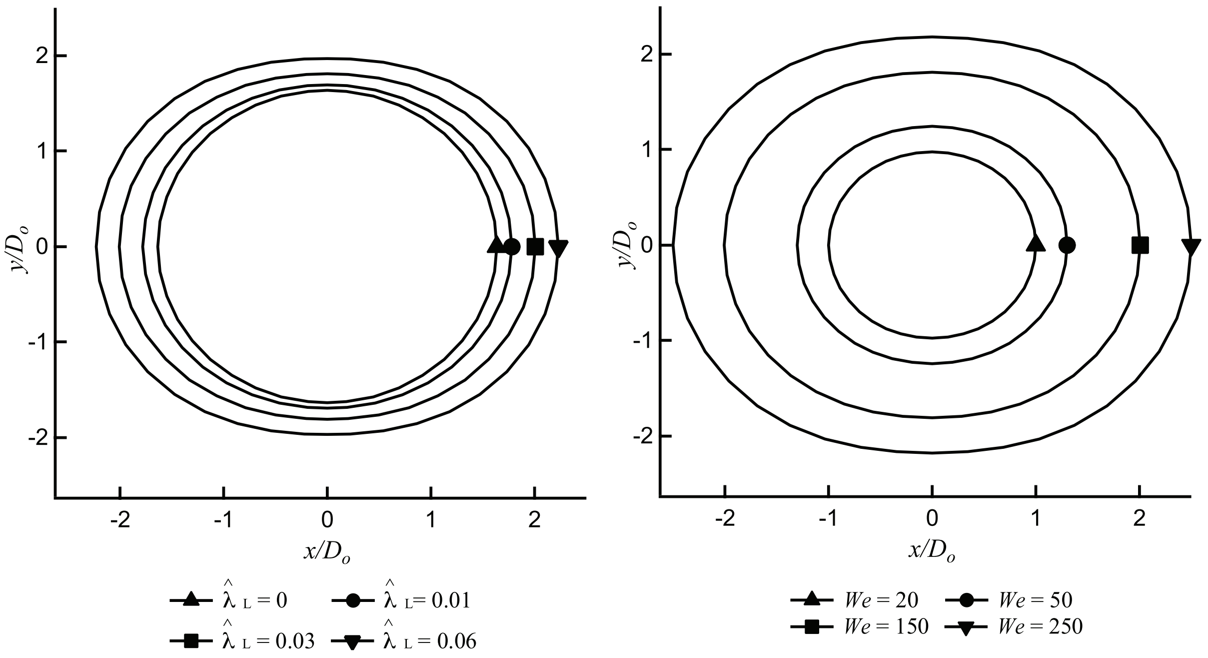

Figure 2.11: Model results for the droplet shape at $\hat{t}_{D_{max}}$ for different values of slip (left) and Weber numbers (right). The data in both figures were calculated for $Oh = 0.002$ and $\theta = 165°$. Left: $We = 150$. Right: $\hat{\lambda}_L = 0.03$.

values of D_{max}/D_o with the experimental data (longitudinal maximum diameters over the same We range are unaffected). These results demonstrate that the azimuthal distribution of slip for droplet impingement likely differs from that obtained for general Stokes shear flow. However, because an exact slip distribution for droplet impingement flow has not yet been established, the results in the following sections are based on (2.14).

Maximum Diameter Shape and Size

Model results of the shape of a droplet at maximum diameter are shown in the left panel of Figure 2.11 for $We = 150$ and $\hat{\lambda}_L = 0$, 0.01, 0.03, and 0.06, while the right panel depicts the same data for a fixed value of $\hat{\lambda}_L = 0.03$ and $We = 20$, 50, 150, and 250. For both cases, $Oh = 0.002$ and $\theta = 165°$. When anisotropic slip prevails, the droplet shape at maximum diameter is elliptical with the major axis aligned with the longitudinal direction as illustrated in the left panel of Figure 2.11. Further, as slip increases, the eccentricity of the ellipse becomes more pronounced and the diameter increases in both directions. The increase in diameter as $\hat{\lambda}_L$ increases is more pronounced for the

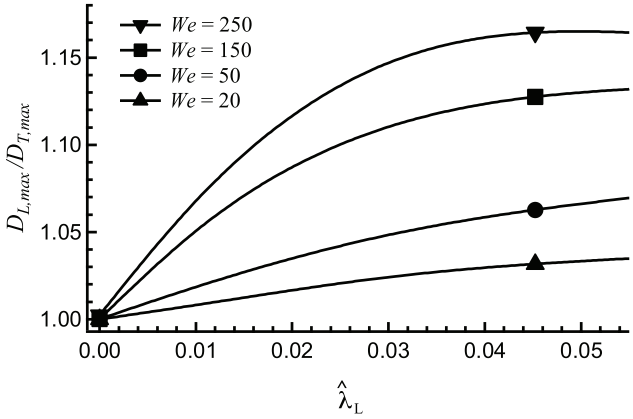

Figure 2.12: Model results for the ratio of the maximum diameter in the longitudinal direction to the transverse direction as a function of longitudinal-direction slip for *We* values of 20, 50, 150, and 250. The data shown is for $Oh = 0.002$ and $\theta = 165°$.

longitudinal direction (35% increase from no-slip) than transverse (20% increase) concomitant with the higher slip in that direction. Similarly, increasing *We* also yields an increase in the droplet eccentricity. Anisotropic dynamics captured by this model can explain the 2-pronged jet rebound phenomenon recently observed by Pearson et al. [77, 92], who also performed their experiments on alternating rib/cavity anisotropic surfaces. They reported that given moderate Weber numbers, the anisotropic droplet shape would cause a rebounding droplet to momentarily split into two jets.

To explore droplet eccentricity further, the ratios of longitudinal maximum diameter to transverse, $D_{L,max}/D_{T,max}$, are shown in Figure 2.12. The figure shows $D_{L,max}/D_{T,max}$ as a function of $\hat{\lambda}_L$ for *We* values of 20, 50, 150, and 250. It illustrates that the diameter ratio increases with increasing $\hat{\lambda}_L$ for all *We* as a result of frictional differences becoming more evident at large $\hat{\lambda}_L$. On the other hand, the behavior of the system approaches non-eccentric, zero slip behavior for very small $\hat{\lambda}_L$. Further, the figure shows that the diameter ratio increases for increasing *We* at any fixed $\hat{\lambda}_L$. At higher *We*, the rate of increase of the ratio of the diameters decreases for sufficiently large $\hat{\lambda}_L$ due to the asymptotic behavior of $\hat{\lambda}$ on the system for large slip values as discussed previously. For instance, for $We = 150$ and $\hat{\lambda} = 0.1$ on an isotropic surface, the maximum diameter is within 10% of the maximum diameter associated with infinite slip. Thus, the eccentricity of the droplet inherent of larger longitudinal slip is diminished at very high $\hat{\lambda}$ values. The value of the maximum diameter in the transverse direction therefore approaches the value of the maximum diameter in the longitudianl direction for large $\hat{\lambda}$ or simply $\lim_{\hat{\lambda}\to\infty} D_{L,max}/D_{T,max} \sim 1$.

2.6 Conclusion

Spreading and recoiling dynamics of an impinging droplet on superhydrophobic surfaces with slip were explored. A theoretical model was developed based on an energy balance including surface and kinetic energy, as well as viscous dissipation. In contrast to what has been accomplished previously, the slip length, which prevails on SH surfaces with high pitch and cavity fraction, was incorporated into the model. Additionally, a two-dimensional numerical scheme was developed to predict the impingement dynamics on SH surfaces exhibiting anisotropic slip. Both models showed good agreement with experiments performed in this work, as well as available empirical data found in the literature. Slip, over its entire physical domain ($0 < \hat{\lambda} < 0.06$), was found to increase the droplet maximum diameter significantly on both isotropic (35% for $We = 150$) and anisotropic surfaces (36%/20% in the longitudinal/transverse direction for $We = 150$). Furthermore, slip effects were magnified for increasing Weber number over the range explored here ($5 < We < 250$) on both surface types. For anisotropic SH surfaces, the droplets were found to spread and recoil in an elliptical shape. The eccentricity of the ellipse at maximum diameter increased for increasing slip and Weber number, with the major axis aligned in the direction of greatest slip. During spreading and recoiling, the fluid spread out faster and farther in the direction aligned with the ribs, concomitant with greater slip. A new azimuthal relation for the slip length of the form $cos(\alpha)$ was discussed for droplet impingement on unidirectional superhydrophobic surfaces.

CHAPTER 3. WENZEL TO CASSIE TRANSITION DURING DROPLET IMPINGEMENT ON A SUPERHYDROPHOBIC SURFACE

This chapter has been submitted for publication in the journal Physical Review Fluids. The formatting of this paper has been modified to meet the stylistic requirements of this dissertation.

3.1 Contributing Authors and Affiliations

Cristian E. Clavijo, Julie Crockett, Daniel Maynes Department of Mechanical Engineering, Brigham Young University, Provo, Utah 84602

3.2 Abstract

Superhydrophobic surfaces offer many industrial advantages such as drag reduction and self-cleaning behavior as long as the liquid remains suspended above the composite solid/gas interface (Cassie state). These advantages are hindered when liquid penetrates the gas cavities (Wenzel state), and this is commonly referred to as impalement. Current efforts to drive impaled liquid out of, or dewet, the cavities are locally-disruptive to the flow such as boiling or mechanically vibrations. In this work, we reveal that passive dewetting is possible during droplet impingement on micropillar substrates under the right thermodynamical conditions. Exploration included substrates with pillar-to-pillar spacing of 8 μm and 16 μm, pillar diameters of 3 μm and 6 μm, and pillar heights of 4 μm to 8 μm and 8 μm to 18 μm, respectively. The substrate temperature range considered was 23°C $< T_s <$ 96°C. Results revealed that dewetting increases with increasing pillar height and increasing substrate temperature. Two hypotheses for the driving mechanism are formulated based on evaporation and surface energy. First order models are consequently constructed revealing that dewetting does not occur due to evaporation, but is caused by surface energy gradients at the interface. Dissipation in the flow is taken into account due to hydrodynamic and non-hydrodynamic mechanisms; the latter is found to dominate resistance.

3.3 Introduction

The behavior of a liquid that comes in contact with a solid surface is highly influenced by the wettability of the surface [93–95]. One commonly used metric to macroscopically determine the extent of hydrophobicity is the static contact angle formed at the triple contact line, which for water is generally between 90° and 120° on a hydrophobic solid [96]. If the hydrophobic substrate exhibits nano- or micro-scale roughness, however, contact angles can exceed 150°, and such substrates are referred to as superhydrophobic (SH) [55, 77, 96]. Surface roughness allows many types of plants [97] and insects [98,99] to thrive in nature and enables unique characteristics that promote extremely low adhesion to water solutions [100]. Consequently, drag-reduction [84, 91, 101, 102], self-cleaning [56] and enhanced drop-wise condensation [40] surfaces can be realized. These characteristics are made possible by the existence of a solid/gas composite layer at the interface (Cassie state). Superhydrophobic substrates are finding use in many man-made applications ranging from medicine to microelectronics [95] and are also of great fundamental interest [71, 80, 103–106].

If liquid impregnates the cavities (Wenzel state), hereafter referred to as impalement, many of the advantages posed by the superhydrophobic effect are compromised due to the dramatic increase in apparent adhesion between liquid and solid. It is, therefore, of significant interest to understand the thermodynamic landscape between the Cassie and Wenzel state in order to avoid transition from the former to the latter or to investigate possible pathways of reversibility once impalement has occurred. The transition between these two potential energy minima [107] has indeed been of great recent scrutiny [107–117].

Whether a sessile droplet resides in the Cassie or Wenzel state depends on the architecture of the SH substrate. For instance, the pressure difference, ΔP, required for impalement on a pattern of alternating rectangular ribs and cavities decreases with increasing cavity length, l, as $\Delta P \sim l^{-1}$ and thus the likelihood of impalement increases with cavity size [108]. Other factors that play a role include the solid fraction, ϕ_s, defined as the solid area in contact with the liquid divided by the projected area; Young, or static, contact angle, θ^0; and roughness factor, r, defined as the total solid surface area divided by the projected area, which for a pillar-type arrangement depicted in Fig. 3.1a is $r = 1 + \pi dh/w^2$ (d is pillar diameter, h is pillar height and w is pillar center-to-center spacing or pitch). The concept of a critical contact angle, θ_c, was defined by Bico et al. [118] as $\cos\theta_c = (\phi_s - 1)/(r - \phi_s)$ and is plotted in Fig. 3.1b as a function of r for $\phi_s = 0.2$, which

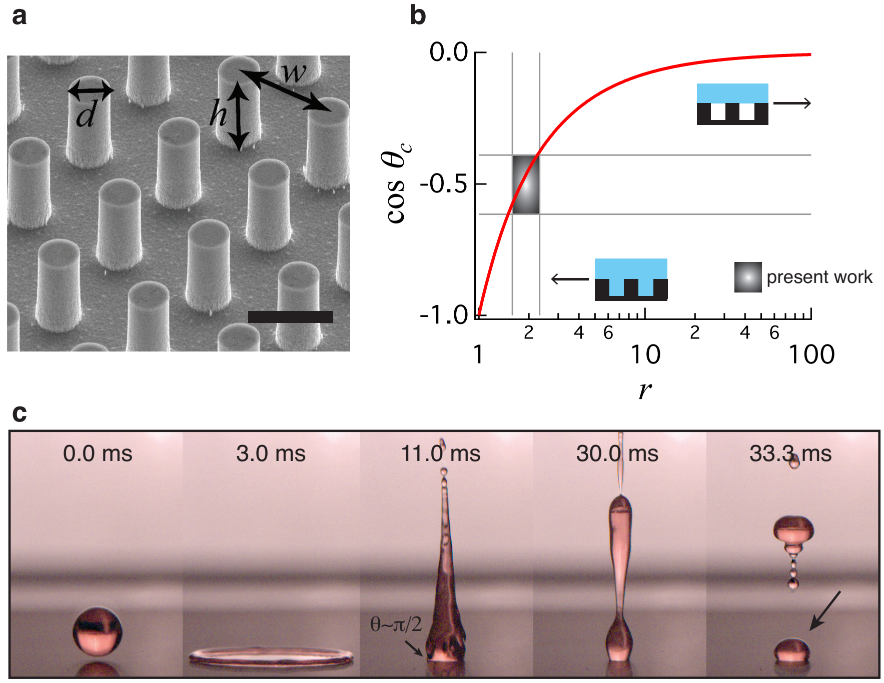

Figure 3.1: a) SEM photograph of superhydrophobic substrate used in this work. b) $cos\theta_c$ is plotted as a function of r for $\phi_s = 0.2$ where the Cassie or Wenzel state become more energetically favorable for $r \to \infty$ and $r \to 1$, respectively. c) A 3 mm diameter water droplet impacting a superhydrophobic substrate: ($t = 0.0$ ms) Prior to impact; ($t = 3.0$ ms) Maximum spread; ($t = 11.0$ ms) Apparent contact angle at the interface is no longer in the superhydrophobic regime, $\theta \sim \pi/2$; ($t = 30.0$ ms) Necking between the rebounding and the pinned liquid becomes evident; ($t = 33.3$ ms) Droplet separation has occurred and pinned liquid remains behind in the Wenzel state as indicated by the arrow.

is a typical solid fraction. If $\cos\theta^0$ is larger than $\cos\theta_c$, then the Wenzel state is highly favored and becomes increasingly more so as $r \to 1$. On the other hand, if $\cos\theta^0$ is smaller than $\cos\theta_c$, energetic favorability is given to the Cassie state.

For a Cassie droplet on a substrate with moderate r values, the Cassie state is generally said to be metastable and becomes vulnerable to impalement for bouncing droplets due to local pressure increase [119, 120]. Figure 3.1C depicts a millimetric droplet bouncing on a SH substrate for a pillar structured surface ($w = 16$ μm and $h = 18$ μm). Here, impalement occurred at impact and as the droplet rebounds, the impaled liquid leaves a smaller drop behind (time, $t \sim 33.3$ ms). These images illustrate the general frailty of micro-structured SH substrates where if several droplets continuously impact it, the substrate may not remain “dry”. Cassie stability can be enhanced by employing hierarchical substrates such as nano-scale roughness on micro-features [120, 121] or simply very tall micro-features [119], either of which effectively increases r by increasing the total solid surface area. However, moderate micro-structured SH substrates (smallest feature size $\sim 10^0 - 10^2$ μm) are often desired in droplet-impingement applications due to the associated large hydrodynamic [77, 122] and/or thermal [123] slip effects. Thus, it has become of interest to investigate impalement reversibility pathways for micro-structured substrates, which thus far has proven difficult [109, 124, 125]. We address this issue in the present work.

Impalement into a SH micro-pillar substrate during droplet impingement was reported by Reyssat et al. [119]. The pillars were 2.5 μm and 10 μm in diameter and height, respectively. Though impingement was axisymmetric, the impaled region exhibited sharp corners due to the lattice arrangement of the pillars, which coincide with the arrangement used in this work. Later, Krupenkin et al. investigated Wenzel to Cassie dynamics for a sessile ionic water droplet on micro-pillar SH substrates of similar lattice arrangement to Reyssat et al. [119], which was induced into the Wenzel state by applying voltage between the droplet and substrate [110, 125]. The temperature at the solid-liquid interface (originally at room temperature) was increased instantaneously well above saturation temperature ($> 200^\circ$C) by running a current through a thin conductive layer coated on the surface. This caused the liquid at the interface to vaporize and thus the droplet rapidly ($\sim$ 50 ms) returned to the Cassie state. While this technique achieves a Wenzel to Cassie transition, the mechanisms used may be adverse in applications where high temperatures are detrimental. Similar approaches have been attempted by other groups [126], as well as magnetism [127], electrolysis [128], vibrations [129] and more recently, hemiwicking of a low surface tension liquid [130]. However, there are no current solutions for passive transition back to the Cassie state once liquid has impaled the surface. In this paper, we discuss a mechanism through which this transition occurs during droplet impingement, which we shall refer to as “dewetting”. Specifically, we explore millimetric water droplet impingement on SH substrates composed of micro-pillar structures (Fig. 3.1a). The influence of substrate temperature (below saturation temperature of water), pillar height and pitch are quantified.

In Section 3.4 experimental and data processing methodologies are detailed. Experimental results showing the influence of substrate temperature, micro-structure height and spacing on dewetting are discussed in Section 3.5. In Section 3.6, first order models are postulated to explain the behavior and identify the mechanisms at play. Although not the primary point of the paper, the mathematical development of the observations reveal that the experiments lend themselves to the isolation of contact line dissipation form hydrodynamic dissipation, which is difficult to achieve experimentally [131]. Finally, the results are summarized and conclusions drawn in Section 3.7.

3.4 Methodology

Superhydrophobic substrates arrayed with micro-pillars (SEM photograph shown in Fig. 3.1a) were fabricated on 4-inch silicon wafers (~ 500 μm thick) using photolithography and reactive-ion etching. Once etched to the desired depth, the substrates were coated with a ~ 100 nm Chromium layer in an electron beam evaporator to promote adhesion of a subsequent ~ 200 nm thick layer fluoropolymer (4, 5-difluoro-2,2-bis(trifluoromethyl)-1,3-dioxole).

Seven different substrate geometries were created with constant solid fraction, $\phi_s \sim 0.11$, but varying pitch and height. Three substrates exhibited an 8 μm pitch, nominal pillar diameters of 3 μm, and 4, 6 and 8 μm pillar heights, respectively. The other four substrates exhibited a 16 μm pitch, nominal pillar diameter of 6 μm, and 8, 12, 16 and 18 μm pillar heights, respectively. These geometrical parameters were chosen such that water would reach the bottom of the cavities during impalement, thus pinning the rebound [132]. Reyssat et al. [?] showed that impalement does not fully penetrate for $h/(w-d)^2 > 10^6$ m^{-1} for a water droplet impinging at a velocity similar those investigated here. For the tallest pillars in both the 8 μm and 16 μm pitch substrates, $h/(w-d)^2 = 0.32 \times 10^6$ m^{-1} and 0.18×10^6 m^{-1}, respectively, thus showing we are well within the complete impalement threshold. This will also be evidenced by the experimental results presented later. From here on, we will refer to the substrates by the following convention: XpYh (e.g. 8p6h refers to the 8 μm pillar pitch, 6 μm pillar height substrate). Pillar height variation across a single substrate (within the region of interest) was on the order of 2%. Final values of pillar diameters, d, and resultant ϕ_s and r are reported in Table 3.1. The apparent static contact angle, θ, for a sessile water droplet in the Cassie state for all substrates was nominally $166 \pm 3^\circ$ with a hysteresis of $\sim 20^\circ$.

Experiments were conducted by releasing a single water droplet from 20 cm above a horizontally-positioned SH substrate as shown in Figure 3.2. One droplet size (~ 24 μL) and impact velocity, V_o (~ 1.96 m/s), were considered across all tests. These were chosen such that the droplet would spread out sufficiently far during impingement and allow a clear view of the impaled

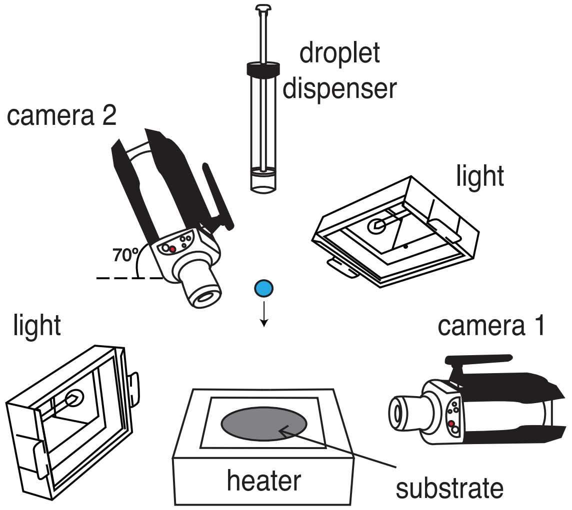

Figure 3.2: Schematic of the experimental setup illustrating the position of the substrate on the heater block and high-speed cameras 1 and 2, which captured droplet impact velocity and dewetting dynamics, respectively.

Table 3.1: Average values of profilometer measurements of pillar-arrayed superhydrophobic substrates. Values for w, h and d are given in μm, while ϕ_s and r are dimensionless.

w/h	d	ϕ_s	r	w/h	d	ϕ_s	r
8/4	3.0	0.11	1.59	16/8	6.0	0.11	1.59
8/6	3.1	0.11	1.88	16/12	6.4	0.13	1.96
8/8	2.8	0.10	2.12	16/16	5.9	0.11	2.18
-	-	-	-	16/18	6.1	0.11	2.32

region. The resulting impact Weber number, $We_o = \rho_o V_o^2 D_o/\sigma_o$, was nominally 190 ($\rho$ is liquid density, D is droplet diameter, σ is liquid-gas surface tension, and the subscript o is used to denote pre-impact conditions at room temperature). D_o was obtained with a high speed camera positioned parallel to the substrate and V_o by fitting a curve to the temporal position of the falling droplet. Uncertainty in V_o and D_o was approximately 1%, while uncertainty in the fluid properties ρ_o and σ_o was 0.2% and 0.7%. Overall uncertainty in We_o was 3.7%.

The superhydrophobic substrate was placed on top of an aluminum block which was heated from the bottom with the sides insulated. Four type K thermocouples (error for absolute measurement $\sim 2.2^\circ$C) were embedded 1 mm below the top of the block at different locations revealing that the temperature variation across that plane of the block was less than 1°C. To determine substrate temperature, a silicon wafer was coated with a thin film of known emissivity (0.96) and placed on top of the aluminum block. Its temperature, as measured with a thermal camera, was nominally 4°C lower than the thermocouples in the range $80°\text{C} < T_s < 100°\text{C}$, where T_s will denote the substrate temperature prior to droplet contact from now on.

To capture dewetting events, a second high speed camera was positioned at an inclination of 70° above the horizontal, as to not interfere with the falling droplet. Figure 3.3A shows a representative impingement event on the 16p18h substrate at room temperature from both camera views. A dark region in the center of the droplet can be observed in the later panels of the top view sequence, which has already been established as impaled liquid on SH substrates of similar scale [**?**,86]. The impaled region is not visible in the first two frames because the drop obscures the view during the initial moments of impingement. Thus, data reported in this work entails dynamics for $t > 2.5$ ms (at room temperature) and $t > 2$ ms (for $T_s > 80°\text{C}$), due to a decrease of viscosity of the droplet and hence slightly faster spreading at higher T_s. After this point and up to ~ 3.5 ms, the lingering curvature of the droplet optically magnifies the area of impalement. This effect endures until the droplet becomes flat in the thin film and is quantified below. An edge finding algorithm based on pixel-value gradient detection was used to measure the impaled area, A, as a function of time (note A is constant in Fig. 3.3a) not including the air bubble at the center, which forms due to air entrapment. The volume of the impaled liquid, Ω, was obtained by $\Omega = A(1-\phi_s)h$. Generally, 10 trials were conducted for each scenario (a given surface at a given temperature). Overall uncertainty, including randomized uncertainty due to scatter, of penetrated volume at any time was obtained based on a 95% confidence level and resulted between 2.7% and 4.3% across all cases.

During the initial stages of impingement, the top of the droplet forms a concave interface (see the first four images of the sequence shown in Fig.3.3), with a radius of curvature, $\mathscr{R}(t)$. Given the difference in index of refraction between water ($n_w = 1.33$) and air ($n_a = 1.00$), the concavity acts like a magnifying lens such that the high speed camera detects a larger impaled region than actually exists. Magnification endures until the interface becomes flat (*i.e.* $\mathscr{R} \rightarrow \infty$). To obtain the temporal magnification, $M(t)$, four small dots (~ 0.1mm) were marked on a superhydrophobic substrate creating a square similar in size to the impaled area at (-i,0), (i,0), (0,j) and (0,-j) around the center of the impingement as shown in Fig. 3.3c. Each of the four points were then tracked

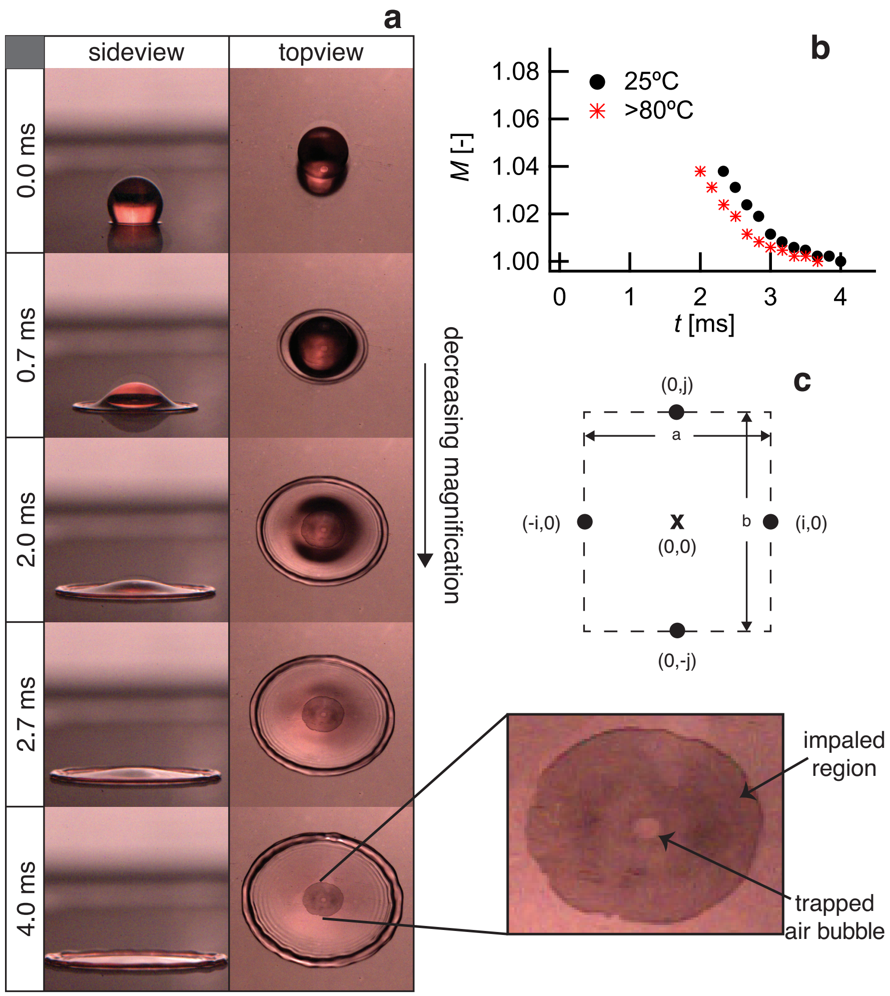

Figure 3.3: a) Droplet spreading following impingement at $We \sim 190$ and ambient temperature ($T_s \sim 25^\circ$C). b) Temporal magnification of impaled area due to droplet curvature at room temperature (•) and on a heated substrate $T > 80^\circ$C (∗). c) Schematic of stencil used to map the extent of magnification during initial droplet impingement.

with the top camera during impingement and the temporal evolution of the area, $A_s = a \times b$, was divided by the unmagnified area to obtain M at each time step. Results are shown in Fig. 3.3b, where $t = 0$ corresponds to the time when the droplet first contacts the substrate. The symbols represent an average of 5 tests. Results show that magnification is modest ($< 5\%$) throughout the spreading event and under 1% after 3.5 ms from impingement.

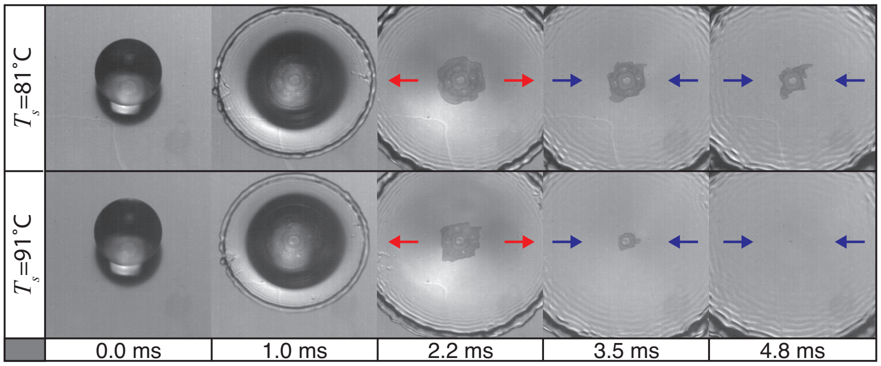

Figure 3.4: Dewetting process during impingement on a 16p18h substrate with $T_s = 81°\text{C}$ and 91°C. In both cases, the impaled region gets smaller with time, but dewetting occurs at a faster rate for $T_s = 91°\text{C}$ such that a complete transition from the Wenzel to the Cassie state has occurred by 4.8 ms. Arrows indicate whether the lamellar ring is moving away or towards the center.

3.5 Experimental Results

Here, we quantify the effects that superhydrophobic architecture and substrate temperature have on the Wenzel to Cassie transition (dewetting) during droplet impingement. Dewetting rates are considered up to the point when the retracting droplet obscures the impaled region prior to rebound (typically ~ 8 ms). Two representative image sequences of dewetting events on the 16p18h substrate at 81°C and 91°C are shown in Fig. 3.4. The data for the 81°C case shows that the impaled region, which can be clearly seen by the third panel ($t = 2.2$ ms), is shrinking with time indicating that dewetting is occurring. However, some liquid remains trapped in the pillars at the end of the event. For the 91°C case, the rate of dewetting is faster and the impaled liquid completely vanishes at $t = 4.8$ ms. We note that dewetting is not necessarily achieved on all substrates or at all temperatures, as will be shown later. The arrows in the last three panels of the top sequence indicate whether the droplet is spreading (arrows point outwards) or retracting (arrow point inwards), thus illustrating that dewetting is not influenced by whether the droplet is spreading or retracting. Finally, the images reveal that although impingement is axisymmetric, the square lattice arrangement of the micro-pillars causes the impaled region to deviate from a circular shape and exhibit sharp corners, in accordance with the work of Reysatt et al. [119].

Results that are shown in Fig. 3.5 characterize the temporal dewetting dynamics for substrate temperatures of $25°\text{C} < T_s < 96°\text{C}$. The temporally varying volume of penetrated or impaled liquid is normalized by a characteristic volume based on the projected area of the droplet and the height of the pillar array for the given substrate, which yields the normalized volume, $\Omega^* = 4\Omega/(\pi D_o^2 h)$. The three panels on the left present data for the 8 μm pitch substrates with pillar heights of 8 μm (top), 6 μm (mid) and 4 μm (bottom), while the three panels on the right represent the 16 μm pitch substrates with pillar heights of 18 μm (top), 12 μm (mid) and 8 μm (bottom). Each curve is the average of 10 trials at the same conditions as explained in Sec. 3.4.

First, dewetting behavior for the 8 μm pitch substrates is discussed. The data of the top left panel (8p8h substrate) shows that at a substrate temperature of 25°C (room temperature) dewetting does not occur (normalized impaled volume is invariant with time). At $T_s = 81°\text{C}$, dewetting occurs with Ω^* decreasing with time and the rate of dewetting increasing with increasing T_s. At $T_s = 91°\text{C}$ and 96°C, the impaled volume transitions completely from the Wenzel to the Cassie state by approximately 5 s and 3 s, respectively. It is also noted that the initial normalized dewetting rate, $d\Omega^*/dt$ (at $t \sim 2$ ms), increases with increasing substrate temperature and this behavior is consistent with all substrates considered.

As pillar height decreases at constant pitch, dewetting becomes less sensitive to temperature. For the 8p6h substrate, dewetting does not occur for any temperatures explored up to $T_s = 81°\text{C}$ and only modest dewetting is evident for the $T_s = 86°\text{C}$ and 91°C cases. At $T_s = 96°\text{C}$, dewetting is pronounced, with only 29% of the initial impaled volume remaining in the impaled state after 8 ms. The nature of the decrease in Ω^* with time is different for this scenario than for the 8p8h substrate. For $T_s \geq 86°\text{C}$, the impaled volume decreases but then levels off and ceases to change (dewetting stops) with time at $t \sim 4$ ms and this behavior is more evident as T_s increases further. The data in the bottom left panel shows that the impaled volume is unchanging with time (no dewetting occurs) for all temperatures explored for the 8p4h substrate, further demonstrating the observation that dewetting rates decrease with decreasing pillar height.

Similar dewetting trends are observed on the 16 μm pitch substrates (right panels of Fig. 3.5). For the 16p18h case, no dewetting occurs at room temperature, but dewetting rates increase significantly for elevated substrate temperatures. Complete dewetting is observed for substrate temperatures of 86°C, 91°C and 96°C at 6.7 ms, 4.8 ms and 3.7 ms, respectively. Similar to the 8p8h surface, $d\Omega^*/dt$ (at $t \sim 2$ ms) increases with increasing temperature. On the 16p12h substrate, the rate of dewetting is not as great as on the 16p18h substrate and only becomes apparent at $T_s = 86°\text{C}$, with the dewetting rate increasing for $T_s = 91°\text{C}$ and 96°C. For these two temperatures,

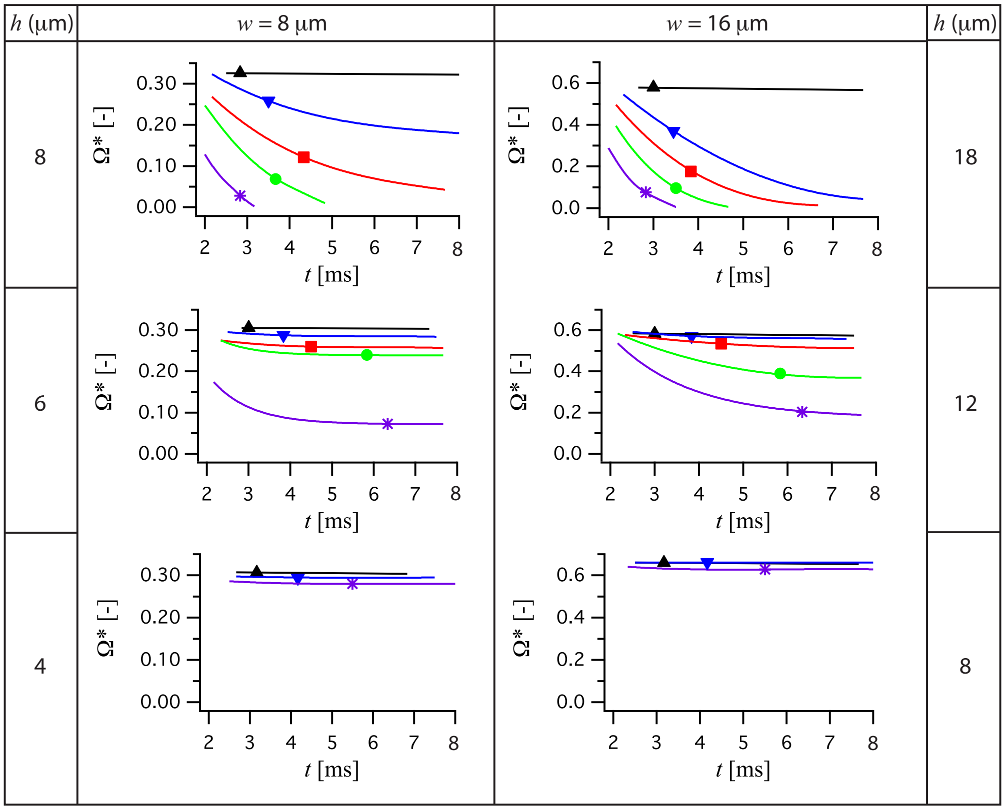

Figure 3.5: Temporal evolution of Ω^* for the 8 μm (left) and 16 μm pitch (right) substrates. On the left, pillar height is 4 μm ($r = 1.59$), 6 μm ($r = 1.88$) and 8 μm ($r = 2.18$) from bottom to top, respectively, while on the right, pillar height is 8 μm ($r = 1.59$), 12 μm ($r = 1.88$) and 18 μm ($r = 2.33$) from bottom to top, respectively. ▲, ▼, ■, ● and ✳ represent $T_s = 25$°C, 81°C, 86°C, 91°C, and 96°C.

the final impaled volumes are 69% and 36% of the initial impaled value for the room temperature scenario. When dewetting occurred for the 16 μm pitch substrates, the impaled volume always decreased with time and no plateauing trends were observed in contrast to the 8p6h substrate. However, dewetting did not occur for the 16p8h substrate at any temperature. Data for the 16p16h substrate are not shown in Fig. 3.5 for clarity, but lie between the data for the $h = 12$ and 18 μm cases.

In summary, dewetting rates increase with increasing h and T_s, although no dewetting occurs for the shortest pillar height (for either pitch) at any T_s, or for the lowest substrate temperature (ambient) at any h. Both the 8 and 16 μm pitch substrates yielded similar behavior at corresponding r values (*i.e.* 8p4h and 16p8h, 8p6h and 16p12h, etc. See Table 1).

All of the image results showed that impalement was initially nearly axisymmetric, but that the symmetry evolved during dewetting into a more "square" shape due to the square lattice arrangement of the micro-pillars. Shown in Fig. 3.6a are images of the dewetting event for the 8p8h substrate at a surface temperature of 91°C and the behavior described below is representative. Due to the entrapped air bubble during impact described previously, there was no impalement in the center of the impaled region (as shown in the images), with the radius of this region denoted as R_b. The total impaled volume was obtained by integrating over the dark region to determine the total impaled area, which is then multiplied by the pillar height. An effective radius of the impaled region can thus be computed as $R_\varepsilon = \sqrt{\Omega/(\pi(1-\phi_s)h)}$ and this will be important for the analysis that is conducted in the following section. A normalized effective radius ($R_\varepsilon^* = R_\varepsilon/(D_o/2)$) was computed as a function of time for all cases considered.

Shown in Fig. 3.6b is R_ε^* as a function of time for the 16p18h substrate at $T_s = 86$°C, with 10 individual trials included. The data reveal excellent repeatability for all trials and shows a linearly decreasing effective radius with increasing time over the majority of the dewetting event. Deviation from linearity occurs only as R_ε approaches the radius of the air bubble trapped in the center, where interaction of this bubble and the effect of individual pillars becomes important. Also shown in the figure is a linear fit to the data from ~ 2 ms to ~ 5 ms. The implication of this is that the dewetting rate $dR_\varepsilon^*/dt \equiv \dot{R}_\varepsilon^*$ is constant over most of the dewetting process. The data for all scenarios exhibited a similar linear relationship, although with a different slope. The behavior of $\dot{R}_\varepsilon^*$ (in the initial dewetting regime where it's constant) is shown in Fig. 3.6c as a function of substrate temperature for all substrates where dewetting occurred. The figure shows that for a given T_s, dewetting rates increase for increasing r values, as expected.

3.6 Analysis

Three independent mechanisms exist that may cause dewetting to occur: buoyancy-driven convection, evaporation and a force resulting from a surface energy gradient between the Wenzel and Cassie states. First, a temperature gradient (decreasing in the vertical direction away from the wall) exists within the impaled liquid and could yield bulk movement of the liquid due to varying density. A buoyancy-induced force would scale as $\rho\beta\Delta T g\Omega$ with ρ, β, ΔT and g representing liquid density, the volumetric thermal expansion coefficient, temperature differential and acceleration

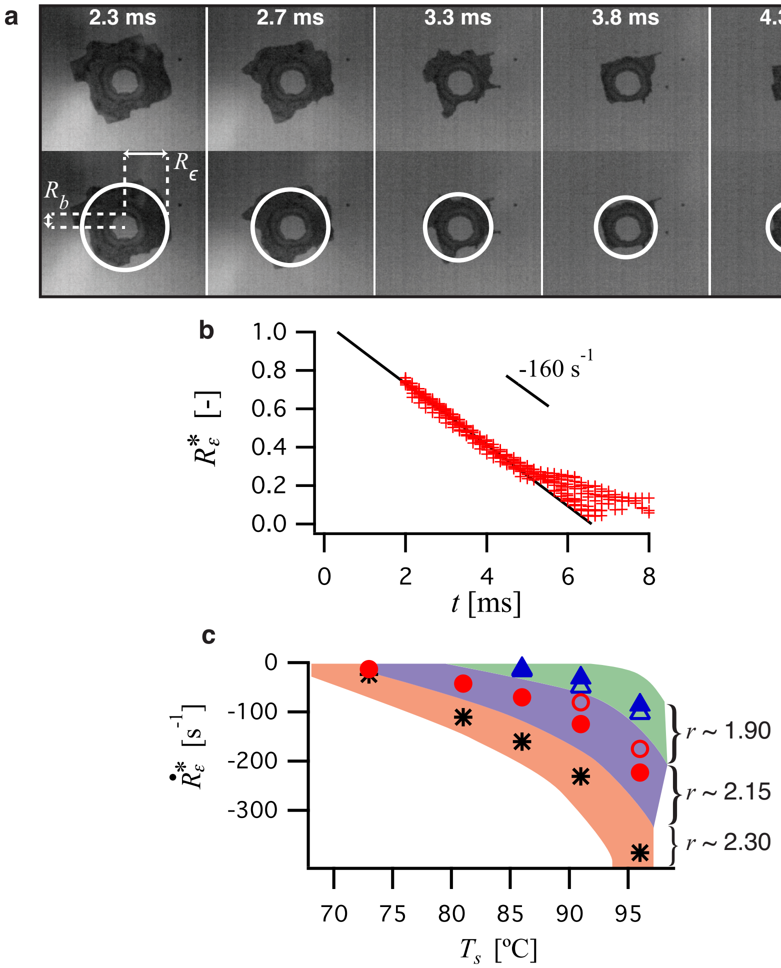

Figure 3.6: a) Image sequence of dewetting event for the 8p8h substrate at 91°C. Overlaid circle of effective radius R_ε used in evaporation and force balance models (bottom sequence). b) Temporal decay of R^*_ε for 10 data sets on the 16p18h substrate at $T_s = 86°\mathrm{C}$. c) $\dot{R}^*_\varepsilon$ as a function of T_s for the 8p6h (▲), 16p12h (△), 8p8h (●), 16p16h (○) and 16p18h (∗) substrates (background color added to emphasize separation due to increasing r values).

due to gravity. However, dewetting due to buoyancy effects is unlikely because of the thinness of the impaled liquid film, h, embedded in the pillar array. Further, although a temperature gradient may induce warmer liquid at the bottom to flow in the direction of decreasing temperature, the rising liquid would be instantaneously replaced by descending colder liquid. Thus, buoyancy will not be considered here. Evaporation of the impaled liquid through the peripheral liquid-air interface is expected to increase with increasing temperature and increasing liquid-gas interfacial area ($\propto h$), both of which agree with trends exhibited by the data. The last mechanism exists because of a surface energy gradient between the Wenzel and Cassie states, which induces an inward pull (in the

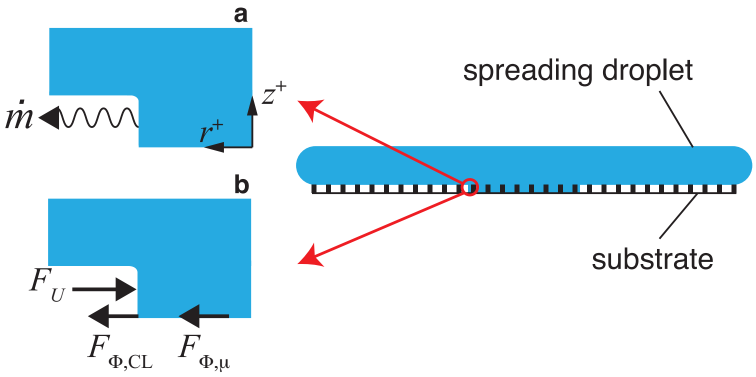

Figure 3.7: Schematic representation of dewetting models for evaporation (a) and a force balance (b). Pillars are not shown on schematics on the left for clarity.

negative radial direction) on the impaled liquid. Figure 3.7 shows schematic illustrations of evaporation and a balance of surface energy and dissipative forces acting on the impaled thin film of liquid. To quantify the extent to which these mechanisms influence dewetting, scaling arguments are considered further below.

3.6.1 Evaporation

Evaporation around the periphery of the impaled liquid at the liquid-gas interface is considered by assuming the impaled volume of liquid is axisymmetric with effective radius, R_ε, and liquid-gas interfacial area, $A_p = 2\pi R_\varepsilon h(1-\phi_p)$, where $\phi_p = d/w$ is the solid fraction around the periphery of the effective impaled disk. The rate of evaporation, $\dot{m}$, in this scenario is governed by

$$\dot{m} = \bar{h} A_p \left(\rho_{s@T_s} - \rho_{s@T_o}\right) \tag{3.1}$$

where $\bar{h}$ is an average mass transfer coefficient and the term in parenthesis represents the difference in density of the saturated vapor at the substrate temperature, T_s, and ambient temperature, T_o, and is the driving potential. To obtain an estimate of the highest evaporation rates possible, forced convection was assumed. Thus, an average mass transfer coefficient, $\bar{h}$, can be estimated via the following empirical relation for forced convection over a flat interface [23]

$$\frac{\bar{h}L}{D_{AB}} = .664 Re_e^{1/2} Sc^{1/3} \tag{3.2}$$

Here, L represents the streamwise length of the flow at the liquid-air interface, D_{AB} is the binary diffusion coefficient of water vapor in air (adjusted for local pressure, $D_{AB} = 4.2 \times 10^{-5}$ m^2/s), $Re_e = \bar{V}L/\nu$ is the Reynolds number and $Sc = \nu/D_{AB}$ is the Schmidt number (ν_{air} is the kinematic viscosity of air and $\bar{V}$ is the velocity of the flow).

Air under the droplet is driven by the spreading motion of the droplet. Because the droplet impacts the substrate with velocity, V_o, we assume $\bar{V} \sim V_o \sim 2$ m/s. The characteristic length in the direction of the air flow, L, is the height of the interfacial area through which evaporation occurs, $L \sim h$. The tallest pillars tested in this work were 18 μm, which yields $Re_e \sim Sc \sim 1$. Finally, a representative R value from experimental observations is 10^{-3} m. Use of these values and Eqs. (3.1) and (3.2) yields an upper bound for the evaporation rate of $\sim 10^{-8}$ kg/s. This value is at least two orders of magnitude smaller than typical measured dewetting rates and as a result we conclude that evaporation is not the dominant mechanism.

3.6.2 Surface Tension/Dissipation Force Balance

A force balance in the radial direction (see Fig. 3.7 for the coordinate system) on a disk of effective radius R_ε can be expressed as $F_U = \Sigma F_{\Phi,i}$ where F_U represents the force due to a surface energy gradient between the Wenzel and Cassie state and $\Sigma F_{\Phi,i}$ includes all dissipative forces. Inertia is neglected because the "system" consists of only the thin disk of impaled liquid and not the entire droplet.

The total surface energy includes interactions between all immiscible interfaces (solid-gas, solid-liquid and liquid-gas) and is obtained by multiplying interfacial areas by their respective surface tensions [107, 116, 117, 133]. When liquid dwells in the Wenzel state, its total surface energy can be expressed as [116, 117]

$$U_w = \gamma_L \pi R_\varepsilon^2 r + \sigma 2\pi R h \phi_p \tag{3.3}$$

where γ_L and σ are liquid-solid and liquid-gas surface tension values. The second term on the right-hand side of (3.3) is very small compared to the first term for the current situation where $h << R_\varepsilon$ and is neglected. Energy in the Cassie state can also be easily defined and simplified via

Young's relation, $\cos\theta^0 = (\gamma_G - \gamma_L)/\sigma$, as [116, 117]

$$U_c = \pi R_\varepsilon^2[\sigma(1-\phi_s) - \sigma\phi_s\cos\theta^0 + \gamma_G r] \tag{3.4}$$

where γ_G is solid-air surface tension.

It is the difference of the foregoing energy states that either promotes or resists dewetting (the system will tend towards the lower energetic state). Thus, it is useful to define an effective surface energy state, U_{eff}, as the difference between the two [116, 134]

$$U_{eff} \equiv U_w - U_c = -\pi R_\varepsilon^2 \sigma \left[\cos\theta^0 (r-\phi_s) + 1 - \phi_s\right] \tag{3.5}$$

where we expect dewetting to occur for $U_{eff} > 0$ and the rate of dewetting to increase with increasing U_{eff}. The presence of the air bubble in the center of the impaled region is easily taken into account by redefining U_{eff} as

$$U_{eff} = -\pi(R_\varepsilon^2 - R_b^2)\sigma \left[\cos\theta^0 (r-\phi_s) + 1 - \phi_s\right] \tag{3.6}$$

where R_b is the radius of the bubble and observations reveal it to be essentially constant. A force stemming from U_{eff} can be obtained by $F_U = -\nabla U_{eff}$ [134, 135] to yield,

$$F_U = 2R_\varepsilon \pi\sigma\xi \tag{3.7}$$

In the above expression, $\xi = [\cos\theta^0(r-\phi_s) + 1 - \phi_s]$. F_U acts in the negative radial direction–thus facilitating dewetting–when $\xi < 0$. Pillar height, h, comes into play in Eq. (3.7) through the roughness factor ($r = 1 + \pi dh/w^2$). Increasing h effectively increases the magnitude of F_U (since $\theta^0 > \pi/2$), and thus provides an explanation for the experimental observations that dewetting rates increase with pillar height due to an increasing driving force. Equation (3.7) further reveals that the dewetting rates observed from the experiments does not depend on pillar height exclusively, but rather on the roughness factor, which explains why substrates with similar r values exhibited similar behavior.

The Young contact angle, θ^0, can have an instantaneous value within the hysteresis range for a given liquid-solid interface. For the present surfaces, the interface is water-Teflon and the measured advancing and receding values show that $113^\circ < \theta^0 < 128^\circ$. Given the nature of the experiments it is impossible to know the instantaneous value of θ^0 as the impaled liquid retreats through the pillar forest. To demonstrate the sensitivity of θ^0 on the driving force, ξ is shown as a function of r in Fig. 3.8 for $\theta^0 = 120^\circ$ and 127°. If ξ is positive, the driving force from Eq. (3.7) is positive and dewetting is not expected to occur, while the converse is true for negative values of ξ. For a given value of θ^0, ξ will be positive at small roughness values (no dewetting) and becomes negative as the roughness increases. At roughness values in the range 1.6 - 1.9, small changes in the instantaneous value of θ^0 can lead to the value of ξ changing from a positive to a negative, or vice-versa. An implication of this is that the dewetting rate for a particular substrate can change with time, and that small changes in θ^0 can result in dewetting stopping. We hypothesize that this is the dynamic at play for the substrates where dewetting was observed initially, followed by a dewetting rate that vanished.

Recall from the data of Fig. 3.5 that dewetting first began at roughness values between $r = 1.59$ (the 8p4h or 16p8h substrate, neither of which ever dewet) and 1.88 (the 8p6h substrate). Dashed vertical lines are depicted in Fig. 3.8 corresponding to these roughness values. For roughness values greater than $r = 1.88$, dewetting always occurred (with the rate dependent on temperature) and for roughness values less than $r = 1.59$, dewetting was never observed. The magnitude of ξ at $\theta^0 = 127^\circ$ changes sign at $r = 1.59$ and at $\theta^0 = 120^\circ$ the change in sign occurs at 1.88. These values of θ^0 lie within the measured hysteresis range and we safely conclude that the instantaneous value of θ^0 during the dewetting process is between 120° and 127°.

The receding impaled liquid results in a moving three-phase (solid-liquid-gas) contact line, hereafter simply referred to as “contact line”, that extends around the periphery of the impaled region. The motion of moving contact lines result in large dissipation rates due to velocity gradients within the liquid domain (hydrodynamical dissipation), friction due to molecular hopping at the contact line (generally referred to as nonhydrodynamical dissipation having been derived from Molecular Kinetic Theory, MKT) and a precursor film. Precursor film dissipation has only been deemed important at moving contact lines of completely wetting liquids [136] and is thus neglected here.

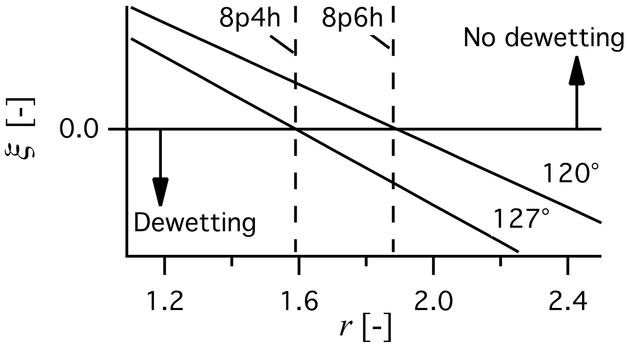

Figure 3.8: Experiments revealed that dewetting ($\xi < 0$) begins somewhere between $1.59 < r < 1.88$ (vertical dashed lines) indicating that the contact angle adopted at the periphery of impalement lies between 120° and 127° (solid lines).

A hydrodynamic dissipation force due to velocity gradients at the bottom surface and adjacent to the vertical pillars scales as $\mu \dot{R}_\varepsilon R_\varepsilon$, where μ is the viscosity of the impaled liquid, R_ε is the effective radius of the impaled (wet) region, and $\dot{R}_\varepsilon$ is the dewetting rate. Equating this dissipation scaling with the driving force due to surface tension gradients given in Eq. (3.7) yields the following scaling

$$\mu \dot{R}_\varepsilon \sim \sigma \xi \tag{3.8}$$

Because the driving and dissipative forces are linearly dependent on R_ε, the scaling suggests $\dot{R}_\varepsilon$ is constant for a given scenario. Common models for liquid viscosity are of the form $\mu \sim 10^{B/(T-C)}$ where T is the absolute temperature of the impaled liquid and B and C are empirically-derived constants of best fit for the distribution of dynamic viscosity with temperature [137]. Substituting this temperature dependency for viscosity into (3.8) and rearranging suggests that all data should collapse in the following manner

$$\frac{\dot{R}_\varepsilon}{\xi} \sim 10^{-B/(T-C)} \tag{3.9}$$

where σ has been assumed to be constant and is dropped from the scaling. Shown in the top panel of Fig. 3.9 is a comparison of the scaling of Eq. (3.9) with the experimental data, where $\dot{R}_\varepsilon/\xi$ is plotted as a function of the surface temperature, where ξ was determined at a constant value of $\theta^0 = 123.5°$. For the scaling, coefficients for the viscosity of water obtained from literature are utilized, with $B = 247.8$ K and $C = 140$ K [137] and T being set to the measured substrate temperature for each scenario. The experimental data for all scenarios considered (shown in symbols) collapse to a similar power-law curve. The scaling of Eq. (3.9) is also shown in the figure and although the model also suggests a power relationship (governed by the dependence of viscosity in temperature), it does not capture the trend followed by the experimental data, which exhibits a much stronger dependence on temperature. This mismatch between the scaling and the data indicates that hydrodynamic dissipation is not the dominant mode of dissipation during dewetting.

We now consider dissipation caused by the moving contact line. Derivation of dissipation at the contact line due to molecular hopping is extensive and stems from Eyring's MKT model [138]. Blake et al. adapted this MKT model and developed an expression for a moving contact line dissipative force [139], which is used here. When the contact angle at the moving contact line is similar to the static contact angle, which is the case here, the dissipative force can be expressed as [140–142]

$$F_{\Phi,\mathrm{CL}} = 2\pi R_\varepsilon \dot{R}_\varepsilon \frac{\hbar}{\lambda^3} e^{\Delta G_w / N k_B T} \tag{3.10}$$

where λ is the individual molecular displacement, k_B is the Boltzmann constant, ΔG_w is the activation free energy of wetting, N is Avogadro's number and $\hbar$ is Planck's constant. The downside of this theoretical manifestation is the difficulty of comparing it with experiments. Because λ and ΔG_w are usually not known *a priori*, they are obtained by curve fitting empirical data of a specific liquid-solid-gas interaction. Tabulated values vary widely and available data only exists for very specific scenarios at specific temperatures (normally room temperature) [139–143]. Furthermore, care must be taken when interpreting and utilizing such empirical results due to the sensitivity of these constants: λ is raised to the third power and ΔG_w dwells inside an exponential. For simplicity and to form a scaling argument, λ is discarded from Eq. (3.10), thus giving the following scaling

$$F_{\Phi,\mathrm{CL}} \sim R_\varepsilon \dot{R}_\varepsilon e^{\Delta G_w / N k_B T} \tag{3.11}$$

The driving force, F_U, is now balanced with the triple line dissipative force to yield

$$\dot{R}_\varepsilon \sim \xi \Phi \tag{3.12}$$

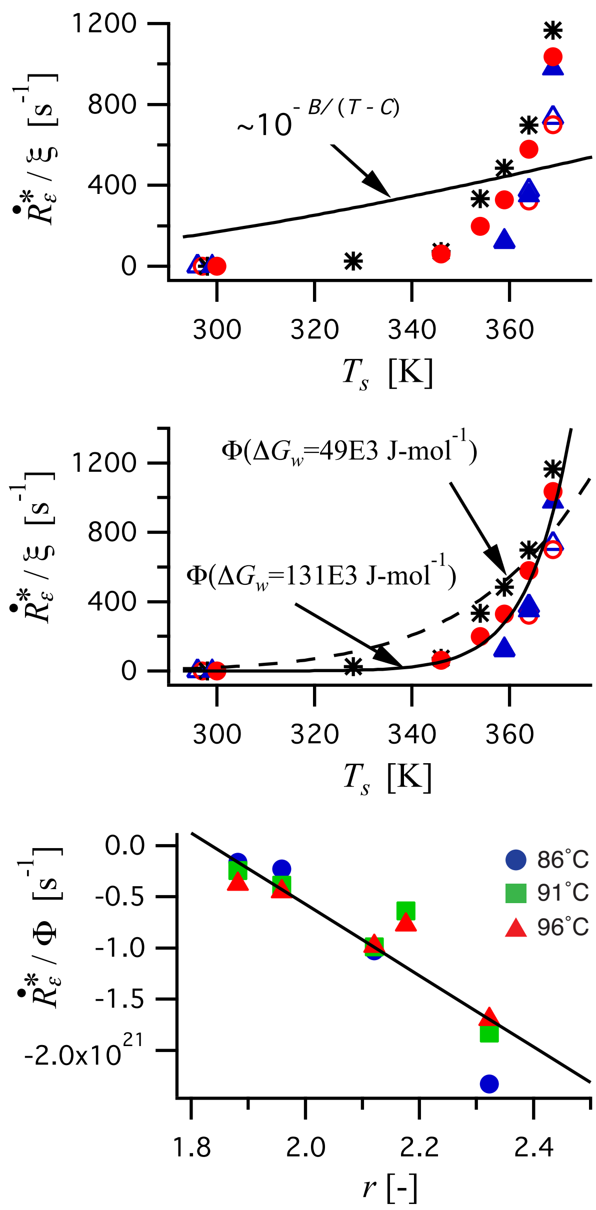

Figure 3.9: Top and middle panel: $\dot{R}^*_\varepsilon/\xi$ as a function of T_s for all scenarios considered where dewetting occurred with $\xi(\theta^0 = 123.5^\circ)$. Symbols represent the experimental data and follow the same convention used in Fig. 3.6c. In the top panel, the solid curve represents the scaling of Eq. (3.9), while in the middle panel, the solid and dashed curves represent the scaling of Eq. (3.12) for two different ΔG_w values as depicted. Bottom panel: $\dot{R}^*_\varepsilon/\Phi$ with $\Delta G_w = 131 \times 10^3$ J mol^{-1} as a function of r.

with $\Phi = e^{-\Delta G_w / N k_B T}$. This relation also indicates that dewetting speed is constant for a given scenario (*i.e.* no dependance on R_ε), which agrees with the experimental behavior already discussed (Fig. 3.6b). Furthermore, the scaling of Eq. (3.12) also suggests that the experimental data should collapse as a function of temperature with $\dot{R}_\varepsilon / \xi$.

The middle panel of Fig. 3.9 again shows the experimental results for $\dot{R}_\varepsilon^* / \xi$ as a function of T_s. The experimental data collapses and agrees with the scaling argument in Eq. (3.12) with $\Delta G_w = 131 \times 10^3$ J mol^{-1}. This value of ΔG_w was obtained by performing a least squared fit to the experimental data. A value for ΔG_w is not available from the literature for a water-Teflon-air interface at the specific temperatures explored, however, the value obtained here is within a factor of three to a published value for a glycerol/water mixture (70% aqueous) on Mylar polyester tape (also a hydrophobic interaction), where $\Delta G_w = 49 \times 10^3$ J mol^{-1} [139]. The scaling of Eq. (3.12) with this value of ΔG_w is also shown in the middle panel of Fig. 3.9 for comparative purposes, where the dependence on temperature is not as great as demonstrated by the experimental data. Finally, $\dot{R}_\varepsilon^*$ normalized by the exponential of Eq. (3.12) is shown as a function of r in the bottom panel of Fig. 3.9. The experimental data collapses into an approximately linear decay as a function of r, as suggested by Eq. (3.12), where $\xi \propto r$.

The models developed in this section arise from a force balance between the driving force generated by the surface tension gradient that exists between the Wenzel and Cassie state and a dissipation force. The results suggest that hydrodynamic dissipation exerts only a small influence, while the contact line dissipation plays the predominant role in the dissipation and resistance to dewetting. The scale analysis (contact line dissipation) agrees very well with the experimental observations that increasing pillar height and increasing substrate temperature increase dewetting rates. These two occur for different reasons, the former because of an increase in the driving force, while the latter because of a decrease in dissipation.

3.7 Conclusion

In this paper the transient process where a localized Wenzel state incurred during droplet impingement recedes or “dewets” back to the Cassie state has been explored. Unlike other mechanisms previously considered for transition from the Wenzel to Cassie state, which aggressively affect the flow, such as boiling or vibrations, the one discussed here achieves dewetting passively.

Experiments reveal that dewetting rates are strongly dependent on the substrate temperature and micro-pillar height. The influence that both of these parameters exert on the process were quantified over a temperature range of 25°C to 96°C, pillar height range from 4 μm to 18 μm, and for two pitch values, 8 μ and 16 μm. Two dewetting mechanisms were considered to explain the dewetting behavior, with one based on evaporation and the other based on a force balance. Evaporation was found to exert negligible influence. The force balance equated the driving force, based on a gradient between the Wenzel and Cassie energy states with dissipation. Hydrodynamic and non-hydrodynamic (based on molecular hopping at the triple contact line) dissipations were considered (with forces that act in opposition to the dewetting motion). A scaling argument revealed that hydrodynamic dissipation plays a minor role and that nonhydrodynamic dissipation exerts dominant influence. The overall results can be summarized as follows:

- The rate at which dewetting occurs increases with increasing substrate temperature and pillar height.
- Both the experiments and scaling suggest that geometrical parameters (such as pillar height or pitch) are not individually important, but a combination in the form of the roughness factor governs the dynamics.
- A force resulting from an energy gradient between the Wenzel and Cassie states drives dewetting, while contact line resistance inhibits the flow.
- The scaling provides a physical explanation for the experimental observations: Increasing h induces dewetting due to an increased driving force, while increasing T_s also induces dewetting but due to decreased dissipation.

These findings have broader implications in the design and commercialization of superhydrophobic surfaces for varying applications, especially those focused on single droplet or multi-droplet mobility. Further research should include micro-features of differing geometry (square posts, ribs, etc.) and different liquid-solid hydrophobic interactions.

CHAPTER 4. HYDRODYNAMICS OF DROPLET IMPINGEMENT ON HOT SURFACES OF VARYING WETTABILITY

This chapter has been submitted for publication in the International Journal of Heat and Mass Transfer. The formatting of this paper has been modified to meet the stylistic requirements of this dissertation.

4.1 Contributing Authors and Affiliations

Cristian E. Clavijo, Julie Crockett, Daniel Maynes Department of Mechanical Engineering, Brigham Young University, Provo, Utah 84602

4.2 Abstract

This work presents on the hydrodynamics of water droplet impingement on superheated solid surfaces across the entire wettability spectrum: superhydrophilic, hydrophilic, hydrophobic and superhydrophobic. While a large body of work exists on droplet impingement on hydrophilic and superhydrophilic surfaces, impingement on the latter two has been largely neglected and the present results show that dynamics are dramatically different. Experiments ranging in surface temperature from 125°C to 415°C and Weber numbers from 10 to 225 were performed and analyzed using high-speed imaging. Some of the most striking differences are as follows. While atomization is always present for impingement on the hydrophilic and superhydrophilic surfaces at temperatures below the Leidenfrost point, atomization is absent at low Weber numbers and at low excess surface temperatures on the hydrophobic surface. At high surface temperatures, the attraction of vapor bubbles on the hydrophobic surface allows a vapor blanket to form more readily thus leading to Leidenfrost behavior at a much lower temperature than classically observed on a hydrophilic surface. One of the most interesting phenomenon that will be discussed includes what will be described as a "pseudo-Leidenfrost" state for impingement on the superhydrophobic

surface. Because water can be suspended at the peaks of the roughness on a superhydrophobic interface, vapor escapes from underneath the droplet thus mimicking Leidenfrost behavior for all excess temperatures. This results in minimal atomization for superhydrophobic impingement over the entire regime explored. Finally, maximum spread diameters for Leidenfrost impingement are tabulated as a function of the Weber number for all surfaces and are shown to be larger on the smooth surfaces than on the textured ones indicating that droplet spreading at the Leidenfrost point is *not* independent of surface type as previously supposed.

4.3 Introduction

Significant interest in the interaction between droplets and superheated solid surfaces is evident by the plethora of publications in the last few years [8, 46, 53, 144–150]. This scenario is present in a wide array of applications including spray cooling, coating, biochemical reactions and combustion. The physics involved are rich and complex including both hydrodynamic and thermal transport phenomena. From a hydrodynamical stand point, a droplet impinging a hot surface can have dramatically varying results. It may boil violently, atomize and splash, or rebound without either splashing or atomizing (or a combination of the two). Instantaneous heat transfer rates correspondingly vary dramatically across these regimes. While ample research has been performed in this field, most of it has focused on interactions with hydrophilic-type surfaces. Thus, open questions for impingement boiling on hydrophobic and superhydrophobic surfaces still remain. This work addresses some of these questions.

In 1997, Bernardin et al. published some of the first comprehensive boiling regime maps for droplet impingement on heated aluminum (hydrophilic) surfaces for impact Weber numbers, $We = \rho V^2 D/\sigma$, (where ρ, σ, V and D represent liquid density and surface tension, impact velocity and initial diameter, respectively) of 20, 60 and 220 [24]. They observed that at low excess surface temperatures (contact boiling regime), boiling increased with increasing surface temperature, where boiling was described as the presence of vapor bubbles, droplet breakup and the ejection of a fine mist or shower of tiny droplets. This shower of droplets is generally referred to as atomization or secondary atomization; we will refer to it as atomization throughout this paper. On the other hand, they found that for sufficiently high surface temperatures, atomization was no longer present and the droplet would rebound as if on a superhydrophobic surface. [24]. This regime is known as film boiling and the lowest surface temperature at which atomization ceases to occur has been named the Leidenfrost point (LFP) [9,30,44,151,152]. The lack of atomization is attributed to the presence of a thin vapor film at the solid-liquid interface by which vapor can be transported from the droplet, thus preventing vapor bubbles from bursting [8,9,11,24].

With improved high-speed imaging technology and controlled micro-fabrication techniques, Tran et al. later provided another detailed study of droplets impinging on heated smooth [9] and textured [11] hydrophilic surfaces. They also constructed regime maps, but this time with surface temperatures as high as 600°C. An entirely new regime applicable to droplets was introduced, namely ”spraying film boiling”, which occurs at surface temperatures well above the LFP. Here, atomization once again is present and is also attributed to bursting vapor bubbles [9]. However, the primary mode of heat transfer is radiation through the thin vapor film which still exists between the droplet and the hot surface. Their results further showed that the transition temperature from contact to film boiling increases with Weber number and that surface texture decreases the LFP, both of which are a result of a balance between vapor production (surface temperature) and inertia of the impacting droplet (Weber number). Lastly, they concluded based on observations made using an optically-transparent sapphire plate as the impinged surface, that the liquid does not contact the solid for impingement during film boiling [9]. These results provide further evidence that at the LFP, transport through the vapor film prevails and inhibits bubble formation and atomization.

The maximum spread diameter, D_{max}, at the LFP provides insight to the dynamics of the system as well and has been explored in multiple previous works [48,53,153–155]). Tran et al. showed that D_{max} is larger at the LFP on a hydrophilic surface than on a superhydrophobic surface maintained at room temperature for $We < 1000$, though both exhibit similar spreading/retracting dynamics [9]. These trends have also been confirmed elsewhere [10]. Larger maximum spread diameters during Leidenfrost impingement are attributed to droplets being hotter (less viscous) and not interacting with the solid (less frictional resistance). These results seem to indicate that droplet spreading/retracting dynamics in the film boiling regime may be independent of the wettability of the surface since the droplet is suspended above its own vapor with negligible contact with the solid [11]. However, the results of the present work will show that D_{max} at the LFP is different for surfaces of varying wettability suggesting that lack of atomization does not always imply a stable vapor film.

More recently, the morphology of an impinging droplet on hot aluminum surfaces over a wide range of surface temperatures and Weber numbers was presented by Bertola [8]. A regime map was developed based on atomization and whether a droplet remained intact following impact. The regime maps that shall be disclosed herein only denote regions where atomization was or was not observed but are not indicative of droplet breakup regions (breakup is discussed to a smaller extent). The work by Bertola also highlighted that maximum spread diameters are unattainable for *We* greater than 100 at the LFP due to peripheral droplet separation, though this value is lower than that reported by Tran et al. [9, 11] ($We \approx 200$).

Though previous research has covered a broad range of experimental conditions and provided great insight into the physics of the interaction between a droplet and a heated hydrophilic surface, impingement on hydrophobic and superhydrophobic surfaces at elevated temperatures has received only modest attention [52, 53]. All work available, to the authors' knowledge, on droplet impingement on heated hydrophobic/superhydrophobic surfaces is now described. Park et al. performed experiments of droplets (360 μm in diameter) impinging on hydrophilic and hydrophobic surfaces over a temperature range of 110°C to 210°C [52]. However, because the study was mainly focused on thermal transport considerations between solid and droplet, little information on boiling hydrodynamics was provided. They reported that the residence time was generally lower for impingement on a hydrophobic substrate, but no information regarding Leidenfrost transition temperatures or maximum spread diameter at the LFP was given. In a different work, Li et al. report hydrodynamic behavior of impinging droplets, such as droplet height, diameter and dynamic contact angles, on surfaces of varying wettability (hydrophilic to superhydrophobic) but the maximum surface temperature explored was limited to 110°C [53]. More recently, a publication has described boiling dynamics of a water droplet on heated hydrophobic and superhydrophobic surfaces ($<$ 230°C) in which they reported minimized boiling behavior on superhydrophobic surfaces, but only a sessile droplet was considered [54]. Thus, hydrodynamics of droplet impingement on hydrophobic and superhydrophobic surfaces at temperatures well above saturation remains largely unexplored.

This paper presents on the phenomena of a millimetric water droplet impinging on heated surfaces of varying wettability (superhydrophilic to superhydrophobic) over a surface temperature range of 125°C to 415°C. Given that a broad body of work on hydrophilic/superhydrophilic impingement already exists, the main contribution of this work is attributed to dynamics on hydrophobic and superhydrophobic surfaces. Notwithstanding, experiments were also conducted on hydrophilic and superhydrophilic surfaces for comparison with other works in the literature. Section 4.4 provides a detailed methodology of the experimental approach. In Section 4.5, high-speed images are provided which qualitatively show the difference in atomization and vapor bubble formation across the different types of surfaces for varying *We* and surface temperatures. Atomization regime maps are constructed for each surface, which clearly identify the LFP as a function of the Weber number. Maximum spread diameters at the LFP as a function of time and impact Weber number are also provided. Finally, conclusions are given in Section 4.6.

4.4 Experimental procedure

Four surface types were fabricated on 500 μm thick / 100 mm diameter polished silicon wafers: superhydrophilic (SHL), hydrophilic (HL), hydrophobic (HB) and superhydrophobic (SHB). For the HL surface, an unaltered polished silicon wafer was used. For the HB surface, a thin coat of Teflon was applied to a wafer in the following manner to render it hydrophobic. Teflon (4, 5-difluoro-2,2-bis(trifluoromethyl)-1,3-dioxole) was dissolved in FC-40 to yield a 0.2% Teflon solution, which was subsequently applied to the wafer by spin coating (a $\sim$ 100 nm chromium layer was applied first for adhesion promotion). The wafer was then placed on a hot plate at 90°C for 5 minutes, 165°C for 5 minutes and 330°C for 20 minutes. The resultant Teflon coat was $\sim$ 200 nm thick. Teflon was chosen as the coating material due to its stronger thermal stability than other hydrophobic coats such as organosilanes. For the SHL and SHB surfaces, wafers were first arrayed with a square lattice arrangement of micro-pillars via photolithography and etching (6 μm diameter, 8 μm height and 16 μm center-to-center spacing). Teflon was applied in a similar manner to the description above to yield the SHB surface, while the SHL surface was left uncoated. Roughness is known to increase hydrophilicity/phobicity on a given surface per the Wenzel and Cassie-Baxter equations, respectively: $\cos\theta = r\cos\theta_e$ and $\cos\theta = r\phi\cos\theta_e + \phi - 1$, where θ, r, θ_e and ϕ respectively represent the apparent contact angle, the overall surface area divided by its projected area (roughness), intrinsic contact angle, and the area of the top of the pillars divided by the projected area of the surface (solid fraction). For the SHB and SHL surfaces, $r \approx 1.6$ and $\phi \approx 0.11$. SEM images and sessile water droplets on all four surfaces are shown in Figure 4.1. The

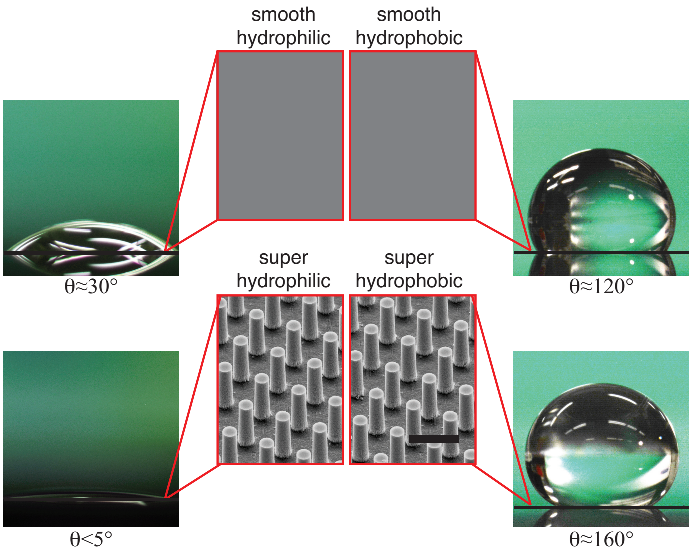

Figure 4.1: A 5 μL water droplet resting on the four different surfaces used in this work: (top) hydrophilic and hydrophobic; (bottom) superhydrophilic and superhydrophobic.

static contact angles on all four surfaces at room temperature were 0° (SHL), 30° (HL), 120° (HB) and 160° (SHB) (droplet remained in the Cassie state on the SHB surface), with a ±3° uncertainty.

For heating, an aluminum block was embedded with four 500 W cartridge heaters and four thermocouples (5 mm below the surface) upon which the wafers were placed. The surface temperature of the wafer, T_s, (the value reported in this work as "surface temperature before impact") was deduced by placing a silicon wafer coated with a thin coat of known emissivity (0.96) and measuring its temperature with a thermal camera. Thermal camera values were usually 2°C - 10°C lower than thermocouple readings depending on the temperature of the block. Figure 4.2 shows the relation between the thermal camera measurements and thermocouple measurements (symbols) and a linear fit up to 350°C, a limit imposed by the coat of known emissivity. For block temperatures above this point, the surface temperature of the wafer was deduced by extrapolation. The range of surface temperatures tested in this work was 125°C - 415°C for the HL and SHL surfaces, and 125°C - 340°C on the HB and SHB surfaces. The temperature range on the hydrophobic surfaces was limited by the glass transition temperature of Teflon. Water contact angle tests were performed on the HB and SHB surfaces regularly after experiments to verify that no Teflon degradation had occurred.

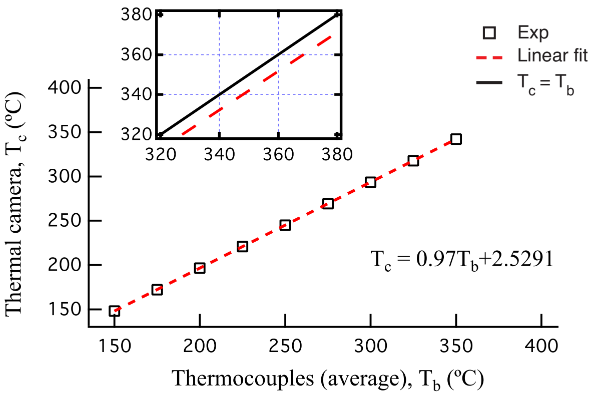

Figure 4.2: Calibration plot between temperature measured by thermocouples and thermal camera.

Impingement events were captured in the following manner. A distilled water droplet (5 μL, $D = 2.2$ mm) was released from a syringe (needle gauge 30) some height above the heated wall such that the impact Weber number was varied by varying the release height. All events were captured with a high-speed camera at 3000 - 6000 fps with a spatial resolution of 12 μm/pixel. Regime maps were constructed based on whether atomization was observed. Atomization was defined as a mist of very small droplets that are ejected during spreading and did not include satellite droplet separation at the periphery of the drop. The LFP was defined as the lowest surface temperature at which atomization was no longer observed. Whether atomization was present in a given scenario was determined by visual inspection of the high-speed videos. While the presence of atomization was generally easy to detect, determining its presence near transitional boundaries (onset of film boiling) was not straightforward in some cases. The reason for this is that atomization decays as surface temperature nears the LFP such that its intensity slowly decreases making the definite temperature at which it completely stops difficult to establish. Furthermore, it has been said that atomization dynamics near the LFP are probabilistic [8]. This is why the transition from the atomization to atomization-free regimes is generally given with a temperature resolution of 10°C to 40°C [8, 9, 11]. For the present work, the resolution is 25°C.

Impact parameters such as droplet velocity and initial and maximum spreading diameters were extracted via a computer vision algorithm. Impact droplet diameter was obtained by $D = \sqrt{4A/\pi}$, where A was the area captured by the camera and the impact velocity was calculated by fitting a straight line through the center of gravity of the descending droplet during the last 15

- 20 frames prior to impact. Liquid properties such as density and surface tension were always evaluated at room temperature. Uncertainty in the droplet diameter and the impact Weber number is about 1% and 3%, respectively. Each scenario was repeated between 5 - 12 times and the total uncertainty was based on a T-test 95% confidence interval.

4.5 Results & Discussion

Results are organized as follows. In Section 4.5.1, high-speed images of droplet impingement on all four surface types are shown for different Weber numbers and surface temperatures. Hypotheses are postulated based on the observations and discussed qualitatively. In Section 4.5.2, atomization regime maps are presented. LFP values are compared with other work available in the literature and differences across varying surface types are addressed. In Section 4.5.3, maximum spread diameters as a function of *We* for all surfaces at their respective LFP are presented. We note that this study is only concerned with the initial rebound of a droplet (typically within 12 ms of impact) and not subsequent ones.

4.5.1 High Speed Imaging of Atomization

Basic differences between the SHL/HL and the SHB/HB surfaces at low T_s and low We will be discussed first. This scenario is depicted through the high-speed image sequence in Fig. 4.3, where the rows (from top to bottom) represent impingement on SHL, HL, HB and SHB surfaces, respectively, at $T_s = 150°\text{C}$ and $We = 40$. The times for all frames are given in the figure, where maximum spread diameter on the HB surface occurs at $\approx$ 3 ms. The photographs show that atomization does not begin on any of the surfaces by 3 ms. At 9 ms, the droplets on the SHL and HL surfaces have completely spread out over the surface and exhibit atomization, while the droplets on the HB and SHB surfaces are rebounding with no atomization having taken place. Atomization on the SHL surface is more abundant than on the HL surface because of the increase in surface area due to the texturing, having also been reasoned elsewhere [11]. The spread-and-stick behavior on the HL and SHL surfaces, as well as the repelling behavior on the HB and SHB ones, is similar to impingement at room temperature given the low excess temperature here. Because the liquid remains attached on the former two surfaces, it will eventually completely vaporize for large

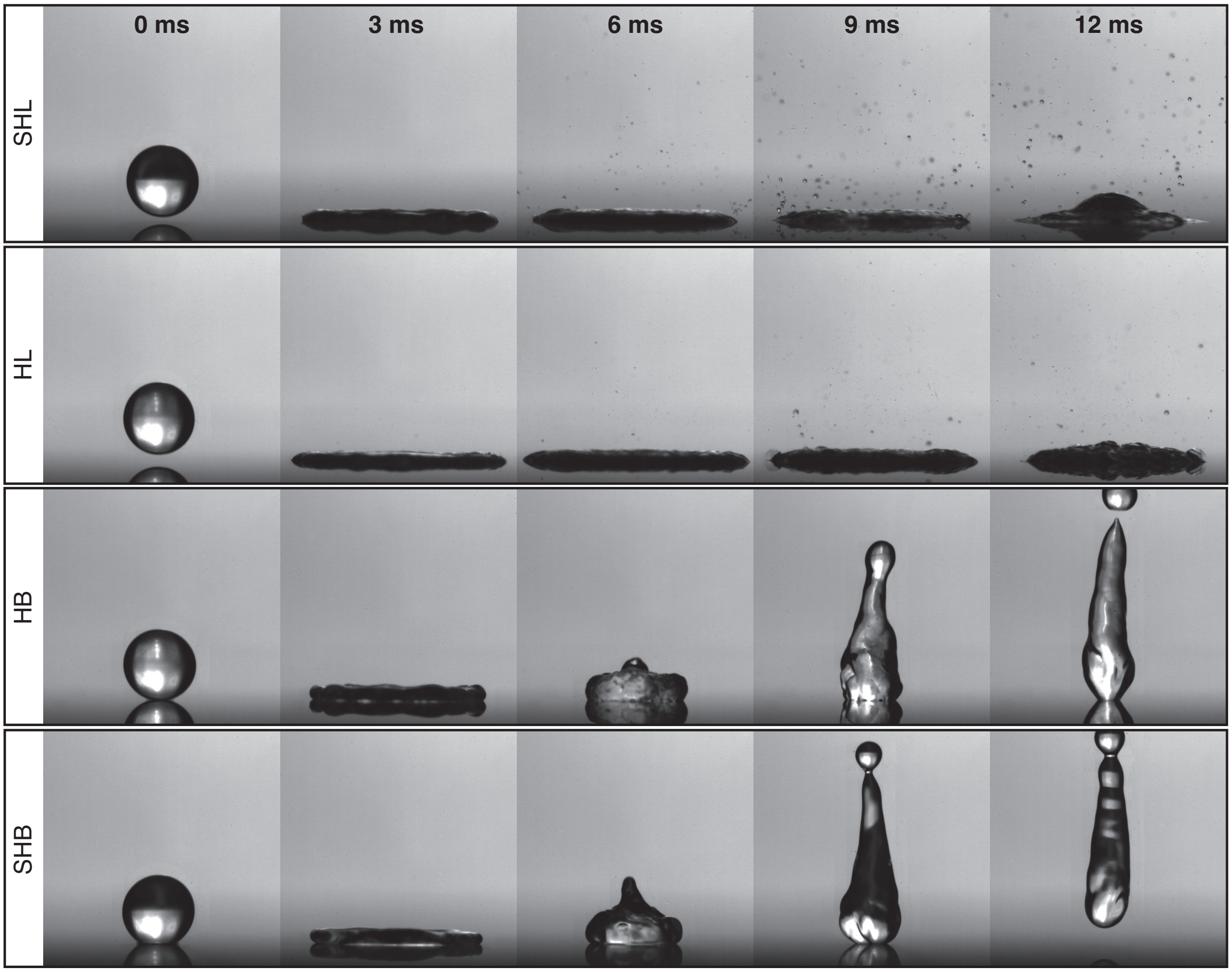

Figure 4.3: Image sequences of droplet impingement on all four surfaces at $T_s = 150°\mathrm{C}$ and $We = 40$. Atomization exists on the SHL and HL surfaces and is absent on the HB and SHB surfaces.

enough times (~ 1 s). On the other hand, the lack of atomization on the HB and SHB surfaces may be attributed to the smaller maximum spread diameter (smaller contact area) and less time spent in contact with the surface, both of which result in less heat transfer. As stated earlier, the presence of atomization implies the presence of bursting vapor bubbles, which leads one to conclude that vapor bubbles exist on both the HL and SHL surfaces for this scenario, while their existence on the other surfaces remains as of yet undetermined. Furthermore, if bubbles exist on the HB and SHB surfaces, why do they not burst?

To investigate further, impingement was filmed from a top view at the same surface temperature and Weber number. The photographs are shown in Fig. 4.4 and depict dynamics which occur before the rebounding jet begins to form on the HB and SHB surfaces (≈ 4.3 ms). As seen from this view, it is evident that the spread diameter is generally larger on the HL and SHL surfaces as already discussed. Furthermore, the presence of vapor bubbles is verified here on these surfaces, which is not surprising given an excess temperature of roughly 50°C. Interestingly, these photographs also show the presence of bubbles on the HB and SHB surfaces. The presence of vapor bubbles but lack of atomization (at least any that could be captured by the same camera arrangement that captured atomization on the other surfaces) then suggests that no bubble bursting occurs. One possible explanation is that the lamellar film on the HL and SHL surfaces must be thin enough as to allow "venting of the vapor bubbles" through atomization [9]. The larger spread diameters support the idea of a thinner lamella film via a conservation of volume inspection, admittedly qualitatively. This establishes an important technicality often used–or misused–loosely in the field. The contact boiling and atomization regime for droplet impingement should not be used interchangeably since they are not one and the same. Here, the former precedes the latter (in terms of temperature), but does not necessarily coincide.

Next, we continue to explore dynamics on all surfaces at low *We* but higher surface temperatures. The top panel of Fig. 4.5 shows impingement dynamics at $T = 275°\text{C}$ and $We = 25$. Atomization is evident on the HL and SHL surfaces as expected at this temperature. Similar to the results of Fig. 4.3, no atomization occurs on either the HB or SHB surface even though surface temperature is much higher. First, dynamics on the HB surface will be discussed. The lack of atomization here is unexpected since spreading on the HB surface exhibits diameters of similar lengths to the HL surfaces (which was not the case at $We = 40$) and thus similar thin film thickness and boiling behavior should prevail. Experiments were performed at the same *We* for lower temperatures to test whether the film boiling regime had been reached. These experiments, for which images are not shown, resulted in atomization over the range $200°\text{C} < T_s < 270°\text{C}$ indicating that the LFP on the HB surface occurs at $T_s \approx 275°\text{C}$. This result is intriguing because transition to film boiling at this *We* does not occur on the HL and SHL surfaces until $T_s \approx 365°\text{C}$ and 320°C, respectively. What causes the LFP to occur on a hydrophobic surface at lower temperatures? It has been shown previously that vapor bubbles on smooth hydrophobic substrates tend to grow in a flat manner and spread out over the solid (analogous to a water droplet on a hydrophilic surface), which is in contrast to bubble growth on a hydrophilic surface where bubbles bead up (analogous to a water droplet on a hydrophobic surface) [49, 50, 156]. Thus, bubble growth structure on the

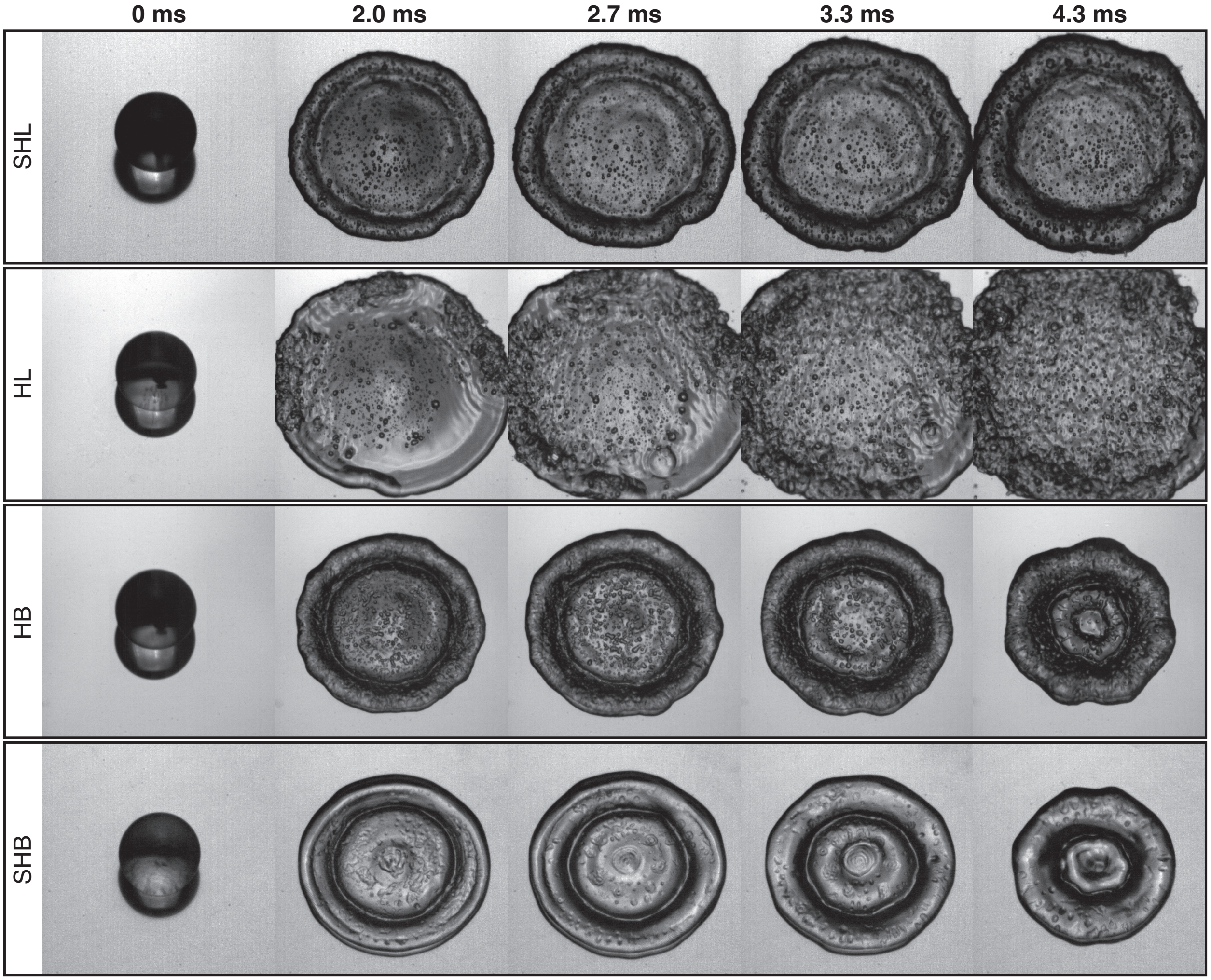

Figure 4.4: Top view of droplet spreading at $T_s = 150°\text{C}$ and $We = 40$ on all four surfaces. These images show the existence of vapor bubbles that form during impingement at the solid-liquid interface on the HB and SHB surfaces, as well as the HL and SHL surfaces.

hydrophobic surface facilitates the formation of a vapor blanket, which leads to transition to film boiling at lower temperatures. A schematic drawing of the expected bubble growth is shown in Fig. 4.6. Early transition to film boiling has also been observed for hydrophobic pool boiling [51] and immersed hydrophobic solid spheres [157].

To evaluate LFP dependence on Weber number, the experiments were repeated at the same surface temperature ($T_s = 275°\text{C}$) as the top panel of Fig. 4.5 but at a higher We ($We = 100$). This is shown in the bottom panel of Fig. 4.5. The images depict that atomization occurs on the HL and SHL surfaces, as it did for the lower Weber number case, though both exhibit more violent atomization, as well as peripheral droplet break up associated with the increased kinetic energy at

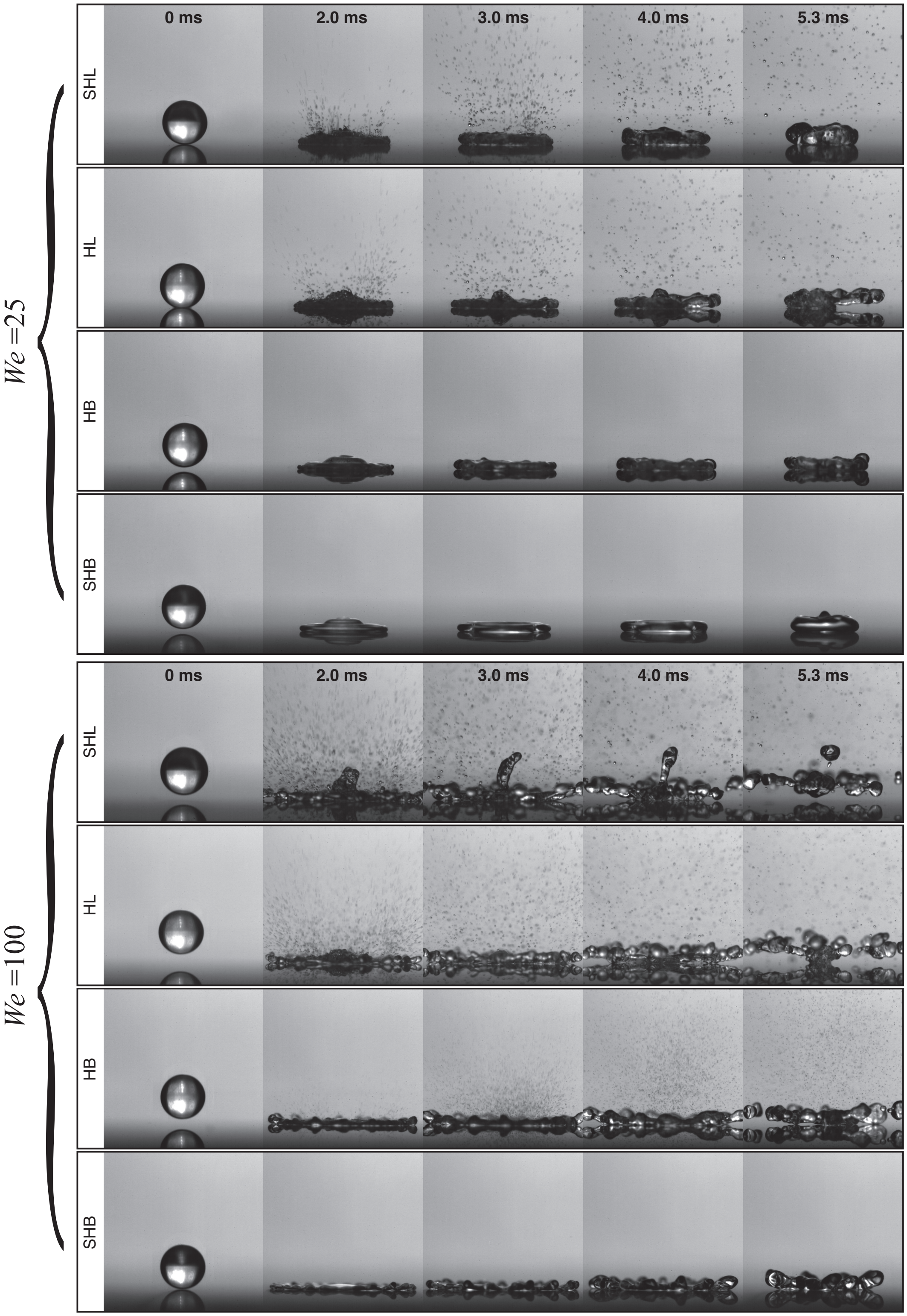

Figure 4.5: Droplet impingement on all four surfaces at $T_s = 275^\circ\text{C}$ and $We = 25$ (top) and 100 (bottom).

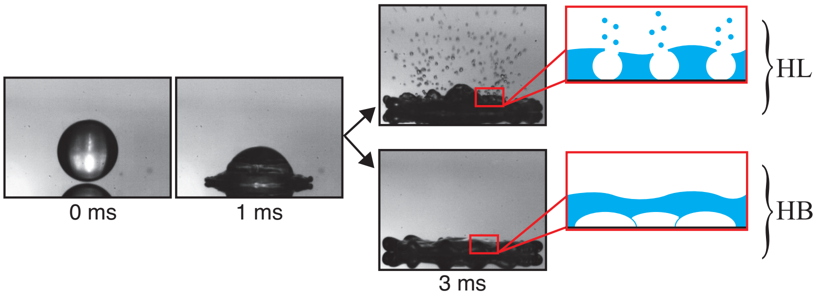

Figure 4.6: Schematic drawings of bubble dynamics inside the droplet during spreading on the HL and HB surfaces for $T_s = 275°C$ and $We = 25$.

impact. Furthermore, the rebound on the SHL surface is characterized by the formation of a vertical jet, which has only been observed on textured hydrophilic surfaces and may be associated with "converging liquid motion toward the axis of the flattened drop" [11]. Interestingly, the droplet on the HB surface does atomize at this *We* indicating that the LFP at this Weber number must occur at a higher temperature. This result suggests that LFP increases with Weber number on the HB surface, a trend that is consistent with hydrophilic surfaces [8, 9, 11]. This trend occurs as a result of larger inertial impacts requiring higher vapor production at the interface to maintain a stable vapor film layer.

Remarkably, Fig. 4.5 shows that atomization is absent on the SHB surface at $T_s = 275°C$ for both *We*. As will be shown in the following section, atomization does not occur on the SHB surface at this surface temperature for any of the *We* explored. To investigate behavior on the SHB surface further, experiments were conducted at other surface temperatures and various Weber numbers. We found that atomization was generally minimal and only present for a few specific scenarios. As an example, two impingement events on the SHB surface are shown in Fig. 4.7, which are representative of scenarios with the largest amount of atomization observed on the SHB surface over the entire regime explored. The top row represents SHB impingement at $We = 50$ and $T_s = 175°C$ while the second and third row correspond to $We = 100$ and $T_s = 220°C$ for the SHB and HL surfaces, respectively. Impingement on the HL surface is shown for visual comparison. As is evident in these images, the amount of atomization that occurs on the superhydrophobic surface is almost indistinguishable, in accordance with a previous study of sessile droplets on heated superhydrophobic surfaces of similar solid fractions [54].

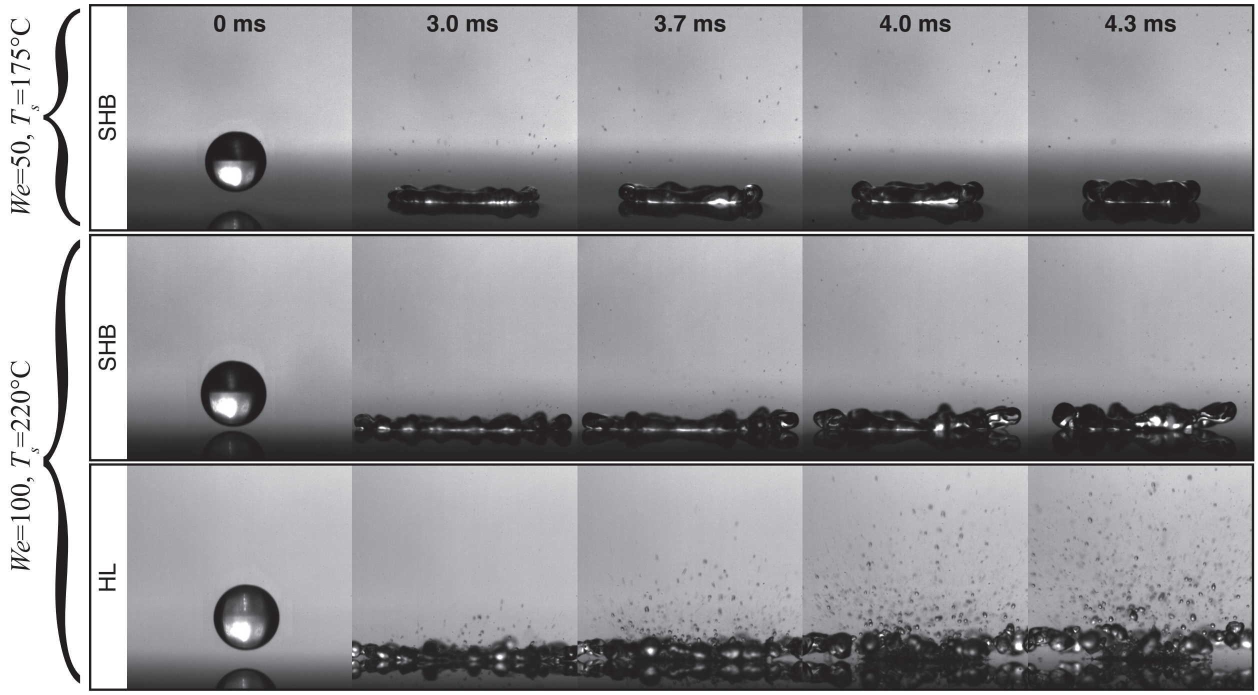

Figure 4.7: droplet impingement on the SHB surface at $T_s = 175$°C and $We = 50$ (top panel) and 220°C and $We = 100$ (middle panel). Both of these scenarios represent cases where the most atomization was observed on the SHB surface. Dynamics on the HL surface are shown in the bottom panel for comparison at the second set of conditions.

Minimized atomization during contact boiling is attributed to the hydrophobic texture (micro-pillars) and rationalized as follows. First, the pillars do not permit liquid intrusion into the open space between them (even if liquid penetrates at the impingement point due to stagnation pressure, it is likely that the liquid returns to the Cassie state due to the elevated temperature of the surface [158]). The prevailing Cassie state results in a reduction of contact area between solid and liquid (solid fraction is 11% for the current case) and thus heat transfer to the liquid is decreased. Second and more importantly, the cavities in between the micro-pillars allow vapor to continuously escape from underneath the droplet, thereby mitigating vapor bubble formation and atomization. This is drastically different from behavior on other surface types during contact boiling where vapor must vent through the droplet itself, causing atomization.

To further investigate this idea, impingement events were recorded from a top view on all four surfaces in the contact boiling regime as shown in Fig. 4.8 at $We = 50$ and $T_s = 200$°C.

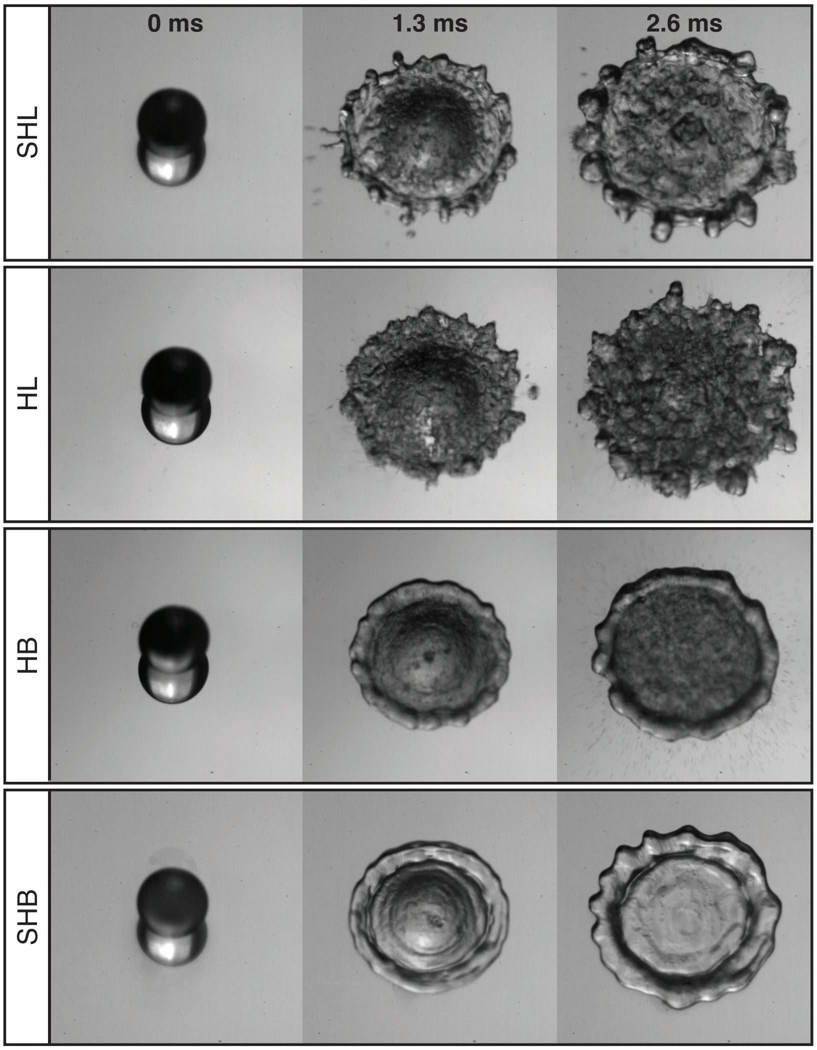

Figure 4.8: Top view of the impingement event for $We = 50$ and $T_s = 200$°C on all four surfaces to demonstrate minimal boiling behavior on SHB surface made evident by the transparency of the spreading droplet.

These photographs depict boiling activity on the SHL, HL and HB surfaces, which can be easily recognized by the opaque nature of the droplet. In contrast, the droplet on the SHB surface does not display boiling and remains transparent suggesting that vapor transport from underneath suppresses bubble activity. Thus, droplet impingement on the superheated SHB surface is tantamount to what occurs on the other surfaces (SHL, HL and HB) in the film boiling regime, namely, vapor is able to freely escape from underneath the droplet through the vapor film. This alternate flow path for vapor flux minimizes vapor bubbles forming within the droplet on these surfaces, thus suppressing atomization. The open space in the hydrophobic pillar forest allows vapor to escape in a similar manner even when contact prevails. One may thus analogously refer to droplet impingement on the SHB surface in the contact boiling regime as a pseudo-Leidenfrost effect. As discussed earlier, no atomization was observed on the SHB surface at $T_s = 275°\mathrm{C}$ at any *We* indicating that a stable film boiling regime exists for the SHB surface and this will be discussed in the next section.

But if vapor is free to escape through the superhydrophobic interface during contact boiling, why does atomization on the SHB surface occur at all? We hypothesize that if vapor production at the solid-liquid interface is higher than the rate at which vapor can escape through the textured interface, vapor will build up in the liquid with a force proportional to the rate of vapor generation [46] forming "domes" (see Fig. 4.4). These domes, which can burst in a similar way to bubbles formed on a different surface type, are the cause of the minimally observed atomization but only induces atomization when the droplet becomes sufficiently thin during spreading/retraction (*i.e.* for high enough Weber numbers; discussed in next section). Future work should explore different types of superhydrophobic surfaces to quantify the relationship between resistance to vapor flow through the texture and the corresponding magnitude of atomization.

4.5.2 Atomization Regime Maps

Atomization regime maps were constructed for all surfaces over the range of $10 < We < 225$ and $150°\mathrm{C} < T_s < 415°\mathrm{C}$ as shown in Fig. 4.9. Circular symbols (accompanied by shaded regions) represent scenarios where atomization did occur, while triangular ones represent scenarios where atomization did not, where transitional boundaries fall in between. Each scenario was repeated 5 to 12 times with more repetitions near the boundaries. We begin by describing behavior on the HL and SHL surfaces and note that atomization always occurred for all temperatures between 125°C and the LFP regardless of the *We*. Transition to film boiling on these surfaces increases with *We*, which agrees with what has been previously reported [8,9,11]. This is due to an increase in inertial pressure at impact associated with increasing *We*, which requires a higher surface temperature to maintain the vapor blanket at the interface, as stated earlier.

Tran et al. showed that atomization resumes on smooth hydrophilic surfaces at surface temperatures approaching 500°C, and called this regime "spraying film boiling" [9]. In the cases considered here, atomization was never observed above the LFP on any of the surfaces, indicating that the spraying film boiling regime was likely not reached in the present experiments. Results

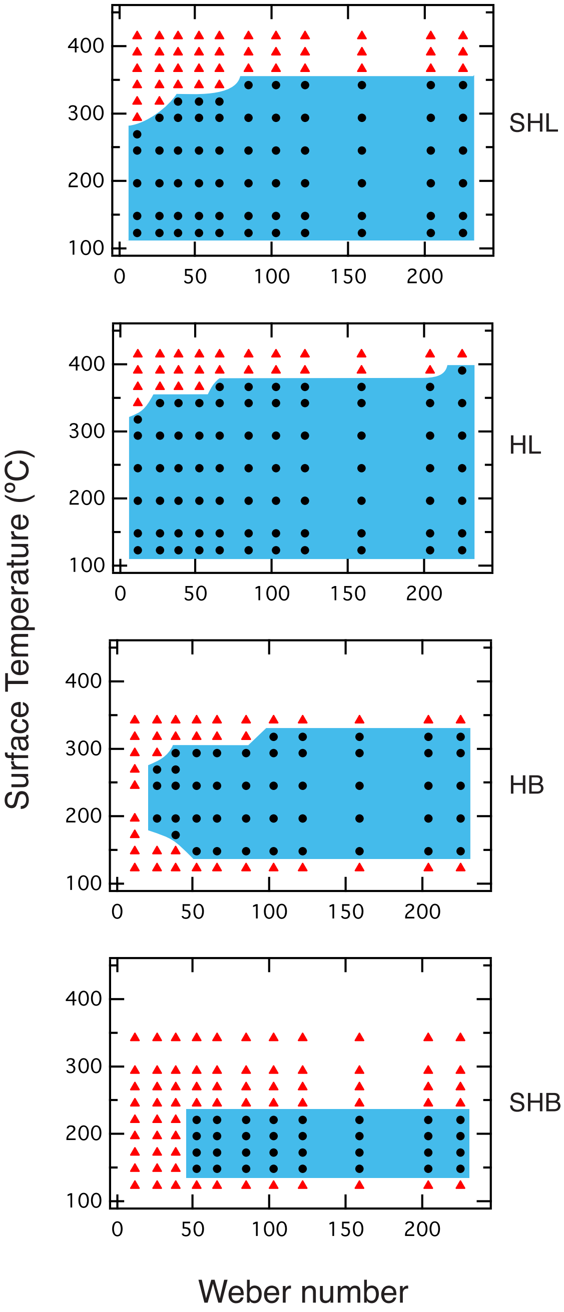

Figure 4.9: Atomization regime map for all four surfaces. Circles represent scenarios where atomization occurred, while triangles represent scenarios where atomization was not observed.

also show that the LFP is lower for the SHL surface than for the HL surface, for all We. This occurs because surface texturing effectively increases the solid surface area, which increases heat transfer to the droplet, promoting the formation of a stable vapor layer at lower surface temperature [11].

Next, we discuss the atomization regime map for the HB surface (third panel in Fig. 4.9). The map is similar in form to the HL and SHL maps, but shows two exceptions. First, no atomization occurs at $We \approx 10$ for any T_s, or at $T_s \approx 125°\text{C}$ for any We. Lack of atomization at $We \approx 10$ is attributed to minimal spreading on the hydrophobic surface at relatively low We, which results in a thicker spreading drop. Thus, while vapor bubbles still form at the solid-liquid interface, they never penetrate the free surface of the droplet. Lack of atomization at $T_s \approx 125°\text{C}$ is due to the relatively low heat transfer rate into the droplet. Here, the short time the droplet spends flat on the surface is much less than the time it takes for atomization to begin on the hydrophilic surface (~ 50 ms). The second difference regarding impingement on the HB surface is the lower surface temperature associated with transition to film boiling relative to both the HL and SHL surfaces for all We explored. A hypothesis for this early transitional behavior was formulated and described in conjuction with Fig. 4.5, and is related to the attraction of vapor bubbles to the surface.

Atomization behavior differs dramatically on the SHB surface. First, the map (bottom panel of Fig. 4.9) depicts a significantly smaller atomization or contact boiling regime. Furthermore, the intensity of the atomization in this regime is significantly less than that on other surfaces as noted previously (see Fig. 4.7). This was attributed to the ability of vapor to escape through the cavities in the pillar forest, which, being similar to vapor transport on other surface types at the LFP, was named the pseudo-Leidenfrost state. This map shows that a transition exists ($T_s \approx 245°\text{C}$) from this pseudo-Leidenfrost state to a more stable Leidenfrost state, where no atomization was observed. This transition indicates that increasing surface temperature (thus increasing vapor production) stimulates vapor dome growth enough to form a more continuous vapor layer above the texture yielding a larger path for vapor to escape.

Figure 4.10 shows the LFP (based on the regime maps in Fig. 4.9) as a function of We. The top panel includes LFP values for the SHL and HL surfaces, as well as data from Tran et al. [9,11] and Bertola [8]. The bottom panel shows the LFP for all surfaces in this work. Error bars are based on the resolution of temperature ranges at which experiments were performed, 25°C. Data from Tran et al. represent LFP values for droplet impingement on heated smooth hydrophilic [+] and

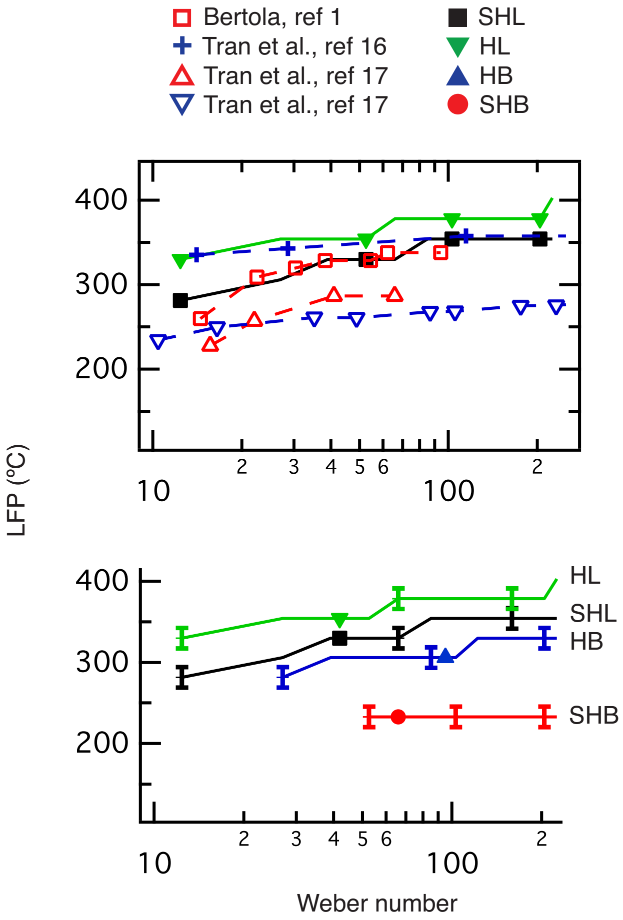

Figure 4.10: Transition temperature to the Leidenfrost point or LFP as a function of *We*. Top panel: Present results shown with data from Bertola [8] and Tran et al [9]. Bottom panel: Present results for all four surfaces.

two types of textured hydrophilic silicon wafers similar to the ones used in this work. The pillar diameter on their textured hydrophilic surfaces was 9 μm and the pillar height was 8 μm, while the pitch values were 29 μm [△] and 13 μm [▽]. Surface temperature values reported by Tran et al. in their publication [9, 11] were based on thermocouple readings embedded in the stainless steel holder upon which the wafers were placed rather than actual wafer surface temperatures. These values were later corrected by Bertola [8] to represent actual surface temperature and the corrected values are the ones shown here. The second set of data are from Bertola [□] and represent experiments performed on a heated aluminum surface with average surface roughness of 0.1 μm. All trends in the top panel of Fig. 4.10 show that the LFP increases with *We*. LFP values on the hydrophilic surface show very good agreement with results of Tran et al. for $We < 50$, but exhibit an offset of about 20°C at higher Weber numbers, which falls within the resolution of the experiments. Superhydrophilic LFP values reported in this work differ from those of Tran et al. by 50°C and 75°C at low and high Weber numbers, respectively. This is rather unexpected since their texture also consisted of micro-pillars, but differences might be related to pillar diameter where those used by Tran et al. were 50% larger than the ones used here. This would further explain their lower LFP values which are a consequence of higher heat transfer rates. Results from Bertola match more closely our data for the SHL surfaces. This may be due to roughness on the aluminum surface, which approximates the superhydrophilic scenario, although some discrepancy is expected due to the different material used. Data in the bottom panel of Fig. 4.10 shows that the LFP on the SHL surface is nominally 12% less than that on the HL surface over the entire *We* range explored, while the LFP on the HB and SHB surfaces are respectively 20% and 40% smaller than for the HL surface. Moreover, the SHB surface exhibited no dependence of the LFP on the Weber number over the entire *We* range explored. Given the probabilistic nature of the transitional boundaries aforementioned, it is difficult to determine this dependence definitively.

4.5.3 Maximum Spread Diameters

In this section, we discuss the relationship between the normalized maximum spread diameter (D_{max}/D) at the LFP and the Weber number as shown in Fig. 4.11. Weber numbers of 100 and greater generally resulted in satellite droplet ejection (matching the work of Bertola [8]) thus limiting the *We* range that was explored. Maximum spread diameters on a superhydrophobic surface at room temperature are typically provided for comparison when discussing Leidenfrost droplet rebound since both undergo a repelling interaction [159, 160]. We do likewise here and thus the top panel depicts our results for impingement on the SHB surface at room temperature alongside with results for the HL and SHL surfaces at their respective LFP values (where the LFP at a given *We* was defined in Sec. 4.5.2). Also shown are experimental data from Antonini et al. (superhydrophobic surface at room temperature) [10] and Tran et al. (hydrophilic and superhydrophilic surfaces at their respective LFP values) [11] for comparison.

Our data compares well with the two data sets from the literature in Fig. 4.11. All data sets show that D_{max}/D increases with increasing *We* for all scenarios, as expected. However, the maximum diameter is lower on the superhydrophobic surface at room temperature than at the

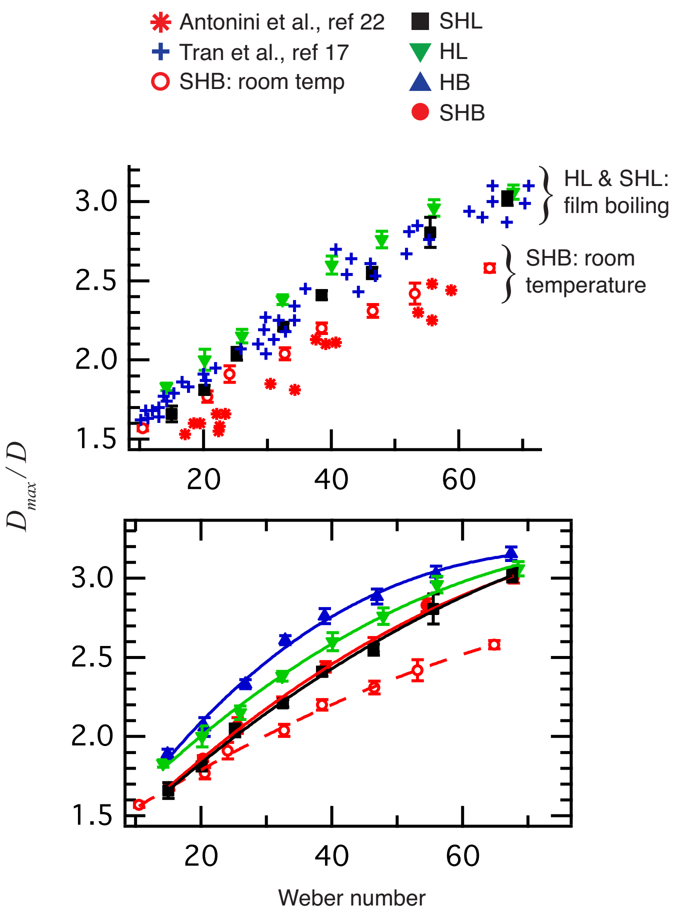

Figure 4.11: Normalized maximum spread diameter as a function of *We* at the corresponding LFP values for each surface and SHB at room temperature. Top panel: Present results shown with data from Antonini et al. [10] and Tran et al. [11]. Bottom panel: Present results for all four surfaces with a curve fit for clarity.

LFP for the hydrophilic and superhydrophilic surfaces. This should not be surprising given two facts. First, even though the vapor blanket "insulates" the droplet from the heated surface on a Leidenfrost impingement, the temperature of the bottom of the droplet is still close to saturation temperature since it is continuously vaporizing. Because the bottom of the droplet houses the largest velocity gradients [161], the reduction of liquid viscosity (due to increased temperature) is significant and allows for larger spreading. Second, Leidenfrost spreading encounters virtually no solid-liquid contact and thus approaches an infinite slip scenario [32], which is in contrast with spreading on the SHB surface at room temperature, which experiences no shear over cavities but frictional resistance over the pillars.

Having shown agreement between our data and that of previous researchers, focus is now turned to results for all surfaces considered in this work. The bottom panel of Fig. 4.11 constitutes our results shown in the top panel with the addition of the HB and SHB surface results at their respective LFP values. A curve fit to each data set is shown for clarity. Since no transition to Leidenfrost behavior on the SHB surface occurred for $We < 50$ (atomization was absent at all temperatures), impingement was evaluated at a constant surface temperature of 230°C, the LFP value at higher We. The data here shows that the maximum spread diameter is larger on the HB and SHB surface at their respective LFPs for all We than for the SHB surface at room temperature, as was the case with the HL and SHL surfaces. More interestingly, the figure shows that D_{max}/D is lower for both textured surfaces (SHL and SHB), which virtually overlap each other, than for the smooth surfaces (HL and HB) for all We. This difference is greater than the uncertainty of the experiments, which is low given that length calibration uncertainty does not play a role due to the manner of normalization. For example, at $We \approx 33$, $D_{max}/D = 2.61$ on the HB surface, but only 2.22 on the SHB and SHL surfaces, yielding an 18% increase, while uncertainty was about 2% on either surface. The differences in maximum spread diameter across all the surfaces suggest that Leidenfrost rebound is not independent of surface type. In other words, it is unlikely that a full vapor film exists at the interface, which would create independence of spreading dynamics from the solid surface characteristics. At first glance, it seems reasonable to assume that the considerable differences in LFP temperatures across the different surfaces may cause the measured discrepancies through differences in viscosity. However, we see that D_{max}/D on the SHL and SHB surfaces collapse to nearly the same curve even though the LFP on the former is generally 100°C greater than on the latter. This suggests that surface architecture plays a dominant role over surface temperature.

It is likely that very little, if any, solid-liquid contact prevails during impingement on the HB surface since it exhibited the highest maximum spread diameters. As mentioned earlier, vapor bubbles spread out on a hydrophobic solid lending themselves to a continuous vapor film sooner. On the other hand, more friction must be present during spreading on the other surfaces since the maximum spread diameters on those are smaller. First, let us compare results between the HB and the textured surfaces (SHB and SHL). It is likely that some contact between the top of the pillars (either SHB or SHL) and the liquid prevails during spreading at the LFP since vapor can dwell and vent through the micro-pillar forest [46]. This contact exerts frictional resistance on the flow yielding smaller maximum spread diameters than on the HB surface, though it is difficult to ascertain to what extent contact is present. Solid-liquid contact and atomization are not mutually exclusive as discussed earlier so long as vapor can escape through the cavities at the interface.

Differences in maximum spread diameters between the HB and HL surface are now discussed. While this difference is not as large as that of the HB and textured surfaces, it is a measurable difference nonetheless. This is interesting because both surfaces are smooth and there is no texture which might exert frictional resistance on the flow during spreading. Once again, we highlight that viscosity changes due to surface temperature are unlikely since the LFP values associated with the HB surface are lower even though it is the surface that exhibited larger spreading. Thus, we hypothesize that the differences in maximum spread diameters are related to the way in which bubbles form and bead up on the hydrophilic surface. This idea is concomitant with protruding menisci which increase friction, rather than providing a favorable slip condition, at the solid-liquid interface [162]. On the other hand, bubbles do not bead up on the HB surface, but rather spread out in a flat manner consequently enhancing slip.

Earlier in the paper, we discussed that contact boiling and atomization regimes are not one and the same. Given the differences in maximum spread diameter discussed here, another important distinction is now brought to light: film boiling and atomization-free regimes are not the same. Discrepancy in terminology may have in part existed because droplet impingement is often categorized with similar regimes used in pool boiling. For example, if atomization is present, the impingement event may be said to be in the contact or "nucleate" boiling regime, whereas if atomization is absent, it is assumed to be in film boiling. The results in this section indicate that the lack of atomization and a stable vapor film may not always coincide since surface-type plays a role in spreading dynamics even when atomization has disappeared.

4.6 Conclusion

In this paper, the hydrodynamics of a single droplet impinging on a superheated solid surface were analyzed. Previous research has focused on smooth and textured hydrophilic surfaces and, as such, experiments here were performed on a smooth hydrophobic and a micro-pillar textured superhydrophobic surface. A smooth hydrophilic and a micro-pillar textured superhydrophilic surface were also used for comparison, as well as data available in the literature. The ranges of surface temperatures and Weber numbers considered were 150°C to 415°C and 10 to 225, respectively. High-speed images were acquired and presented to qualitatively discuss the associated impingement dynamics across the different surface types. Results were quantified into regime maps which depict where atomization is present. Finally, the maximum spread diameter at the LFP prior to peripheral droplet breakup for each surface was quantified and compared across all surfaces as a function of the Weber number. Results can be summarized as follows for impingement on the hydrophobic surface explored here:

- Atomization is absent at low Weber numbers ($We \approx 10$) for all surface temperatures and at low surface temperatures ($T_s \approx 125°\mathrm{C}$) for all Weber numbers. The former occurs because the droplet does not spread as far as it does on a hydrophilic surface prior to retraction resulting in a thicker spreading film, while the latter because the droplet spends less time in contact with the surface. Both of these behaviors prevent vapor bubbles from bursting.
- Transition to the Leidenfrost regime occurs at lower surface temperatures than on the hydrophilic or superhydrophilic surfaces for all Weber numbers explored. Given the attraction of vapor bubbles to the hydrophobic surface, a vapor blanket at the solid-liquid interface is more readily formed.
- At the Leidenfrost point, the droplet spreads out farther prior to retraction compared to all other surfaces at their respective LFP. This behavior is not attributed to lower viscosity since the LFP values of some of the other surfaces are higher.

For impingement on the superhydrophobic surface:

- Atomization is significantly less intense than on all other surface types and occurs for a much narrower range of parameters. The hydrophobic micro-pillars at the interface cause water to be suspended above them and thus vapor escapes from underneath the droplet, which promotes Leidenfrost-like behavior at all conditions.
- Transition to the Leidenfrost regime occurs at a much lower surface temperature than all other surface types.

- Maximum spread diameter at the LFP is lower than both the hydrophobic and hydrophilic surfaces for all *We*. This indicates that some solid-liquid contact may prevail during spreading, thus exerting frictional resistance on the flow.

CHAPTER 5. SECONDARY ATOMIZATION DURING DROPLET IMPINGEMENT ON SUPERHEATED HYDROPHOBIC AND SUPERHYDROPHOBIC SURFACES

This chapter will be submitted for publication to the International Journal of Heat and Mass Transfer. The formatting of this paper has been modified to meet the stylistic requirements of this dissertation.

5.1 Contributing Authors and Affiliations

Cristian E. Clavijo, Kimberly Stevens, Julie Crockett, Daniel Maynes Department of Mechanical Engineering, Brigham Young University, Provo, Utah 84602

5.2 Abstract

This paper presents on secondary atomization dynamics during droplet impingement on superheated hydrophobic and superhydrophobic surfaces (one smooth hydrophobic and three different superhydrophobic surfaces). The superhydrophobic surfaces used are made up of circular pillars 4 μm in height with varying center-to-center distance (pitch): 8 μm, 12 μm and 16 μm. The range of surface temperatures explored is 110°C $< T_s <$ 337°C. An image processing algorithm was developed to quantify the temporal behavior of secondary atomization captured via high-speed photography across the different surfaces and different surface temperatures. The results show that secondary atomization is initially absent following impact ($<$ 1 ms) on all surfaces, after which point it begins, and its intensity is a function of surface temperature and surface type. The maximum amount of atomization for a given scenario is highly dependent on surface temperature. For low surface temperatures, atomization increases with temperature, but then begins to decrease at high surface temperatures. This rise and fall behavior is tantamount to the classical relationship between heat flux and excess temperature for the case of pool boiling. Both scenarios depend on vapor bubble formation dynamics at the interface and the stability of the so-called Leidenfrost

vapor film for which surface wettability has an impact. Surface pitch also plays a significant role in secondary atomization dynamics with its intensity being significantly higher for smaller pitch surfaces. The implications of these results suggest that not all superhydrophobic surfaces sustain Leidenfrost-like behavior at all excess temperatures.

5.3 Introduction

This paper is concerned with droplet impingement on hydrophobic and superhydrophobic solid surfaces heated above the saturation temperature of the liquid. Boiling is present in a myriad of industrial applications. Understanding its complexities is crucial for further advancements in quenching, electronic and power plant thermal management and other applications where high heat transfer rates are necessary [163–165]. Research on the interaction of sessile or impinging droplets on hot surfaces is of particular interest because it mimics situations such as spray cooling and condensation processes. The study of a single (rather than multiple) droplet impinging on a surface further facilitates the analysis of secondary atomization, which is defined as the ejection of small droplets during droplet impingement due to bursting vapor bubbles [8, 43, 166]. Understanding secondary atomization is crucial in order "to achieve a better control of spray cooling," [167] amongst other applications. Most research on droplet impingement on hot surfaces has focused on hydrophilic surfaces such as aluminum, steel, copper, etc. However, as superhydrophobic surfaces continue to gain popularity due to their hydrodynamic advantages including drag reduction and drop-wise condensation, it will be important to understand impingement behavior on these surfaces at elevated temperatures [168,169]. Hydrophobic (HB) and superhydrophobic (SHB) surfaces have shown significant deviation from hydrophilic (HL) behavior in pool boiling [49–51, 157, 170] and are hence expected to also affect droplet impingement boiling dynamics, which has only been explored scarcely [45, 52–54]. In this work, attention is given to "secondary atomization" and its behavior with time, surface temperature and surface type.

First, we provide a brief review of what is known regarding droplet impingement dynamics on heated hydrophilic surfaces. At surface temperatures within a few degrees of saturation temperature, the droplet spreads, sticks to the surface and exhibits minimal boiling behavior during its lifetime [24, 30, 151, 152]. The major mode of heat transfer here is due to convection and evaporation. For higher surface temperatures (tens of degrees above the saturation temperature of the liquid), the droplet is said to be in the nucleate/contact boiling regime and is characterized by vapor bubbles nucleating, growing and bursting, which results in the ejection of micro-sized droplets termed secondary atomization. Latent energy transfer is the major mode of thermal transport in this regime. At surface temperatures much higher than saturation temperature (a few hundreds of degrees above the saturation temperature of the liquid), the droplet rebounds off the surface as though it were superhydrophobic and no signs of boiling or secondary atomization are displayed; this regime is known as film boiling. Such repelling behavior has come to be known as the Leidenfrost effect, having been first reported by Leidenfrost [44], and occurs due to a vapor film that prevails between the droplet and the surface. When hydrophilic surfaces are textured with micropillars (1 - 10 μm), the transition temperature to film boiling (also known as the Leidenfrost point, LFP) is lower because the increase in liquid-solid contact area promotes higher liquid to vapor conversion [11,45].

This paper focuses on secondary atomization, which we define as ejected droplets (also known as secondary droplets) due to bursting vapor bubbles and *not* ejected droplets from the periphery of the lamella due to droplet breakup. Chaves et al. explained the genesis of a secondary droplet in that when a growing/rising vapor bubble reaches the top liquid-air interface of the droplet (commonly referred to as the lamella when spreading), it bursts when the liquid film between the vapor and the air becomes thin enough [171]. Consequently, the liquid seeks to minimize its surface energy by filling in the resulting “concavity” and in doing so, a Rayleigh jet forms begetting a secondary droplet. Vapor bubble diameters are on the order of 10^2 to 10^3 μm [171], while secondary droplets remain around 10^2 μm in diameter [166], having also been confirmed in the present study. Secondary atomization does not start immediately following droplet impact because not enough heat has been transferred to nucleate and grow vapor bubbles [43,166,172]. The duration of this period of time before secondary atomization begins is on the order of a few milliseconds but varies with surface temperature, solid/liquid thermal properties and impact Weber number, $We = \rho V^2 D/\sigma$, where V, D, ρ and σ represent impact velocity and diameter, and liquid density and surface tension [172]. Interestingly, secondary droplets can fly off at speeds exceeding that of the droplet at impact. For instance, Lee et al. measured atomization speeds of 4.2 m/s for a droplet impact speed of 1.97 m/s [148].

This study will show that secondary atomization dynamics unfold differently on HB and SHB surfaces than on HL surfaces. The following description summarizes the relevant work available in the literature regarding general boiling on HB/SHB surfaces. The attraction between a vapor bubble and a HB surface promotes the formation of a vapor film and thus transition to film boiling occurs at a lower temperature than on a hydrophilic surface during pool boiling [49, 170]. In the case of a SHB surface, the critical heat flux is much lower ($< 85\%$) than on a hydrophilic surface [51] and similar behavior was observed for a hot sphere immersed in a liquid bath [157]. These dynamics have been attributed to the hydrophobic texture upon which water can rest thus trapping gas prematurely at the interface inhibiting heat transfer [157]. In a previous publication, the current authors revealed that atomization is almost completely suppressed during droplet impingement on a superhydrophobic surface over the range $125°\mathrm{C} < T_s < 340°\mathrm{C}$, where T_s represents surface temperature. However, the study only employed a single superhydrophobic surface. Here, in-depth consideration is given to the temporal evolution of the amount of secondary atomization on SHB surfaces with varying pitch or center-to-center spacing.

Previous methods, such as phase doppler anemometry [173, 174], particle image velocimetry [148] and droplet counting [166, 175], have revealed essential characteristics of secondary droplets including size, speed and population. In this paper, focus is instead given to time scales including the onset and cessation of atomization, as well as to the comparison of atomization intensities across different surfaces and temperatures during spreading. Previous methods were deemed unsuitable due to their low resolution in comparing atomization intensity across different cases. Thus, a new algorithm was developed and implemented.

The manuscript will proceed as follows. First, a description of the experimental setup used in these experiments is described in Sec. 5.4. A general discussion of the dynamics of secondary atomization for hydrophobic and superhydrophobic surfaces is discussed in Sec. 5.5. After the image processing algorithm is discussed in Sec. 5.6, the temporal behavior of secondary atomization for three different superhydrophobic surfaces and one smooth surface at different surface temperatures will be presented in Sec. 5.7. Finally, conclusions are presented in Sec. 5.8.

5.4 Experimental Setup

Secondary atomization during a droplet impingement event was analyzed for a range of surface temperatures and surface architectures (one smooth hydrophobic and three textured superhydrophobic surfaces). The experimental setup and surface fabrication methodology has been previously described [45] and thus is only briefly outlined here. Details pertaining to the manner of data processing and quantification of atomization will be described in Sec. 5.6.

Three SHB surfaces were fabricated by standard photolithography and etching techniques. Silicon wafers (500 μm thick and 10 cm in diameter) were used as the substrate. All SHB surfaces consisted of a square-lattice arrangement of circular pillars 4 μm in height and a solid fraction of 11% (solid fraction is defined as the area of the top of the pillars divided by the projected area of the surface). The three different pitches used were 8 μm (pillar diameter, $d = 3$), 12 μm ($d = 4.5$) and 16 μm ($d = 6$), and we shall refer to these surfaces as 8P, 12P and 16P throughout the paper. A 200 nm coat of Teflon was applied on all surfaces to render them superhydrophobic. The advancing and receding contact angle on these surfaces were typically 168° and 145° ±3°, respectively. Additionally, a fourth surface was fabricated by applying Teflon on a smooth silicon wafer (referred to as the smooth hydrophobic surface here), which yielded an advancing and receding contact angle of 128° and 113° ±3°, respectively.

A syringe filled with distilled water was positioned 15 cm above the surface of interest such that a droplet (~ 5 μL) would impact the surface at $We \approx 85$. This Weber number value was chosen to allow the droplet to spread out without incurring peripheral droplet ejection [8] and was kept nominally constant for all scenarios. The surface was positioned on top of a polished aluminum block which was heated by embedded cartridge heaters. A thermal camera was used to determine the temperature of the surface during testing. The range of surface temperatures explored was $110°\text{C} < T_s < 337°\text{C}$ to avoid degradation of the Teflon coating, which occurs at higher temperatures. A high-speed camera was positioned horizontally to record impingement events at 3000 fps and each scenario was repeated 5 - 8 times. A halogen lamp was positioned opposite to the camera for optimum illumination. Despite the fact that halogen lamps are traditionally considered to be a “constant” light source, when connected to AC power subtle oscillations in pixel intensity (1% - 5% of maximum possible pixel value) were detected by the camera. In order to mitigate this effect, the lamp was instead connected to a DC power source and operated at 400 watts.

The impact Weber number was determined as follows. The projected area of the droplet, as viewed from the camera, was calculated during its descent. The diameter prior to impact was obtained assuming the measured area was circular, which was nominally the case since the diameter of the droplet (≈ 2.2 mm) always remained below the capillary length of water (≈ 2.7 mm). The impact velocity was obtained from a linear fit to the position of the center of gravity of the droplet during descent. Dynamic viscosity and surface tension values were evaluated at room temperature and uncertainty in these quantities was based on temperature fluctuations of $\pm 1.5°$C. Droplet impact diameter and velocity had an uncertainty of $\sim 1\%$. Overall uncertainty in the Weber number based on a 95% confidence interval was $\pm 3\%$.

5.5 General Dynamics

Prior to disclosing details regarding the manner of quantification of secondary atomization, general dynamics will be discussed here qualitatively to aid the reader in understanding the subsequent processing methodology and results. A representation of secondary atomization for a typical droplet impingement event on a SHB surface is shown in the schematic of Fig. 5.1. A small period of time, t_i, prevails immediately following impact where secondary atomization is not present as discussed earlier for a hydrophilic surface. In these experiments, the Weber number, as well as the solid-liquid thermal properties were held constant yielding $t_i \approx 0.8$ ms generally across all cases where atomization was present.

For $t > t_i$, the amount of atomized liquid increases with time as vapor bubbles continue to burst. This trend continues until $t = t_f$ when secondary droplets cease to be ejected, and the amount of atomized liquid remains constant with time (shown in Fig. 5.1). Cessation of atomization is attributed to a decrease in the local temperature of the solid, as well as a now-heavily bubble-populated interface [166], both of which mitigate heat transfer. Technically, atomization will eventually resume as the surface temperature heats up again ($t >> t_f$), however, the time frames considered here are relatively short and this does not occur. t_f values reported by Moita et al. varied between a few milliseconds up to 20 ms for impingement on a hydrophilic surface. Here, $t_f \approx 2.5$ ms on the 8P surface and ≈ 3.0 ms on the smooth surface for the range of surface temperatures explored. Sometimes, the droplet was observed to levitate above the surface during spreading due to droplet breakup (photographs in Fig. 5.1). This occurs due to liquid film shrink-

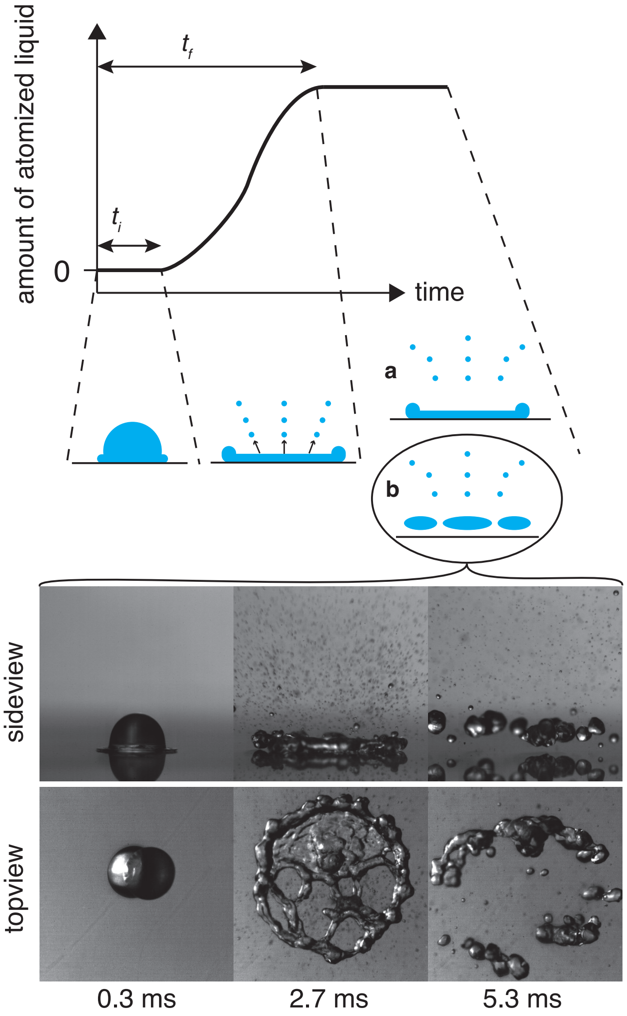

Figure 5.1: Representative evolution of the amount of atomized liquid as a function of time. High-speed photographs represent impingement on the 8P surface at $T_s = 320°\text{C}$ to depict levitation.

ing at the periphery of emerging convection cells, which in turn causes a springing motion in the separated droplets levitating them above the solid surface [171]. This levitating phenomenon did not have an effect on t_f values.

In order to determine whether the amount of atomization at t_f is the maximum, it is important to establish how much of the atomized liquid has either evaporated or fallen back to the substrate by that time. The evaporation of an arbitrary atomized droplet during flight can be estimated by a convection mass transfer analysis. The Sherwood number, $Sh = h_m d/D_{AB}$ (where h_m and D_{AB} are the convective mass transfer coefficient and the binary diffusion coefficient for vapor in air), for a water droplet in air can be expressed as [176]

$$Sh = 2 + 0.6Re^{1/2}Sc^{1/3} \tag{5.1}$$

where $Re = ud/\nu_a$ and $Sc = \nu_a/D_{AB}$ represent the Reynolds number and the Schmidt number, respectively (u and d are the velocity and diameter of the atomized droplet and ν_a is the dynamic viscosity of the medium or air in this case). Values for an average secondary droplet size and velocity were obtained from the literature ($d = 150$ μm, $u = 4$ m/s) and were also verified with our experiments. The total mass transfer rate can be obtained via Newton's law of cooling, $\dot{m} = h_m A \Delta\rho$ where $\Delta\rho$ is the difference in vapor density at room and saturation temperature, thus yielding a maximum possible evaporation rate. This analysis yields an evaporation rate of about 4×10^{-8} kg/s. The initial mass of an average secondary droplet is $\approx 1.8 \times 10^{-9}$ kg and hence evaporation causes a mass loss of about 6% by $t = t_f$, and will be neglected.

On the other hand, a simple force analysis in the vertical direction (positive in the direction opposite to the gravitational vector) for an atomized droplet can be utilized to determine the amount of time it spends in the air,

$$m\dot{u} = -mg - \beta du - \gamma d^2 u|u| \tag{5.2}$$

where m and g represent the mass of the atomized droplet and the gravitational constant, and u is a function of time. The two far-right terms on the right hand side of Eq. (5.2) represent the linear and quadratic aerodynamic drag, respectively, and $\beta = 1.6 \times 10^{-4}$ N·s/m^2 and $\gamma = 0.25$ N·s^2/m^4 are the corresponding drag coefficients for a water droplet in air [177]. Here, the movement of the atomized droplet has been assumed to be in the vertical direction, which has been shown to be a good assumption [172] and was observed to be the case for our experiments as well. The solution of Eq. (5.2) yields that the duration of the droplet in air is about 400 ms prior to falling back on the substrate, which is much greater than $t_f \approx 2.5$ ms. Thus, both of the analyses for evaporation and droplet flight time demonstrate that the amount of atomization at t_f is an absolute maximum.

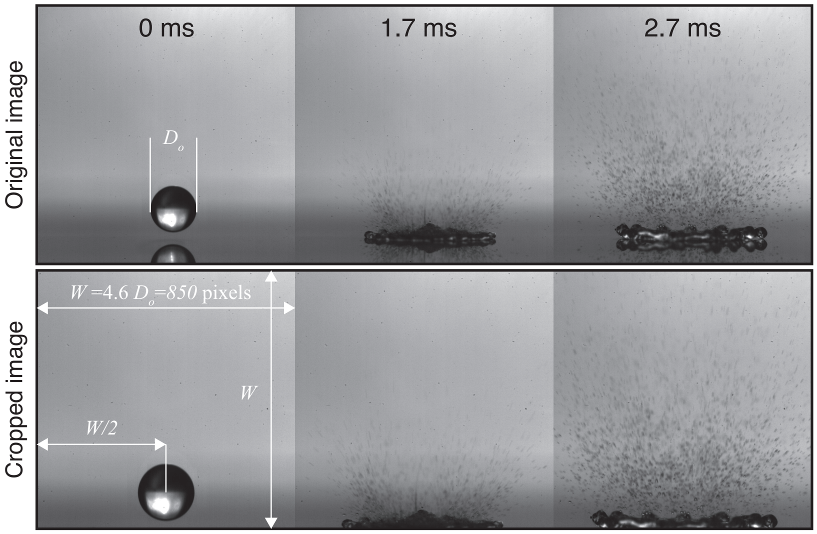

Figure 5.2: Original (top) and cropped (bottom) images for impingement on the 8P surface at $T_s = 200°\text{C}$.

5.6 Digital Image Processing

High-speed photographs of an impingement event on the 8P surface at $T_s = 200°\text{C}$ is shown in Fig. 5.2. The amount of atomization was quantified by analyzing photographs and the methodology is described in this section. However, we first wish to emphasize the difficulty in this task, which arises because atomization is inherently a 3-dimensional phenomenon and photography is 2-dimensional. Other methods presented in the literature that also seek to quantify atomization by processing photographs such as the work by Moita et al. [166] and Castanet et al. [175] are constrained by the same limitations. Photographs include blurred secondary droplets which fall outside the depth of field and omit secondary droplets that become "hidden" behind others or are far from the focus plane. Consequently, the results that will be provided in this paper must be interpreted with this understanding. The results nevertheless yield sufficiently good contrast between the different scenarios considered and agree with visual inspection and the literature.

The first step in the algorithm was to ensure that atomization was weighted in a spatially-consistent manner across all scenarios. The original images were 1024 × 1024 pixels (top panel of Fig. 5.2). To achieve horizontal symmetry, images were cropped to a width, W, of 850 pixels ($\approx 4.6 \times D_o$) with the droplet in the center, as shown in the bottom panel of Fig. 5.2. Given that maximum spread diameter is $\approx 3 \times D_o$ for $We = 85$ [32], the entire droplet was able to fit in the reduced frame at all times during spreading thus allowing atomization stemming from the droplet to be within the field of view (atomization eventually escaped the cropped frame and this effect will be quantified later). Images were also cropped vertically 850 pixels above the droplet-surface interface.

Resulting cropped images will be denoted by I_{ij}^{k} where k represents the time step, and i and j represent the row and column location of a pixel. Y and X will denote the maximum number of rows and columns, respectively ($Y = X = 850$ for all images). I_{ij}^{0} represents the image when the droplet first hits the surface at $t = 0$ ms and the time corresponding to subsequent images, I_{ij}^{1}, I_{ij}^{2}, ... can be calculated by $t = k/\text{fps}$ ms (fps $= 3000$ s^{-1} in this paper unless stated otherwise). A background image, which consisted of an image with no droplet (referred to as an empty frame), was defined as $\mathscr{O}_{ij}$. We note that all images were 8-bit grayscale color graphics and thus possible pixel values ranged from 0 to 255. All subsequent variables will assume a normalization by 255 yielding values which fall within 0 and 1 (0-black and 1-white).

In order to identify the location of the droplet and the amount of atomization present, the absolute value of the subtraction of every image with the background image was calculated,

$$S_{ij}^{k} = |I_{ij}^{k} - \mathscr{O}_{ij}| \tag{5.3}$$

where S_{ij}^{k} will be referred to as the subtracted image. A binary threshold was determined based on the average random noise present in the images, which was calculated by subtracting $N = 100$ different background images from each other and calculating the average pixel value, $\mathscr{O}_{ave}$, across all subtractions as follows

$$\mathscr{O}_{ave} = \frac{1}{Y \times X} \sum_{i}^{Y} \left[\sum_{j}^{X} \left(\frac{1}{N} \sum_{n, n \neq m}^{N} |\mathscr{O}_{ij}^{n} - \mathscr{O}_{ij}^{m}| \right) \right] \tag{5.4}$$

The average random noise had a nominal value of $\mathscr{O}_{ave} = 0.0036$ with a standard deviation of 0.0028. The binary threshold value was chosen to be six standard deviations above the mean, $0.0036 + 6 \times 0.0028 = 0.0204$. The first two columns of Fig. 5.3 show the transition from an image I_{ij}^{k} to a binary image B_{ij}^{k} for three arbitrary cases.

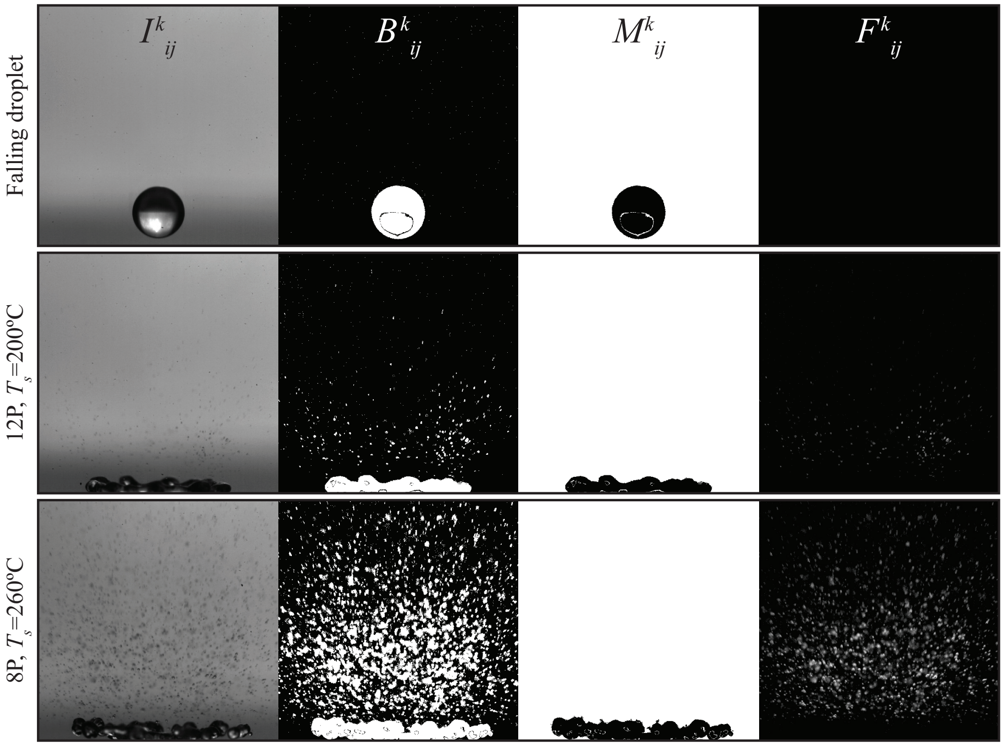

Figure 5.3: Representation of images at every step during processing for three arbitrary cases: a falling droplet (top), moderate atomization (middle) and heavy atomization (bottom). I^k_{ij}, B^k_{ij}, M^k_{ij} and F^k_{ij} represent the initial image (after cropping), the binary image, the mask used to remove the droplet, and the final image from which an average pixel intensity value to represent the amount of atomization was obtained.

In order to remove the main droplet from the images and only consider atomization, a mask, M^k_{ij}, was utilized (see third column of Fig. 5.3). Here, a value of 0 was assigned to all areas in B^k_{ij} with more than 10×10^3 connected pixels (having been determined *a posteriori*) and a value of 1 elsewhere. The remaining active pixels in B^k_{ij} were used as a second mask (not shown in Fig. 5.3) on S^k_{ij} to reduce background noise on the final image, F^k_{ij} (fourth column of Fig. 5.3), and only consider pixels containing atomization. In short, the formula applied to all images is given by

$$F^k_{ij} = |I^k_{ij} - \mathscr{O}_{ij}| \circ M^k_{ij} \circ B^k_{ij} \tag{5.5}$$

where ∘ represents the Hadamard product. A spatial average of F^k_{ij} was obtained by

$$A^k = \frac{1}{Y \times X} \sum_{i}^{Y} \left[\sum_{j}^{X} \left(F^k_{ij} \right) \right] \tag{5.6}$$

Table 5.1: Intensity-to-noise ratios for impingement at $T_s = 200°\text{C}$ on the 8P and 16P surfaces (top two rows) and intensity-to-intensity ratio between the surfaces (bottom row).

	12 μm (%)	22 μm (%)	51 μm (%)
PD_1 (16P)	120	40	20
PD_1 (8P)	8850	1780	320
PD_2	4420	1360	280

to yield the atomization intensity, A^k, in a given image. From now on, A^k will just be denoted as A, is unitless (given the aforementioned normalization) and is assumed to be a function of time.

Next, pixel resolution is considered, which refers to the physical length scale covered by a single pixel. Pixel resolution is inversely related to the size of the field of view and both a large field of view and sufficiently high resolution are desired. Three different resolutions were tested: 12 μm, 22 μm and 51 μm (per pixel side length), with 12 μm being the highest resolution possible in our experimental setup. For all of these cases, the frame size was constant at 850×850 pixels, which resulted in physical frame side lengths of 10.2 mm, 18.7 mm and 43.4 mm, respectively (recall droplet diameter $\approx$ 2.2 mm). The 8P and 16P surfaces, which generally yielded the largest and lowest amount of atomization, respectively, were tested at each of these resolutions for $T_s = 200°\text{C}$ and each test was repeated three times. The averaged results shown in Table 5.1 represent the percent difference, PD_1, between the maximum atomization intensity during impingement, A_{max}, and noise, A_{min}, for each surface,

$$PD_1 = (A_{max} - A_{min})/A_{min} \times 100\% \tag{5.7}$$

Percent differences of the maximum intensities between both surfaces, PD_2, were also calculated

$$PD_2 = (A_{max,8P} - A_{max,16P})/A_{max,16P} \times 100\% \tag{5.8}$$

These results indicate that the signal-to-noise ratio for either surface, as well as the intensity ratio between them increased significantly with increasing pixel resolution (51 μm $\rightarrow$ 12 μm). The images in Figures 5.2 and 5.3 correspond to a resolution of 12 μm.

Next, we evaluate the effect of pixel resolution on field of view. Figure 5.4a shows the temporal evolution of A on the 8P surface at $T_s = 200°\text{C}$ with a resolution of 12 μm. The data shows that A is zero until $t \approx 0.8$ ms, as expected, after which point it begins to increase with time. After reaching a maximum point at $t \approx 2.5$ ms, A begins to decrease. This decrease is not physically realistic since we have shown that secondary droplets do not evaporate significantly or fall back to the substrate within this window of time, but occurs here because they escape the field of view of the camera. A pixel resolution of 51 μm was used to enlarge the field of view and ensure that all atomization fell within the camera view at all times. A comparison of the amount of atomization in these larger images was compared to a cropped image equivalent to the physical size of the 12 μm resolution images. Figure 5.4b,c show the percent of the atomization not captured by the cropped image as a function of time. The results indicate that atomization begins leaving the field of view at $t \approx 2.7$ ms for the 8P surface and $t \approx 3.5$ ms for the smooth surface (these tests were performed at surface temperatures where the maximum amount was observed). The amount of escaped atomization naturally increases with increasing time as secondary droplets continue to leave the field of view. In this paper, we limit our analysis to $t < 2.7$ ms, this being the time at which secondary droplets escape the field of view for the highest atomizing surface at a pixel resolution of 12 μm is used.

Now we quantify the influence of using a single or an averaged background image (based on an array of 100 images) on the temporal evolution of A. Impingement events on the 8P and 16P surface at $T_s = 260°\text{C}$ and 170°C, respectively, were analyzed. Data showed that using an averaged background image yields an atomization intensity nominally 1% - 2% lower of the maximum atomization intensity value on the 8P surface ($A \approx 10.8 \times 10^{-3}$) compared to using a single background image. Atomization intensity on the 16P surface was virtually unaffected by the choice of background. Consequently, all results will be based on a single background image.

The last consideration that shall be given regards scenarios for which significant atomization was present (Fig. 5.5). Here, the masking process described earlier caused the pixels from the main droplet to be connected to some pixels containing atomization in B_j (second panel of Fig. 5.5). This resulted in the mask assuming a droplet shape that included a significant portion of the atomization region (third panel of Fig. 5.5). This type of behavior only occurred on the 8P and smooth surfaces at surface temperatures above 230°C and 260°C, respectively, and typically

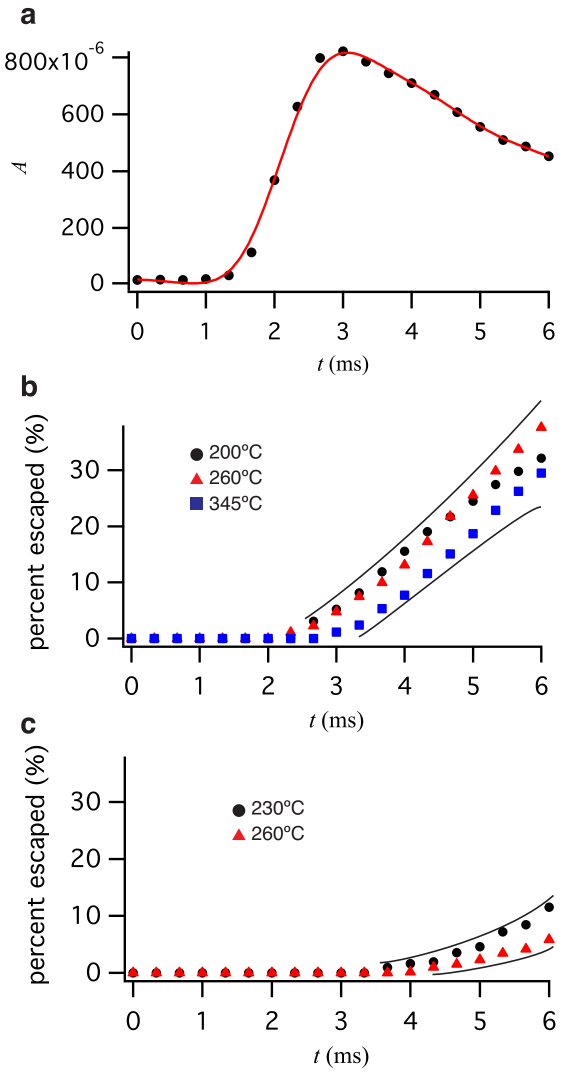

Figure 5.4: (a) Atomization intensity for droplet impingement on a 8P surface at $T_s = 200°\mathrm{C}$ as shown in Fig. 5.2. (b) and (c) Percentage of atomization that escapes the field of view when pixel resolution is 12 μm as a function of time for impingement on the 8P (b) and smooth (c) surface. Solid lines represent the maximum and minimum values.

ceased for $t \geq 3.5$ ms when the atomization began to dissipate. For $t < 3.5$ ms, a new mask was created with a shape more representative of the droplet. To accomplish this, the pixel location belonging to the highest point of the main droplet, y_m, was manually selected at every time step from I^k_{ij} such that all pixels from the mask above the horizontal line were removed. This resulted in a modified mask, which more closely represented the shape of the main droplet (last panel of Fig. 5.5). However, the horizontal crop along the top of the droplet caused pixels where atomization was present to be removed, shown in red in M_j-modified. To evaluate the influence of this on

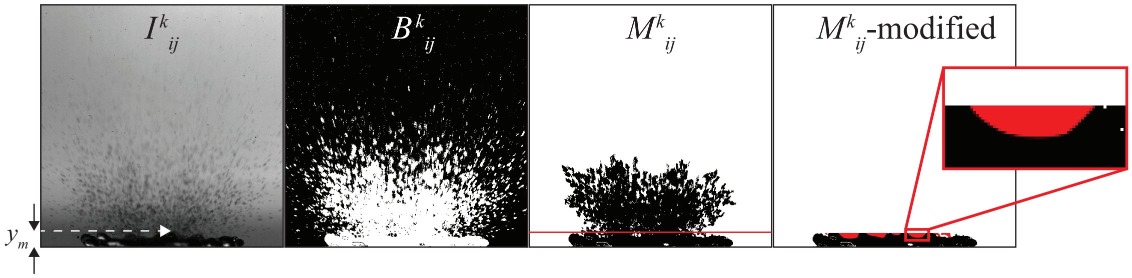

Figure 5.5: a) Impingement on the 8P surface at $T_s = 260°\text{C}$ and $t = 2$ ms where the creation of new mask, M^k_{ij}-modified, to remove the droplet was necessary due to the large amount of atomization.

the results, the amount of removed atomization was calculated for impingement on the 8P surface at $T_s = 260°\text{C}$ as a function of time. The average amount of atomization intensity removed was nominally 7×10^{-5}, which resulted in around 1% of the maximum A.

Thus, the image processing algorithm captures secondary atomization in a quasi-2-dimensional manner. Resulting absolute intensity values in and of themselves do not represent a physical quantity, but rather they are useful in a relative sense when comparing to other scenarios (whether as a function of surface temperature or type).

5.7 Secondary Atomization

5.7.1 Smooth Hydrophobic Surface

Secondary atomization dynamics on the HB surface will be discussed first followed by a discussion on the SHB surfaces. Figure 5.6a depicts the temporal evolution of A on the smooth HB surface for $138°\text{C} < T_s < 226°\text{C}$. The data shows that atomization does not occur for a surface temperature of 138°C. The heat transfer to the droplet at this temperature is insufficient for vapor bubbles to grow and burst during spreading/retracting [45]. For higher surface temperatures, atomization takes places for $t > 0.8$ ms (shown in the inset) and A increases with T_s for all times. As can be seen in the main plot of Fig. 5.6a, atomization is modest for $T_s = 167°\text{C}$, but the image processing algorithm is able to detect its presence and growth with time (as can be seen in the inset image). Higher atomization intensity with increasing surface temperature is due to higher vapor production rates at the solid-liquid interface, which induces faster vapor bubble growth.

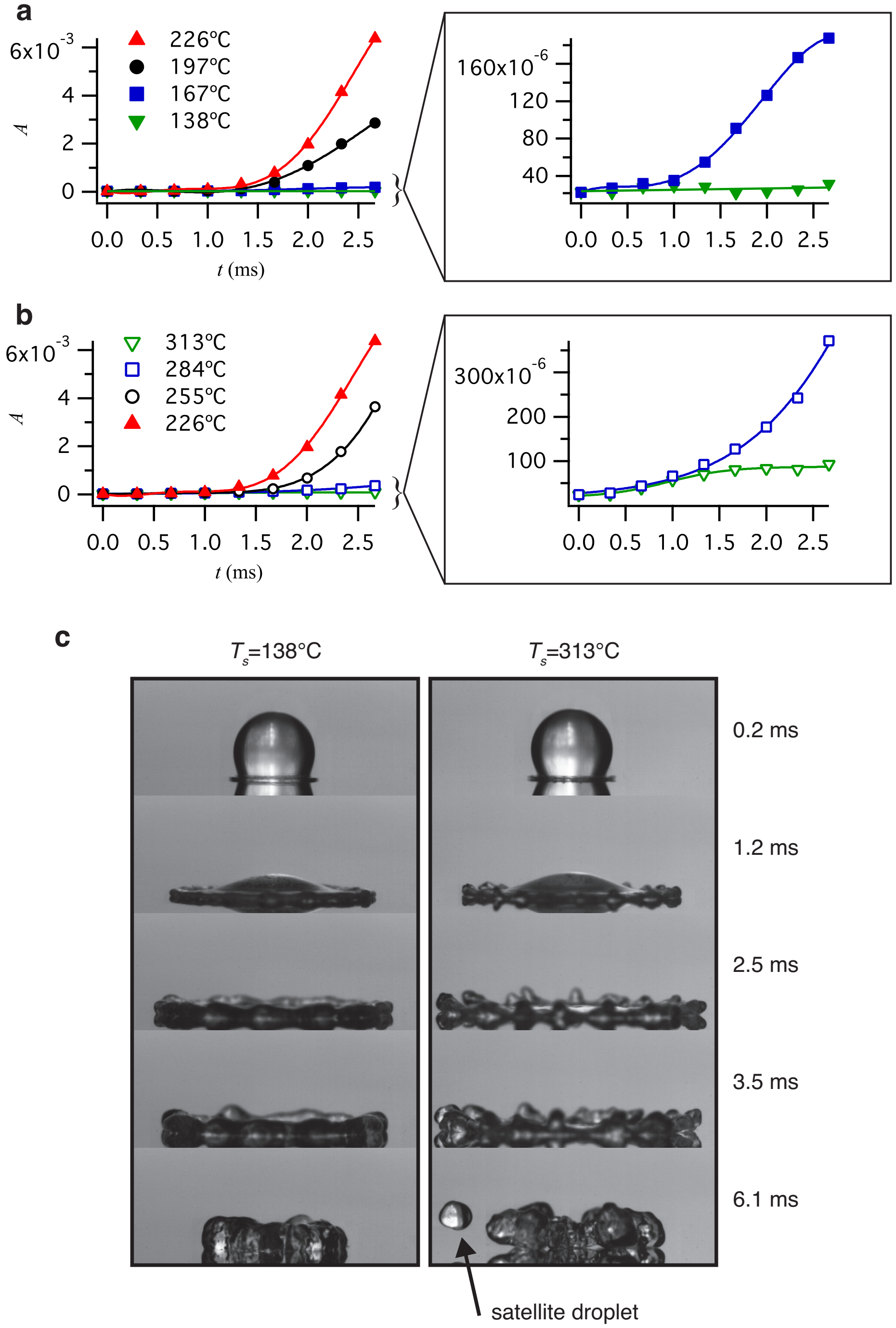

Figure 5.6: Temporal evolution of A for the HB surface. Surface temperatures between 138°C and 226°C are conisdered in (a) and between 226°C and 313°C in (b). (c) Droplet impingement at $T_s = 138$°C and 313°C for which atomization was not present.

Figure 5.6b displays results for A on the smooth surface for surface temperatures of 226°C and higher (data for $T_s = 226°\text{C}$ is shown in both (a) and (b) for comparison). Here, surface temperature causes an opposite effect in that atomization intensity decreases with increasing T_s. For the highest surface temperature, $T_s = 313°\text{C}$, atomization has ceased and remains absent up to 337°C (not shown). Decreasing atomization with surface temperature is due to the formation of the so-called vapor blanket, which yields Leidenfrost behavior and atomization becomes absent due to vapor escape through the vapor blanket. The two scenarios devoid of atomization in Figure 5.6a and b, one occurring at the beginning of the contact boiling regime (138°C) and one at the end (313°C) deserve further consideration. High-speed photographs of these two scenarios are shown in Fig. 5.6c and interestingly depict different spreading behavior. The droplet on the $T_s = 138°\text{C}$ surface exhibits classic droplet spreading and retraction behavior whereas the droplet on the $T_s = 313°\text{C}$ surface spreads out farther promoting peripheral (or satellite) droplet formation. This is evidenced by the bulbous lamellar ring (compare images corresponding to $t = 2.5$ ms). Satellite droplets eventually detach from the main droplet, as can be observed by 6.1 ms. Given the 175°C difference between both cases, one might suspect that this temperature difference is the cause of peripheral droplet ejection. However, we know that the droplet temperature in both cases remains below saturation, $\approx 100°\text{C}$, since the droplet remains in the liquid state. Therefore, the observed difference is instead attributed to a larger slip boundary condition which is associated with a full vapor blanket ($T_s = 313°\text{C}$) rather than a partial one ($T_s = 138°\text{C}$). It has been shown that larger slip causes droplets to spread out farther and consequently promotes satellite droplet formation [32].

The maximum values of atomization intensity during a given event, A_{max}, on the smooth surface (corresponding to Fig. 5.6) as a function of surface temperature are shown in Fig. 5.7. The data (symbols) shows that atomization is absent for very low and very high excess surface temperatures with a maximum, $A_{s,max}$, at $T_s = 226°\text{C}$, as previously discussed. A gaussian curve was used to fit the data (solid line), which shows good agreement with the behavior, and is similar to that of heat flux vs. excess temperature for pool boiling. In that case, heat flux also increases up to some maximum point (known as the critical heat flux) and then decreases towards the Leidenfrost point. Our data discloses for the first time a similar rise-and-fall behavior of atomization during the contact boiling regime for impinging droplets. While other work has identified that atomization is present during contact boiling [8, 9, 24], the current work represents the first relative quantifi-

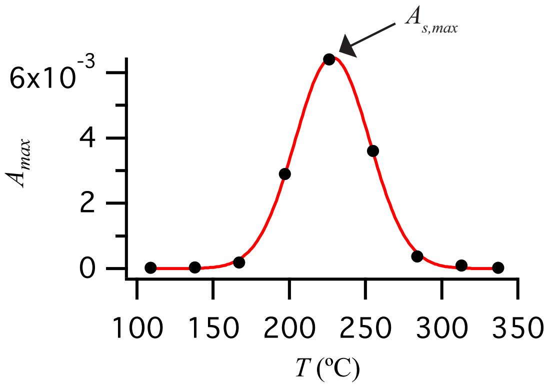

Figure 5.7: The maximum of atomization intensity on the smooth hydrophobic surface at a given surface temperature as a function of surface temperature. Curve represents Gaussian curve fit of data points and $A_{s,max}$, the maximum value of the data set, is used as a normalization constant for subsequent results.

cation of atomization intensity changes within this regime. Further implications of these results, such as the relationship between heat flux and atomization, remain open-ended and require further investigation.

5.7.2 Superhydrophobic Surfaces

Next we present results pertaining the SHB surfaces. For comparative purposes, atomization intensities on the SHB surfaces will be normalized by the maximum value on the smooth surface, $A_{s,max}$, shown in Fig. 5.7. Figure 5.8 depicts dynamics at $T_s = 197°\text{C}$ for all SHB surfaces. The data show that atomization is absent on the 16P surface for all time, while it increases with time on the 12P and 8P surfaces. The maximum value of atomization intensity here falls within 12% of atomization on the smooth HB surface. Intensity is higher for decreasing pitch, and is rationalized as follows. Since gas cavities prevail within the textured interface (since water remains suspended above the texture) and allow vapor to escape thus preventing vapor bubbles from forming as rapidly [45]. However, resistance to vapor flow increases with decreasing pitch since the distance between adjacent pillars becomes smaller inducing larger velocity gradients and thus atomization increases. This has been verified elsewhere for micro-pillars of similar height and the

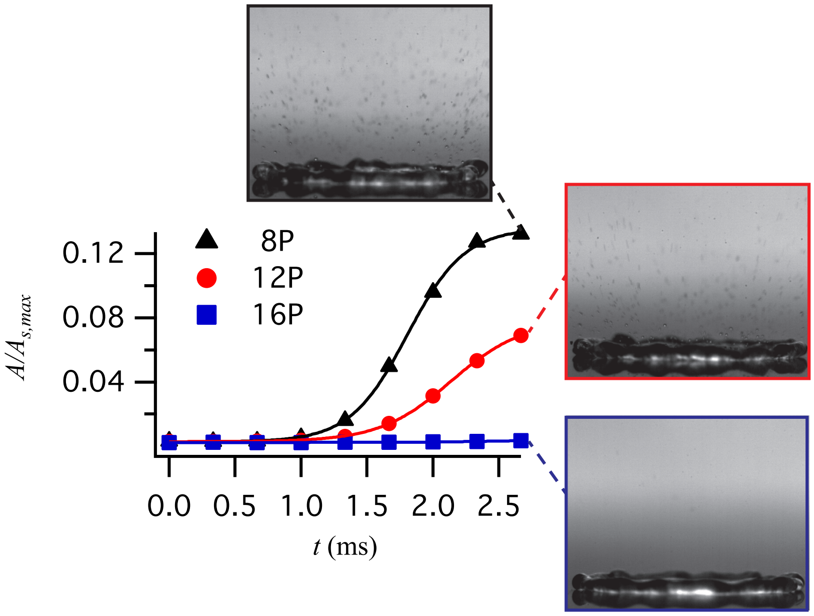

Figure 5.8: Atomization intensity on all superhydrophobic surfaces normalized by $A_{s,max}$ as a function of time for $T_s = 197°\mathrm{C}$. Photographs represent impingement on their corresponding surfaces at $t \approx 2.3$ ms.

drag force, F, was found to be inversely related to pitch, p, as follows [135]

$$F \propto \frac{1}{p^2 \ln(p)} \tag{5.9}$$

This relation demonstrates the steep increase in drag resistance on the escaping vapor with decreasing pitch. Of course, bubble growth is also dependent on the solid-liquid contact area, which influences the heat transfer. However, in this work all SHB surfaces exhibit similar solid fractions and thus similar solid-liquid contact area. Consequently, atomization increases with decreasing pitch due to increasing resistance to vapor flow, as demonstrated by the data.

Now we consider atomization on the 8P surface more in depth as it is the highest atomizing SHB surface. Figure 5.9 shows $A/A_{s,max}$ as a function of time for surface temperatures between 138°C and 226°C (top panel), and between 226°C and 337°C (bottom panel). The data in the top panel shows that increasing surface temperature results in increasing atomization intensity, which is similar to behavior on the smooth surface. Interestingly, data in the bottom panel shows that A continues to increase with increasing surface temperature from 226°C to 313°C. This is in contrast to the smooth surface, where atomization began to decrease for $T_s > 226°\mathrm{C}$ as the interfacial

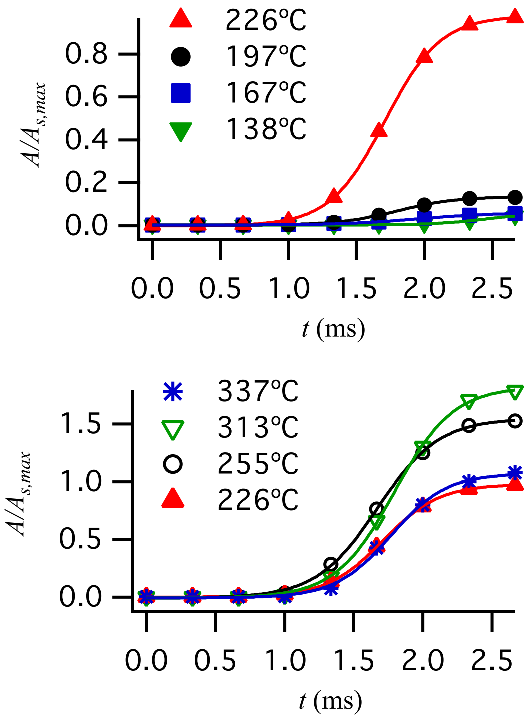

Figure 5.9: Atomization intensity on the 8P surface normalized by $A_{s,max}$ as a function of time. The top panel shows results for surface temperatures between 138°C and 226°C while the bottom panel shows results between 226°C and 337°C.

vapor film matured. Nonetheless, atomization eventually decreases at $T_s = 337°\text{C}$ indicating that atomization on the 8P surface reaches a maximum at a surface temperature of about 313°C. Furthermore, decreasing atomization with temperature suggests that a Leidenfrost point on this surface exists, though the temperature at which this occurs remains unknown given the physical limitation of the Teflon coating used here.

The data in Fig. 5.9 further shows that for $T_s = 255°\text{C}$ and 313°C, atomization intensity is 50% to 70% higher on the 8P surface than the greatest value for the smooth surface. This is unexpected given the presence of cavities at the superhydrophobic interface, which should facilitate vapor escaping and mitigating atomization. To investigate further, additional experiments were performed on a SHB surface also with a 8 μm pitch pillar arrangement, but taller pillar height, $h = 14$ μm (recall for the 8P surface, $h = 4$ μm). These results are shown in Fig. 5.10 and demonstrate that atomization intensity at 313°C on the $h = 14$ μm is actually higher than on the $h = 4$ μm surface for all t. These results indicate that while gas cavities at a superhydrophobic

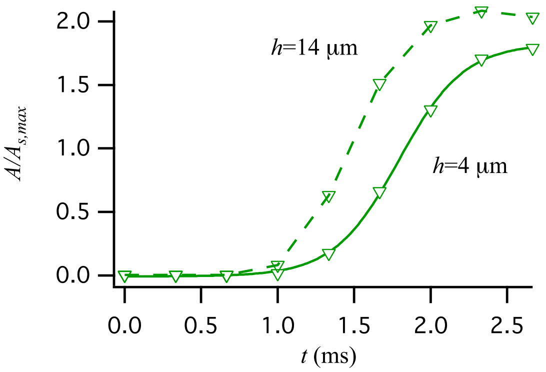

Figure 5.10: Atomization intensity normalized by $A_{s,max}$ for a superhydrophobic surface with a pitch of 8 μm and pillar height, $h = 4$ μm (same as Fig. 5.9), and $h = 14$ μm.

interface allow vapor to escape, they also promote liquid contact at the peak of the texture since the vapor can now dwell in the cavities. In other words, on a smooth surface, the vapor blanket separates the liquid and solid phases, however, on a superhydrophobic surface, vapor can dwell inside the cavities prolonging solid-liquid contact. Here, the $h = 14$ μm surface has over three times the volume for vapor to dwell in as the $h = 4$ μm pitch surface and this may be responsible for increased solid-liquid contact and hence higher atomization (a systematic study of the effect of pillar height on atomization is beyond the scope of this paper). Thus, two competing mechanisms exist. Vapor escape through the cavities, which mitigates bubble formation, and prolonged solid-liquid contact, which enhances local bubble formation. When the latter behavior is dominant, higher atomization than a smooth surface may result illustrating that superhydrophobic surfaces may not always be advantageous over smooth surfaces in applications requiring low atomization.

Finally, the relationship between the maximum atomization intensity for each of the SHB surfaces and surface temperature is shown in Fig. 5.11. Here we show that increasing atomization with decreasing pitch holds for all surface temperatures during contact boiling. The data further show that all pitches exhibit negligible atomization at $T_s = 110$°C, which is expected given the low excess surface temperature. The 16P surface exhibits a maximum at $T_s = 138$°C, after which it decreases with surface temperature. The 12P and 8P surfaces display similar behavior but the maximum values occur at $T_s = 226$°C and 313°C, respectively. Similar to Fig. 5.7, here, the rise-and-fall of atomization is evident and atomization disappears as surface temperature approaches the Leidenfrost point (not reached on the 8P surface). These results make clear that surface pitch

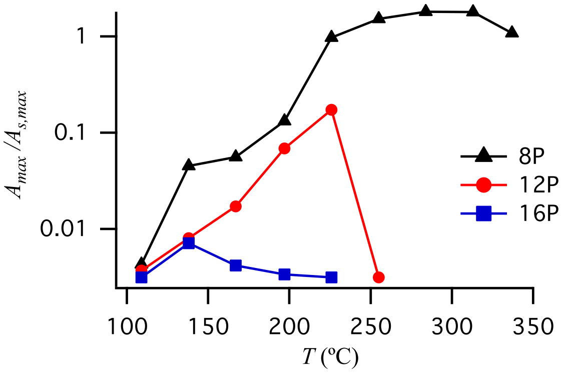

Figure 5.11: The maximum amount of atomization on all superhydrophobic surfaces for a given surface temperature normalized by $A_{s,max}$ as a function of surface temperature.

affects the temperature at which maximum atomization occurs as well as the LFP with the value of each occurring at lower surface temperatures for increasing pitch.

5.8 Conclusions

In this paper, secondary atomization resulting from droplet impingement on hydrophobic and superhydrophobic surfaces was investigated. An image processing algorithm was developed to analyze high-speed photographs and compare atomization intensity across different scenarios. Surface temperatures ranged from 110°C to 337°C and the Weber number was maintained constant at 85 for all tests. The results show that secondary atomization intensity versus surface temperature follows a similar trend to heat flux vs. surface temperature in pool boiling. Namely, atomization intensity increases with increasing surface temperature and after reaching a maximum value, it begins to decrease as the vapor film at the interface becomes stabilized (film boiling). Atomization on the superhydrophobic surfaces was found to depend largely on the center-to-center spacing between adjacent pillars (pitch). The surface with the smallest pitch induced the greatest atomization for all surface temperatures and atomization always decreased for increasing pitch values. This behavior was attributed to increasing resistance to vapor flow through the micro-pillar forest with decreasing pitch values. The Leidenfrost point was consequently found to be dependent on pitch and occurs at higher temperatures for decreasing pitch values. Atomization is not always less on a superhydrophobic surface than on a smooth one, as previously supposed [45]. A hypothesis was presented arguing that the amount of secondary atomization depends on a balance between solid-liquid contact and resistance to vapor flow.

CHAPTER 6. CONCLUSIONS

This dissertation explored the physics of single droplet impingement on micro-structured superhydrophobic surfaces. Attention was given to the effects of slip velocity on spreading/retracting (Chapter 2), Wenzel-to-Cassie transition (Chapter 3), general dynamics at surface temperatures above saturation (Chapter 4) and secondary atomization intensity on different superhydrophobic surfaces (Chapter 5). Analytical, numerical and experimental approaches were utilized throughout this work. The preferred method of experimental exploration included high-speed photography to capture the impingement events, image processing to extract desired parameters from the high-speed photographs, and photolithography to fabricate the superhydrophobic samples.

Superhydrophobic surfaces are said to yield a slip boundary condition due to the periodic gas-liquid (nearly shear free) contact at the interface. An analytical model was developed to analyze isotropic or axisymmetric slip during droplet impingement. The results showed that larger slip leads to larger spreading diameters. This behavior is associated with a decrease in viscous dissipation such that kinetic energy remains higher during the event. In order to analyze anisotropic slip (representative of a superhydrophobic surface with uni-direction ribs/cavities), the governing equation derived for the analytical model was discretized in the azimuthal direction. These results also showed that larger spreading diameters occur due slip, but preferential spreading occurred in the longitudinal direction of the ribs concomitant with larger slip. This resulted in elliptical-type shapes during spreading. Experiments were performed and agreed with the models.

When liquid resides on top of the superhydrophobic texture, the liquid is said to be in the Cassie state. On the other hand, when liquid penetrates into the cavities, it is said to be in the Wenzel state. The advantages posed by superhydrophobic surfaces due to slip are often voided when transition occurs from the Cassie to the Wenzel state. We investigated transition form the latter to the former when penetration occurred during droplet impact. Experiments revealed that tall micro-pillars (relative to the center-to-center spacing of the texture) and elevated surface temperatures permitted liquid to revert back to the Cassie state. A scaling analysis was developed to explain the observed behavior and conclusions are as follows. Increasing pillar height increases an effective driving potential for flow to dewet the cavities. This driving potential is based on the interfacial energy between all immiscible phases at the interface. On the other hand, increasing surface temperature caused resistance to dewetting to decrease. This resistance was due to hydrodynamic and non-hydrodynamic (molecular hopping at the triple contact line) dissipation forms.

Given the ever increasing need for higher heat fluxes, an investigation was also performed for droplet impingement on surfaces heated above the saturation temperature of the liquid. This study was two fold. First, dynamics were investigated on surfaces varying across the entire wettability spectrum: superhydrophilic, hydrophilic, hydrophobic and superhydrophobic. The results revealed that the hydrophilic surface exhibited the highest temperature for the Leidenfrost point, or temperature where atomization ceases to occur. The superhydrophilic surface followed and its lower temperature was due to the increased solid-liquid contact area provided by the texture. The hydrophobic surface also had a lower Leidenfrost point temperature, but in this instance, this behavior was due to vapor bubbles being more attracted to the surface thus promoting the formation of a vapor film earlier. The most striking behavior in this study was that secondary atomization on the superhydrophobic surface was nearly absent at all surface temperature explored. Thus, droplet impingement seemed to “skip” the contact boiling regime and always exhibited film boiling characteristics. This behavior occurred due to the ability of vapor to drain from underneath the droplet through the hydrophobic texture. Finally, maximum diameters were evaluated at their respective Leidenfrost point temperatures and it was found that they were smallest when spreading on a textured surface. This indicates that solid-liquid contact prevails during droplet impingement at the Leidenfrost point.

Second, in order to explore this peculiar behavior of suppressed atomization on superhydrophobic surfaces, a second study was performed using a smooth hydrophobic and four different superhydrophobic surfaces. We found that secondary atomization is not always suppressed on a superhydrophobic surface. In fact, droplets can display larger amounts of atomization than on smooth hydrophobic surfaces. The largest amount of atomization occurred on the superhydrophobic surface with the smallest pitch, which coincides with the idea that the obstruction of vapor flow causes vapor bubbles to prevail and burst, resulting in secondary atomization. Lastly, this study revealed the relationship between secondary atomization and surface temperature, which mimicked the relationship between heat flux and surface temperature for the case of pool boiling. The surface temperatures at which the maximum amount of atomization occurs were provided, as well as the temporal evolution of atomization for each surface explored.

6.1 Future Work

In Chapter 3 of this dissertation, a hypothesis was formulated to describe the Wenzel to Cassie transition for droplet impingement on a superhydrophobic surface. Understanding the physical complexities of this transition is necessary to design robust superhydrophobic surfaces for industrial use. I give four reasons why further pursuing this project, and how, would be valuable. First, our mathematical arguments, which was based on an interfacial (potential) energy gradient, were postulated following observation of dewetting on a pillar-arrayed surface and considered "sound" when the equations agreed with experimental trends. These equations can be easily arranged to predict dewetting on other surface arrangements, such as uni-directional ribs, triangular/square pillars, pyramids, etc., and their agreement with new experiments would support the hypothesis. Second, further pursuit of this study facilitates a second well-sought-after physicochemical effect, namely, the isolation of friction at the triple contact line from viscous friction. This is a scenario difficult to establish given the induced shear stresses during contact line movement. Third, the use of different liquids besides water would also yield further insight. For example, glycerol offers a liquid which has significantly higher viscosity than water and exhibits more adhesion to Teflon, while maintaining similar interfacial energy values to that of water. The equations ascertain that as a result friction forces should increase while the driving force should remain constant, which should likewise be confirmed experimentally. Fourth, our hypothesis should be expanded to dewetting of sessile water droplets in the Wenzel state (such as one which originated due to condensation or one that was pushed into the Wenzel state) due to surface heating.

The boiling experiments presented in this dissertation also give room for subsequent follow-up studies. The idea that vapor escapes from underneath the droplet through the pillar forest can be confirmed by evaluating a superhydrophobic surface with "corral" type structures which are expected to completely obstruct vapor flow. Atomization on such surfaces would be expected to exceed that of atomization on pillar-type surfaces, and in so doing would strengthen the hypothesis of vapor escape. While nano-particles are typically much smaller than the size of nucleation sites necessary for vapor to grow, the literature has seen big differences in boiling droplets for hydrophilic interactions. Superhydrophobic surfaces with nano-scale texture has not been explored. Also, if the boiling dynamics observed are merely dependent on polarity considerations, then a non-polar liquid should exhibit similar boiling behavior on all four surfaces tested (superhydrophilic to superhydrophobic), but in reversed order. Finally, a strong analytical/numerical model to predict droplet impingement boiling would, needless to say, be a excellent complement to the experiments, validate the hypothesis of vapor escape and be useful in prediction. In order for a model of this type to be built though, in my opinion, the researcher must take a step back and first solve much simpler scenarios. Some of these simpler scenarios might include the nucleation and growth of a vapor bubble on the peak of a pillar and its descent into the surrounding gas cavities.

REFERENCES

[1] Commons, W., 2014. Lotus effect — wikimedia commons, the free media repository [Online; accessed 15-April-2016]. viii, 5

[2] Antonini, C., Amirfazli, A., and Marengo, M., 2012. "Drop impact and wettability: From hydrophilic to superhydrophobic surfaces." *Phys. Fluids,* **24**, p. 102104. viii, ix, 21, 27, 28, 34

[3] Attane, P., Girard, F., and Morin, V., 2007. "An energy balance approach of the dynamics of drop impact on a solid surface." *Phys. Fluids,* **19**, p. 12101. viii, 23, 24, 25, 31, 32, 33

[4] Aria, A., and Gharib, M., 2014. "Physicochemical characteristics and droplet impact dynamics of superhydrophobic carbon nanotube arrays." *Langmuir,* **30**, pp. 6780–6790. ix, 34

[5] Clanet, C., Beguin, C., Richard, D., and Quere, D., 2004. "Maximal deformation of an impacting drop." *J. Fluid Mech.,* **517**, pp. 199–208. ix, 34

[6] Tran, T., Staat, H., Prosperetti, A., Sun, C., and Lohse, D., 2012. "Drop impact on superheated surfaces." *Phys. Rev. Lett.,* **108**, p. 036101. ix, 34, 35

[7] Tran, T., Staat, H., Susarrey-Arce, A., Foertsch, T., van Houselt, A., Gardeniers, H., Prosperetti, A., Lohse, D., and Sun, C., 2013. "Droplet impact on superheated micro-structured surfaces." *Soft Matter,* **9**, p. 3272. ix, 34, 35

[8] Bertola, V., 2015. "An impact regime map for water drops impacting on heated surfaces." *International Journal of Heat and Mass Transfer,* **85**, pp. 430 – 437. xi, 16, 17, 66, 67, 68, 71, 77, 80, 82, 83, 84, 92, 95, 107

[9] Tran, T., Staat, H. J. J., Prosperetti, A., Sun, C., and Lohse, D., 2012. "Drop impact on superheated surfaces." *Phys. Rev. Lett.,* **108**, Jan, p. 036101. xi, 16, 17, 67, 68, 71, 74, 77, 80, 82, 83, 107

[10] Antonini, C., Bernagozzi, I., Jung, S., Poulikakos, D., and Marengo, M., 2013. "Water drops dancing on ice: How sublimation leads to drop rebound." *Physical Review Letters,* **111**, p. 014501. xi, 11, 67, 84, 85

[11] Tran, T., Staat, H. J. J., Susarrey-Arce, A., Foertsch, T. C., van Houselt, A., Gardeniers, H. J. G. E., Prosperetti, A., Lohse, D., and Sun, C., 2013. "Droplet impact on superheated micro-structured surfaces." *Soft Matter,* **9**, p. 3272. xi, 16, 17, 67, 68, 71, 72, 77, 80, 82, 83, 84, 85, 93

[12] Bird, E., 2014. Annual Report Tech. rep., Denver Botanic Gardens, Denver, CO. 3

[13] Koch, K., and Barthlott, W., 2009. "Superhydrophobic and superhydrophilic plant surfaces: an inspiration for biomimetic materials." *Philosophical Transactions of the Royal Society of London A: Mathematical, Physical and Engineering Sciences,* **367**(1893), pp. 1487–1509. 4

[14] Cassie, A., and Baxter, S., 1944. "Wettability of porous surfaces." *Trans Faraday Soc.,* **40**, pp. 546–551. 7

[15] Wenzel, R. N., 1936. "Resistance of solid surfaces to wetting by water." *Industrial & Engineering Chemistry,* **28**(8), pp. 988–994. 7

[16] Navier, C. L. M. H., 1823. "Memoire sur les lois du mouvement des fluides." *Mem. Acad. Sci. Inst. Fr.,* **6**, pp. 389–440. 7

[17] Woolford, B., Prince, J., Maynes, D., and Webb, B. W., 2009. "Particle image velocimetry characterization of turbulent channel flow with rib patterned superhydrophobic walls." *Physics of Fluids,* **21**, p. 085106. 7, 14

[18] Philip, J., 1972. "Flows satisfying mixed no-slip and no-shear conditions." *Z. Angew. Math. Phys.,* **23**, pp. 353–372. 7

[19] Philip, J., 1972. "Integral properties of flows satisfying mixed no-slip and no-shear conditions." *Z. Angew. Math. Phys.,* **23**, pp. 960–968. 7

[20] Crowdy, D., 2011. "Frictional slip lengths for unidirectional superhydrophobic grooved surfaces." *Physics of Fluids,* **23**, p. 072001. 8

[21] Lauga, E., and Stone, H., 2003. "Effective slip in pressure-driven stokes flow." *Journal of Fluid Mechanics,* **489**, pp. 55–77. 8

[22] Nukiyama, S., 1934. "Thermal conductivities of water and some water solutions." *J. Japan Soc. Mech. Eng.,* **37**, p. 367. 9

[23] Incropera, F., DeWitt, D., Bergmann, T., and Lavine, A., 2007. *Fundamentals of Heat and Mass Transfer.*, 6th ed. John Wiley and Sons. 9, 56

[24] Bernardin, J. D., Stebbins, C. J., and Mudawar, I., 1997. "Mapping of impact and heat transfer regimes of water drops impinging on a polished surface." *International Journal of Heat and Mass Transfer,* **40**(2), pp. 247 – 267. 9, 16, 66, 67, 92, 107

[25] Richard, D., and Quéré, D., 2000. "Bouncing water drops." *Europhysics Letters,* **50**, pp. 769–775. 10

[26] Richard, D., Clanet, C., and Quéré, D., 2002. "Contact time of a bouncing drop." *Nature,* **417**, p. 811. 11

[27] Clanet, C., Beguin, C., Richard, D., and Quéré, D., 2004. "Maximal deformation of an impacting drop." *Journal of Fluid Mechanics,* **517**, pp. 199–208. 11, 14

[28] Pearson, J. T., Maynes, D., and Webb, B. W., 2012. "Droplet impact dynamics for two liquids impinging on anisotropic superhydrophobic surfaces." *Experiments in Fluids,* **53**, pp. 603–618. 11

[29] Bechtel, S. E., Bogy, D. B., and Talke, F. E., 1981. “Impact of a liquid drop against a flat surface.” *IBM J. Res. Develop,* **25**, pp. 963–971. 13

[30] Wachters, L., and Westerling, N., 1966. “The heat transfer from a hot wall to impinging water drops in the spherical state.” *Chemical Engineering Science,* **21**, pp. 1047–1056. 13, 67, 92

[31] Attane, P., Girard, F., and Morin, V., 2007. “An energy balance approach of the dynamics of drop impact on a solid surface.” *Physics of Fluids,* **19**, p. 12101. 13

[32] Clavijo, C. E., Crockett, J., and Maynes, D., 2015. “Effects of isotropic and anisotropic slip on droplet impingement on a superhydrophobic surface.” *Physics of Fluids,* **27**(12). 14, 85, 99, 107

[33] Bico, J., Marzolin, C., and Quere, D., 1999. “Pearl drops.” *EPL (Europhysics Letters),* **47**(2), p. 220. 14

[34] Lafuma, A., and éré, D., 2003. “Superhydrophobic states.” *Nature materials,* **2**, pp. 457 – 460. 14

[35] Woolford, B., Maynes, D., and Webb, B. W., 2009. “Liquid flow through microchannels with grooved walls under wetting and superhydrophobic conditions.” *Microfluid Nanofluid,* **7**, pp. 121–135. 14

[36] Sun, T., Liu, H., Song, W., Wang, X., Jiang, L., Li, L., and Zhu, D., 2004. “Responsive aligned carbon nanotubes.” *Angewandte Chemie,* **116**, pp. 4763–4766. 15

[37] Krupenkin, T. N., Taylor, J. A., Wang, E. N., Kolodner, P., Hodes, M., and Salamon, T. R., 2007. “Reversible wetting-dewetting transitions on electrically tunable superhydrophobic nanostructured surfaces.” *Langmuir,* **23**(18), pp. 9128–9133 PMID: 17663572. 15

[38] Lee, C., and Kim, C.-J., 2011. “Underwater restoration and retention of gases on superhydrophobic surfaces for drag reduction.” *Phys. Rev. Lett.,* **106**, Jan, p. 014502. 15

[39] Cheng, Z., Lai, H., Zhang, N., Sun, K., and Jiang, L., 2012. “Magnetically induced reversible transition between cassie and wenzel states of superparamagnetic microdroplets on highly hydrophobic silicon surface.” *The Journal of Physical Chemistry C,* **116**(35), pp. 18796–18802. 15

[40] Boreyko, J. B., and Chen, C.-H., 2009. “Self-propelled dropwise condensate on superhydrophobic surfaces.” *Phys. Rev. Lett.,* **103**, Oct, p. 184501. 15, 20, 44

[41] He, B., Patankar, N. A., and Lee, J., 2003. “Multiple equilibrium droplet shapes and design criterion for rough hydrophobic surfaces.” *Langmuir,* **19**(12), pp. 4999–5003. 15

[42] Patankar, N. A., 2003. “On the modeling of hydrophobic contact angles on rough surfaces.” *Langmuir,* **19**(4), pp. 1249–1253. 15

[43] Cossali, G., Marengo, M., and Santini, M., 2005. “Secondary atomisation produced by single drop vertical impacts onto heated surfaces.” *Experimental Thermal and Fluid Science,* **29**(8), pp. 937 – 946. 16, 92, 93

[44] Leidenfrost, J. G., 1756. *De aquae communis nonnullis qualitatibus tractatus*. Ovenius. 16, 67, 93

[45] Clavijo, C., Crockett, J., and Maynes, D., 2016. "Hydrodynamics of drop impingement on hot surfaces of varying wettability." *Submitted*. 17, 92, 93, 95, 105, 108, 112

[46] Kwon, H.-m., Bird, J. C., and Varanasi, K. K., 2013. "Increasing leidenfrost point using micro-nano hierarchical surface structures." *Applied Physics Letters,* **103**(20), pp. –. 17, 66, 80, 87

[47] Weickgenannt, C. M., Zhang, Y., Sinha-Ray, S., Roisman, I. V., Gambaryan-Roisman, T., Tropea, C., and Yarin, A. L., 2011. "Inverse-leidenfrost phenomenon on nanofiber mats on hot surfaces." *Phys. Rev. E,* **84**, Sep, p. 036310. 17

[48] Nair, H., Staat, H. J. J., Tran, T., van Houselt, A., Prosperetti, A., Lohse, D., and Sun, C., 2014. "The leidenfrost temperature increase for impacting droplets on carbon-nanofiber surfaces." *Soft Matter,* **10**, pp. 2102–2109. 17, 67

[49] Jo, H., Ahn, H. S., Kang, S., and Kim, M. H., 2011. "A study of nucleate boiling heat transfer on hydrophilic, hydrophobic and heterogeneous wetting surfaces." *International Journal of Heat and Mass Transfer,* **54**(2526), pp. 5643 – 5652. 17, 74, 92, 94

[50] Jo, H., Park, H. S., and Kim, M. H., 2016. "Single bubble dynamics on hydrophobichydrophilic mixed surfaces." *International Journal of Heat and Mass Transfer,* **93**, pp. 554 – 565. 17, 74, 92

[51] Fan, L.-W., Li, J.-Q., Li, D.-Y., Zhang, L., and Yu, Z.-T., 2014. "Regulated transient pool boiling of water during quenching on nanostructured surfaces with modified wettability from superhydrophilic to superhydrophobic." *International Journal of Heat and Mass Transfer,* **76**, pp. 81 – 89. 17, 75, 92, 94

[52] Yong Park, J., Gardner, A., King, W. P., and Cahill, D. G., 2014. "Droplet impingement and vapor layer formation on hot hydrophobic surfaces." *Journal of Heat Transfer,* **136**. 18, 68, 92

[53] Li, X., Ma, X., and Lan, Z., 2009. "Behavioral patterns of drop impingement onto rigid substrates with a wide range of wettability and different surface temperatures." *AIChE Journal,* **55**(8), pp. 1983–1992. 18, 66, 67, 68, 92

[54] Hays, R., Maynes, D., and Crockett, J., 2016. "Thermal transport to droplets on heated superhydrophobic substrates." *International Journal of Heat and Mass Transfer,* **98**, pp. 70 – 80. 18, 68, 77, 92

[55] Herminghaus, S., 2000. "Roughness-induced non-wetting." *Europhys. Lett.,* **52**, p. 165. 20, 44

[56] Blossey, R., 2003. "Self-cleaning surfaces - virtual realities." *Nature Mater,* **2**, pp. 301–306. 20, 44

[57] S.Y. Teh, R. Lin, L. H., and Lee, A. "Droplet microfluidics." *Lab Chip,* **8**. 20

[58] Brouzes, E., Medkova, M., Savenelli, N., Marran, D., Twardowski, M., Hutchison, J., Rothberg, J., Link, D., Perrimon, N., and Samuels, M., 2009. “Droplet microfluidic technology for single-cell high-throughput screening.” *Proc Natl Acad Sci,* **106**, pp. 14195–14200. 20

[59] Pizzola, P., Roth, S., and Forest, P. D., 1986. “Blood droplet dynamics–i.” *J. Forensic Sci.,* **31**, pp. 36–49. 20

[60] Srinivasan, V., Pamula, V., and Fair, R., 2004. “Droplet-based microfluidic lab-on-a-chip for glucose detection.” *Analytica Chimica Acta,* **507**, pp. 145–150. 20

[61] Nizkaya, T., Asmolov, E., and Vinogradova, O., 2014. “Gas cushion model and hydrodynamic boundary conditions for superhydrophobic textures.” *Phys. Rev. E,* **90**, p. 043017. 20, 35

[62] Steinberger, A., Cottin-Bizonne, C., Kleimann, P., and Charlaix, E., 2007. “high friction on a bubble mattress.” *Nature Mater.,* **6**. 20, 39

[63] Navier, C. L. M. H., 1823. “Memoire sur les lois du mouvement des fluides.” *Mem. Acad. Sci. Inst. Fr.,* **6**, pp. 389–440. 20, 25

[64] Ybert, C., Barentin, C., Cottin-Bizonne, C., Joseph, P., and Bocquet, L., 2007. “Achieving large slip with superhydrophobic surfaces: Scaling laws for generic geometries.” *Phys. Fluids,* **19**, p. 123601. 20, 29

[65] Lauga, E., and Stone, H., 2003. “Effective slip in pressure-driven stokes flow.” *J. Fluid Mech.,* **489**, pp. 55–77. 20, 26

[66] Crowdy, D., 2011. “Frictional slip lengths for unidirectional superhydrophobic grooved surfaces.” *Phys. Fluids,* **23**, p. 072001. 20, 22, 26, 37, 38

[67] Philip, J., 1972. “Flows satisfying mixed no-slip and no-shear conditions.” *Z. Angew. Math. Phys.,* **23**, pp. 353–372. 20

[68] Philip, J., 1972. “Integral properties of flows satisfying mixed no-slip and no-shear conditions.” *Z. Angew. Math. Phys.,* **23**, pp. 960–968. 20

[69] Bazant, M., and Vinogradova, O., 2008. “Tensorial hydrodynamic slip.” *J. Fluid Mech.,* **613**, pp. 125–134. 20, 22

[70] Prince, J. F., Maynes, D., and Crockett, J., 2012. “Analysis of laminar jet impingement and hydraulic jump on a horizontal surface with slip.” *Phys. Fluids,* **24**, p. 102103. 20, 22

[71] Prince, J., Crockett, J., and Maynes, D., 2014. “Jet impingement and the hydraulic jump on horizontal surfaces with anisotropic slip.” *Phys. Fluids,* **26**, p. 042104. 20, 22, 44

[72] Ou, J., and Rothstein, J. P., 2005. “Direct velocity measurements of the flow past drag-reducing ultrahydrophobic surfaces.” *Phys. Fluids,* **17**, p. 103606. 20

[73] Ou, J., Perot, B., and Rothstein, J. P., 2004. “Laminar drag reduction in microchannels using ultrahydrophobic surfaces.” *Phys. Fluids,* **16**, pp. 4635–4643. 20

[74] Lee, C., Choi, C.-H., and Kim, C.-J., 2008. “Structured surfaces for giant liquid slip.” *Phys. Rev.,* **101**, p. 064501. 20

[75] Richard, D., Clanet, C., and Quere, D., 2002. “Contact time of a bouncing drop.” *Nature,* **417**, p. 811. 21

[76] Antonini, C., Bernagozzi, I., Jung, S., Poulikakos, D., and Marengo, M., 2013. “Water drops dancing on ice: How sublimation leads to drop rebound.” *Phys. Rev. Lett.,* **111**, p. 014501. 21, 30

[77] Pearson, J. T., Maynes, D., and Webb, B. W., 2012. “Droplet impact dynamics for two liquids impinging on anisotropic superhydrophobic surfaces.” *Exp. Fluids,* **53**, pp. 603–618. 21, 36, 41, 44, 46

[78] Madejski, J., 1975. “Solidification of droplets on a cold surface.” *Inter. J. Heat Mass Transfer,* **19**, pp. 1009–1013. 22, 23

[79] Bechtel, S. E., Bogy, D. B., and Talke, F. E., 1981. “Impact of a liquid drop against a flat surface.” *IBM J. Res. Develop,* **25**, pp. 963–971. 22

[80] Maynes, D., Johnson, M., and Webb, B. W., 2011. “Free-surface liquid jet impingement on rib patterned superhydrophobic surfaces.” *Phys. Fluids,* **23**, p. 052104. 22, 44

[81] Dressaire, E., Courbin, L., Crest, J., and Stone, H., 2009. “Thin-film fluid flows over microdecorated surfaces: Observation of polygonal hydraulic jumps.” *Phys. Rev. Lett.,* **102**, p. 194503. 22, 29

[82] Dressaire, E., Courbin, L., Crest, J., and Stone, H., 2010. “Inertia dominated thin-film flows over microdecorated surfaces.” *Phys. Fluids,* **22**, pp. –. 22, 29

[83] Daniello, R. J., Waterhouse, N. E., and Rothstein, J. P., 2009. “Drag reduction in turbulent flows over superhydrophobic surfaces.” *Phys. Fluids,* **21**, p. 085103. 22

[84] Davies, J., Maynes, D., Webb, B. W., and Woolford, B., 2006. “Laminar flow in a microchannel with superhydrophobic walls exhibiting transverse ribs.” *Phys. Fluids,* **18**, p. 087110. 22, 44

[85] Yarin, A. L., 2006. “Drop impact dynamics: splashing, spreading, receding, bouncing....” *Annu. Rev. Fluid Mech.,* **38**, pp. 159–92. 23, 36

[86] Lee, C., Nam, Y., Lastakowski, H., Hur, J., Shin, S., Biance, A., Pirat, C., Kim, C., and Ybert, C., 2015. “Two types of cassie-to-wenzel wetting transitions on superhydrophobic surfaces during drop impact.” *Soft Matter,* **11**, p. 4592. 29, 49

[87] Wachters, L., and Westerling, N., 1966. “The heat transfer from a hot wall to impinging water drops in the spherical state.” *Chemical Engineering Science,* **21**, pp. 1047–1056. 30

[88] Kolinski, J., Mahadevan, L., and Rubinstein, S., 2014. “Drops can bounce from perfectly hydrophilic surfaces.” *Europhys. Lett.,* **108**, p. 24001. 30

[89] Mundo, C., Sommerfeld, M., and Tropea, C., 1995. “Droplet-wall collisions: Experimental studies of the deformation and breakup process.” *Int. J. Multiphase Flow,* **21**, pp. 151 – 173. 36

[90] Kamnis, S., and Gu, S., 2005. “Numerical modelling of droplet impingement.” *J. Physics D: Appl. Phys.,* **38**, p. 3664. 36

[91] Woolford, B., Maynes, D., and Webb, B. W., 2009. “Liquid flow through microchannels with grooved walls under wetting and superhydrophobic conditions.” *Microfluid Nanofluid,* **7**, pp. 121–135. 39, 44

[92] Pearson, J., Maynes, D., Bilodeau, D., and Webb, B., 2013. “Two-pronged jet formation caused by droplet impact on anisotropic superhydrophobic surfaces.” Proceedings of the ASME 2013 Fluids Engineering Summer Meeting, Incline Village, CA. 41

[93] Wenzel, R. N., 1936. “Resistance of solid surfaces to wetting by water.” *Industrial & Engineering Chemistry,* **28**(8), pp. 988–994. 44

[94] Cassie, A., and Baxter, S., 1944. “Wettability of porous surfaces.” *Trans Faraday Soc.,* **40**, pp. 546–551. 44

[95] Arya, S., Khan, S., Vaid, A., Kour, H., and Lehana, P., 2013. “Microfluidic mechanics and applications: a review.” *Journal of Nano- and Electronic Physics,* **5**(4), p. 04047. 44

[96] Quere, D., 2008. “Wetting and roughness.” *Annu. Rev. Mater. Res.,* **38**, pp. 71–99. 44

[97] Guo, Z., and Liu, W., 2007. “Biomimic from the superhydrophobic plant leaves in nature: Binary structure and unitary structure.” *Plant Science,* **172**(6), pp. 1103 – 1112. 44

[98] Bird, J. C., Dhiman, R., Kwon, H., and Varanasi, K. K., 2013. “Reducing the contact time of a bouncing drop.” *Nature,* **503**, pp. 385–388. 44

[99] Tiwari, M. K., Bayer, I. S., Jursich, G. M., Schutzius, T. M., and Megaridis, C. M., 2010. “Highly liquid-repellent, large-area, nanostructured poly(vinylidene fluoride)/poly(ethyl 2-cyanoacrylate) composite coatings: Particle filler effects.” *ACS Applied Materials & Interfaces,* **2**(4), pp. 1114–1119. 44

[100] Feng, L., Li, S., Li, Y., Li, H., Zhang, L., Zhai, J., Song, Y., Liu, B., Jiang, L., and Zhu, D., 2002. “Super-hydrophobic surfaces: from natural to artificial.” *Advanced materials,* **14**(24), pp. 1857–1860. 44

[101] Maynes, D., Jeffs, K., Woolford, B., and Webb, B. W., 2007. “Laminar flow in a microchannel with hydrophobic surface patterned microribs oriented parallel to the flow direction.” *Phys. Fluids,* **19**, p. 093603. 44

[102] Woolford, B., Prince, J., Maynes, D., and Webb, B. W., 2009. “Particle image velocimetry characterization of turbulent channel flow with rib patterned superhydrophobic walls.” *Phys. Fluids,* **21**, p. 085106. 44

[103] Maynes, D., Webb, B. W., Crockett, J., and Solovjov, V., 2013. "Analysis of laminar slip-flow thermal transport in microchannels with transverse rib and cavity structured superhydrophobic walls." *J. Heat Transfer,* **135**, p. 021701. 44

[104] Maynes, D., and Crockett, J., 2014. "Apparent temperature jump and thermal transport in channels with streamwise rib and cavity featured superhydrophobic walls at constant heat flux." *J. Heat Transfer,* **136**, p. 011701. 44

[105] Maynes, D., Webb, B., and Davies, J., 2008. "Thermal transport in a microchannel exhibiting ultrahydrophobic microribs maintained at constant temperature." *J. Heat Transfer,* **130**, p. 022402. 44

[106] Cowley, A., Maynes, D., and Crockett, J., 2014. "Effective temperature jump and influence of axial conduction for thermal transport through channels with superhydrophobic walls." *Int. J. Heat Mass Transfer,* **79**, pp. 573–583. 44

[107] Patankar, N. A., 2004. "Transition between superhydrophobic states on rough surfaces." *Langmuir,* **20**, pp. 7097–7102. 44, 57

[108] Reyssat, M., Yeomans, J. M., and Quéré, D., 2008. "Impalement of fakir drops." *EPL (Europhysics Letters),* **81**(2), p. 26006. 44

[109] Lafuma, A., and Quere, D., 2003. "Superhydrophobic states." *Nature mater.,* **2**, pp. 457 – 460. 44, 46

[110] Krupenkin, T. N., Taylor, J. A., Wang, E. N., Kolodner, P., Hodes, M., and Salamon, T. R., 2007. "Reversible wetting and dewetting transitions on electrically tunable superhydrophobic nanostructured surfaces." *Langmuir,* **23**(18), pp. 9128–9133 PMID: 17663572. 44, 46

[111] Bartolo, D., Bouamrirene, F., Verneuil, ., Buguin, A., Silberzan, P., and Moulinet, S., 2006. "Bouncing or sticky droplets: Impalement transitions on superhydrophobic micropatterned surfaces." *EPL (Europhysics Letters),* **74**(2), p. 299. 44

[112] Manukyan, G., Oh, J. M., van den Ende, D., Lammertink, R. G. H., and Mugele, F., 2011. "Electrical switching of wetting states on superhydrophobic surfaces: A route towards reversible cassie-to-wenzel transitions." *Phys. Rev. Lett.,* **106**, Jan, p. 014501. 44

[113] Dupuis, A., and Yeomans, J. M., 2005. "Modeling droplets on superhydrophobic surfaces: equilibrium states and transitions." *Langmuir,* **21**(6), pp. 2624–2629 PMID: 15752062. 44

[114] Koishi, T., Yasuoka, K., Fujikawa, S., Ebisuzaki, T., and Zeng, X. C., 2009. "Coexistence and transition between cassie and wenzel state on pillared hydrophobic surface." *Proceedings of the National Academy of Sciences,* **106**(21), pp. 8435–8440. 44

[115] Zheng, Q.-S., Yu, Y., and Zhao, Z.-H., 2005. "Effects of hydraulic pressure on the stability and transition of wetting modes of superhydrophobic surfaces." *Langmuir,* **21**(26), pp. 12207–12212 PMID: 16342993. 44

[116] He, B., Patankar, N. A., and Lee, J., 2003. "Multiple equilibrium droplet shapes and design criterion for rough hydrophobic surfaces." *Langmuir,* **19**(12), pp. 4999–5003. 44, 57, 58

[117] Patankar, N. A., 2003. “On the modeling of hydrophobic contact angles on rough surfaces.” *Langmuir,* **19**(4), pp. 1249–1253. 44, 57, 58

[118] Bico, J., Thiele, U., and Quéré, D., 2002. “Wetting of textured surfaces.” *Colloids and Surfaces A: Physicochemical and Engineering Aspects,* **206**(13), pp. 41 – 46. 44

[119] Reyssat, M., Pepin, A., Marty, F., Chen, Y., and Quéré, D., 2006. “Bouncing transitions on microtextured materials.” *EPL (Europhysics Letters),* **74**(2), p. 306. 45, 46, 51

[120] Jung, Y. C., and Bhushan, B., 2009. “Dynamic effects induced transition of droplets on biomimetic superhydrophobic surfaces.” *Langmuir,* **25**(16), pp. 9208–9218 PMID: 19441842. 45

[121] Deng, T., Varanasi, K. K., Hsu, M., Bhate, N., Keimel, C., Stein, J., and Blohm, M., 2009. “Nonwetting of impinging droplets on textured surfaces.” *Applied Physics Letters,* **94**(13), pp. –. 45

[122] Clavijo, C. E., Crockett, J., and Maynes, D., 2015. “Effects of isotropic and anisotropic slip on droplet impingement on a superhydrophobic surface.” *Physics of Fluids,* **27**(12). 46

[123] Rosengarten, G., Tetuko, A., Li, K., Wu, A., and Lamb, R., 2011. “The effect of nanostrucutred surfaces on droplet impingement heat transfer.” Proceedings of the ASME 2011 International Mechanical Engineering Congress and Exposition, Washington, D.C. 46

[124] Krupenkin, T. N., Taylor, J. A., Schneider, T. M., and Yang, S., 2004. “From rolling ball to complete wetting: the dynamic tuning of liquids on nanostructured surfaces.” *Langmuir,* **20**(10), pp. 3824–3827 PMID: 15969363. 46

[125] Krupenkin, T., Taylor, J., Kolodner, P., and Hodes, M., 2005. “Electrically tunable superhydrophobic nanostructured surfaces.” *Bell Labs Technical Journal,* **10**(3), Fall, pp. 161–170. 46

[126] Liu, G., Fu, L., Rode, A. V., and Craig, V. S. J., 2011. “Water droplet motion control on superhydrophobic surfaces: Exploiting the wenzel-to-cassie transition.” *Langmuir,* **27**(6), pp. 2595–2600 PMID: 21322574. 46

[127] Cheng, Z., Lai, H., Zhang, N., Sun, K., and Jiang, L., 2012. “Magnetically induced reversible transition between cassie and wenzel states of superparamagnetic microdroplets on highly hydrophobic silicon surface.” *The Journal of Physical Chemistry C,* **116**(35), pp. 18796–18802. 46

[128] Lee, C., and Kim, C.-J., 2011. “Underwater restoration and retention of gases on superhydrophobic surfaces for drag reduction.” *Phys. Rev. Lett.,* **106**, Jan, p. 014502. 46

[129] Boreyko, J. B., and Chen, C.-H., 2009. “Restoring superhydrophobicity of lotus leaves with vibration-induced dewetting.” *Phys. Rev. Lett.,* **103**, Oct, p. 174502. 46

[130] Stamatopoulos, C., Schutzius, T. M., Koppl, C. J., Hayek, N. E., Maitra, T., Hemrle, J., and Poulikakos, D., 2016. “On the shedding of impaled droplets: The role of transient intervening layers.” *Scientific Reports,* **6**, p. 18875. 46

[131] Snoeijer, J. H., and Andreotti, B., 2013. "Moving contact lines: Scales, regimes, and dynamical transitions." *Annual Review of Fluid Mechanics,* **45**(1), pp. 269–292. 47

[132] Liu, Y., Moevius, L., Xu, X., Qian, T., Yeomans, J., and Wang, Z., 2014. "Pancake bouncing on superhydrophobic surfaces." *Nat Phys,* **10**(7), pp. 515–519. 47

[133] Jung, Y. C., and Bhushan, B., 2008. "Dynamic effects of bouncing water droplets on superhydrophobic surfaces." *Langmuir,* **24**(12), pp. 6262–6269 PMID: 18479153. 57

[134] Srivastava, N., Ding, C., Judson, A., MacDonald, N., and Meinhart, C., 2010. "A unified scaling model for flow through a lattice of microfabricated posts." *Lab on a Chip,* **10**, pp. 1148–1152. 58

[135] Ishino, C., Reyssat, M., Reyssat, E., Okumura, K., and Quere, D., 2007. "Wicking within forests of micropillars." *EPL (Europhysics Letters),* **79**(5), p. 56005. 58, 109

[136] de Gennes, P. G., 1985. "Wetting: statics and dynamics." *Rev. Mod. Phys.,* **57**, Jul, pp. 827–863. 59

[137] Fox, R. W., McDonald, A. T., and Pritchard, P. J., 2004. *Introduction to Fluid Mechanics.*, 6th ed. John Wiley & Sons, New Jersey. 60, 61

[138] Glasstone, S., Laidler, K., and Eyring, H., 1941. *The theory of rate processes*. McGraw-Hill, New York. 61

[139] Blake, T., 1993. *Wettability*. Marcel Dekker, New York, ch. 5. 61, 63

[140] Blake, T., and Coninck, J. D., 2002. "The influence of solid-liquid interactions on dynamic wetting." *Advances in colloid and interface science,* **96**, pp. 21–36. 61

[141] de Ruijterand J. De Coninckand G. Oshanin, M. J., 1999. "Droplet spreading: partial wetting regime revisited." *Langmuir,* **15**(6), pp. 2209–2216. 61

[142] Blake, T. D., 2006. "The physics of moving wetting lines." *Journal of Colloid and Interface Science,* **299**(1), pp. 1 – 13. 61

[143] Duvivier, D., Seveno, D., Rioboo, R., Blake, T. D., and Coninck, J. D., 2011. "Experimental evidence of the role of viscosity in the molecular kinetic theory of dynamic wetting." *Langmuir,* **27**(21), pp. 13015–13021 PMID: 21919445. 61

[144] Li, J., Hou, Y., Liu, Y., Hao, C., Li, M., Chaudhury, M. K., Yao, S., and Wang, Z. "Directional transport of high-temperature janus droplets mediated by structural topography." *Nature Physics,* **advance online publication**. 66

[145] del Cerro, D. A., lvaro G. Marn, Rmer, G. R. B. E., Pathiraj, B., Lohse, D., and in t Veld, A. J. H., 2012. "Leidenfrost point reduction on micropatterned metallic surfaces." *Langmuir,* **28**(42), pp. 15106–15110 PMID: 23020737. 66

[146] Fujimoto, H., Watanabe, S., Okamoto, T., Hama, T., and Takuda, H., 2015. "Photographic study of hydrodynamics of drops of aqueous polymer solution impinging on hot solid." *Experimental Thermal and Fluid Science,* **60**, pp. 66 – 74. 66

[147] Gradeck, M., Seiler, N., Ruyer, P., and Maillet, D., 2013. "Heat transfer for leidenfrost drops bouncing onto a hot surface." *Experimental Thermal and Fluid Science,* **47**, pp. 14 – 25. 66

[148] Lee, C., Kim, D., Kim, H., and Kim, K., 2015. "Dynamic behavior and micro-explosion characteristics of impinging droplets on a high-temperature surface." *Journal of Visualization,* **18**(1), pp. 59–70. 66, 93, 94

[149] Kim, H., Truong, B., Buongiorno, J., and Hu, L.-W., 2011. "On the effect of surface roughness height, wettability, and nanoporosity on leidenfrost phenomena." *Applied Physics Letters,* **98**(8), pp. –. 66

[150] Fujimoto, H., Oku, Y., Ogihara, T., and Takuda, H., 2010. "Hydrodynamics and boiling phenomena of water droplets impinging on hot solid." *International Journal of Multiphase Flow,* **36**(8), pp. 620 – 642. 66

[151] Engel, O., 1955. "Waterdrop collisions with solid surfaces." *Journal of Research of the National Bureau of Standards,* **54**, pp. 281– 298. 67, 92

[152] Chandra, S., and Avedisian, C., 1992. "Observations of droplet impingement on a ceramic porous surface." *International Journal of Heat and Mass Transfer,* **35**(10), pp. 2377 – 2388. 67, 92

[153] Negeed, E.-S. R., Hidaka, S., Kohno, M., and Takata, Y., 2013. "High speed camera investigation of the impingement of single water droplets on oxidized high temperature surfaces." *International Journal of Thermal Sciences,* **63**, pp. 1 – 14. 67

[154] Moita, A., and Moreira, A., 2012. "Scaling the effects of surface topography in the secondary atomization resulting from droplet/wall interactions." *Experiments in Fluids,* **52**(3), pp. 679–695. 67

[155] Mahulkar, A. V., Marin, G. B., and Heynderickx, G. J., 2015. "Dropletwall interaction upon impingement of heavy hydrocarbon droplets on a heated wall." *Chemical Engineering Science,* **130**, pp. 275 – 289. 67

[156] Nam, Y., Wu, J., Warrier, G., and Ju, Y. S., 2009. "Experimental and numerical study of single bubble dynamics on a hydrophobic surface." *Journal of Heat Transfer,* **131**, p. 121004. 74

[157] Vakarelski, I. U., Patankar, N. A., Marston, J. O., Chan, D. Y. C., and Thoroddsen, S. T., 2012. "Stabilization of leidenfrost vapour layer by textured superhydrophobic surfaces." *Nature Letter,* **489**, p. 274. 75, 92, 94

[158] Clavijo, C., Crockett, J., and Maynes, D., 2016. "Wenzel to cassie transition during droplet impingement on a superhydrophobic surface." *Submitted.* 78

[159] Biance, A.-L., Chevy, F., Clanet, C., Lagubeau, G., and Quéré, D., 2006. "On the elasticity of an inertial liquid shock." *Journal of Fluid Mechanics,* **554**, 5, pp. 47–66. 84

[160] Reyssat, M., Richard, D., Clanet, C., and Quere, D., 2010. "Dynamical superhydrophobicity." *Faraday Discuss.,* **146**, pp. 19–33. 84

[161] Rosengarten, G., Tetuko, A., Li, K., Wu, A., and Lamb, R., 2011. "The effect of nano-strucutred surfaces on droplet impingement heat transfer." Proceedings of the ASME 2011 International Mechanical Engineering Congress and Exposition, Washington, D.C. 85

[162] Steinberger, A., Cottin-Bizonne, C., Kleimann, P., and Charlaix, E., 2007. "high friction on a bubble mattress." *Nature Mater.,* **6**. 87

[163] Totten, G., Bates, C., and Clinton, N., 1993. *Handbook of Quenchants and Quenching Technology*. ASM International. 92

[164] You, S., Simon, T., and Bar-Cohen, A., 1992. "A technique for enhancing boiling heat transfer with application to cooling of electronic equipment." *Components, Hybrids, and Manufacturing Technology, IEEE Transactions on,* **15**(5), Oct, pp. 823–831. 92

[165] Ahn, H. S., Lee, C., Kim, H., Jo, H., Kang, S., Kim, J., Shin, J., and Kim, M. H., 2010. "Pool boiling {CHF} enhancement by micro/nanoscale modification of zircaloy-4 surface." *Nuclear Engineering and Design,* **240**(10), pp. 3350 – 3360 4th International Topical Meeting on High Temperature Reactor Technology (HTR 2008), with Regular Papers. 92

[166] Moita, A., and Moreira, A., 2007. "Drop impacts onto cold and heated rigid surfaces: Morphological comparisons, disintegration limits and secondary atomization." *International Journal of Heat and Fluid Flow,* **28**(4), pp. 735 – 752 Including Special Issue of Conference on Modelling Fluid Flow (CMFF06), Budapest13th event of the international conference series in fluid flow technologies: conference on modelling fluid flow. 92, 93, 94, 96, 99

[167] Bertola, V., and Sefiane, K., 2005. "Controlling secondary atomization during drop impact on hot surfaces by polymer additives." *Physics of Fluids,* **17**(10). 92

[168] Choi, C., Shin, J. S., Yu, D. I., and Kim, M. H., 2011. "Flow boiling behaviors in hydrophilic and hydrophobic microchannels." *Experimental Thermal and Fluid Science,* **35**(5), pp. 816 – 824 7th ECI-International Conference on Boiling Heat Transfer ICBHT-2009. 92

[169] Thome, J. R., 2004. "Boiling in microchannels: a review of experiment and theory." *International Journal of Heat and Fluid Flow,* **25**(2), pp. 128 – 139 Selected Papers from the 5th {ECI} International Conference on Boiling Heat Transfer. 92

[170] Takata, Y., Hidaka, S., and Uraguchi, T., 2006. "Boiling feature on a super water-repellent surface." *Heat Transfer Engineering,* **27**(8), pp. 25–30. 92, 94

[171] Chaves, H., Kubitzek, A. M., and Obermeier, F., 1999. "Dynamic processes occurring during the spreading of thin liquid films produced by drop impact on hot walls." *International Journal of Heat and Fluid Flow,* **20**(5), pp. 470 – 476. 93, 97

[172] Cossali, G., Marengo, M., and Santini, M., 2008. "Thermally induced secondary drop atomisation by single drop impact onto heated surfaces." *International Journal of Heat and Fluid Flow,* **29**(1), pp. 167 – 177. 93, 98

[173] Cossali, G. E., Marengo, M., Santini, M., and Watanabe, J., 2002. "Secondary droplet atomisation from single drop impact on heated surfaces." *Zaragoza,* **9**, p. 11. 94

[174] Damaschke, N., Gouesbet, G., Gréhan, G., Mignon, H., and Tropea, C., 1998. “Response of phase doppler anemometer systems to nonspherical droplets.” *Appl. Opt.,* **37**(10), Apr, pp. 1752–1761. 94

[175] Castanet, G., Dunand, P., Caballina, O., and Lemoine, F., 2013. “High-speed shadow imagery to characterize the size and velocity of the secondary droplets produced by drop impacts onto a heated surface.” *Experiments in Fluids,* **54**(3), pp. 1–17. 94, 99

[176] Ranz, W., and Marshall, W., 1952. “Evaporation from drops.” *Chem. Eng. Prog.,* **48**(141). 98

[177] Taylor, J. R., 2003. *Classical Mechanics*. University Science Books, Sausalito, CA. 98